



Cape Peninsula
University of Technology

**POWER SYSTEM STABILITY ENHANCEMENT IN THE PRESENCE OF RENEWABLE
ENERGY RESOURCES**

By

BRICE EKOME NNA

Thesis submitted in fulfilment of the requirements for the degree

Master of Engineering: Energy

in the Faculty of Engineering and built environment

at the Cape Peninsula University of Technology

Supervisor: Prof Khaled Aboalez

Bellville

March 2023

CPUT copyright information

The dissertation/thesis may not be published either in part (in scholarly, scientific or technical journals), or as a whole (as a monograph), unless permission has been obtained from the University.

DECLARATION

I, Brice Ekome Nna, declare that the contents of this thesis represent my own unaided work, and that the dissertation/thesis has not previously been submitted for academic examination towards any qualification. Furthermore, it represents my own opinions and not necessarily those of the Cape Peninsula University of Technology.

Signed

A handwritten signature in black ink, consisting of several overlapping loops and lines, positioned between the 'Signed' and 'Date' labels.

Date: 07-03-2023

ABSTRACT

In power systems, electrical networks constantly face unexpected events such as faults on lines or busses, sudden changes in load demand and loss of generation. When these events occur, the power grid can be plagued by uncontrollable loop currents, overloading equipment, and system instabilities, leading to cascade outages. In other words, all these events can cause the system to lose its stability. The concept of stability is essential in the power system, either with or without renewable energy. It is the system's ability to preserve its synchronism after disturbances have occurred. Maintaining synchronism is necessary in the power system due to the day-by-day expenditure of the system.

This research focuses on enhancing the stability of a wind-integrated power system that is subjected to faults. The system stability is enhanced by using PSHP on a 100 MW wind power integrated network, the modified New England test system known as the 10-machines 39-bus system. Modern pumped storage hydropower plants (PSHP) based on doubly fed induction machines (DFIM), also known as variable speed PSHP, and conventional PSHP based on synchronous machines (SM), also known as fixed speed PSHP, both have distinct effects on the stability of a large-scale power system (FS). Comparing the effects of DFIM and SM-based PSHP in terms of the best stability improvement solution has shown that DFIM-PSHP presents better stability improvement results than SM-DFIM.

Simulations were carried out using Digsilent Power Factory software, considering two study cases. The 1st study case is the stability improvement with a SM-based PSHP instead of a synchronous machine on Bus 10. The 2nd study is the stability improvement with a DFIM-based PSHP instead of SM-based PSHP. The two study cases were done under various scenarios, and it was shown that stability is best improved with the use of DFIM-based PSHP compared to SM-based PSHP.

ACKNOWLEDGEMENTS

I wish to thank:

- The Almighty God for granting me this opportunity of such a success in my life.
- My supervisors Prof. KM Aboalez and Dr M Giraneza, for guidance and accommodating me whenever there was a need. Your constant encouragement, support, and invaluable suggestions and contributions made this work successful.
- My parents, brothers, and sisters for prayers and believing in me.
- Prof A.K Raji and Prof. MTE Kahn from The Cape Peninsula University of Technology Centre for Power Systems Research (CPSR) for the knowledge gained from the master of engineering in energy courses taken during my first year of master especially the modules such as generation, transmission and distribution and Energy modelling conducted by them.
- My best friends and all my friends for their help, support, and prayers.

TABLE OF CONTENTS

Declaration	ii
Abstract	iii
Acknowledgements	iv
Table of contents	v
List of figures	ix
List of tables.....	xi
Abbreviations and symbols	xii
CHAPTER ONE: INTRODUCTION	1
1.1. Background.....	1
1.2. Problem statement	2
1.3. Research question.....	2
1.4. Significance of problem	2
1.5. Research objectives	3
1.6. Methodology	3
1.7. Thesis outline	4
CHAPTER TWO: LITERATURE REVIEW.....	6
2.1. Introduction.....	6
2.2. Basic concept	6
2.2.1. Power system	6
2.2.1.1. Substation for Power Generation	7
2.2.1.2. Substation for Transmission	7
2.2.1.3. Substation for distribution.....	8
2.2.2. Power system stability	8
2.2.2.1. Rotor angle stability	9
2.2.2.2. Voltage stability	9
2.2.2.3. Frequency stability.....	9
2.2.3. Power system stability study tools	10
2.2.3.1. Power flow	10
2.2.3.1.1. PV bus	10
2.2.3.1.2. PQ bus.....	10
2.2.3.1.3. Slack bus	10
2.2.3.1.4. Device busses	10
2.2.3.2. Fault.....	11
2.2.3.2.1. Open circuit faults	11
2.2.3.2.2. Short circuit faults.....	11
2.2.3.3. Reasons for choosing digsilent Powerfactory	13
2.2.4. Wind energy	13

2.2.5.	Pumped storage hydropower	16
2.3.	Power system stability enhancement	17
2.3.1.	Power System Stabilizer	17
2.3.2.	FACTS devices	20
2.3.2.1.	SVC	21
2.3.2.2.	STATCOM	21
2.3.3.	Battery Energy Storage System (BESS)	24
2.3.4.	Pumped Storage Hydropower Plants (PSHP)	25
2.4.	Stability improvement summary table	26
2.5.	Conclusion	26
	CHAPTER THREE: IEEE 39 BUS SYSTEM MATHEMATICAL MODELLING	28
3.1.	Introduction	28
3.2.	Power system elements of 39 bus systems	28
3.2.1.	Synchronous generator	28
3.2.2.	Transformers	31
3.2.3.	Transmission Lines	33
3.2.4.	Load	36
3.2.5.	Busbars	37
3.3.	DFIG based Wind Power	37
3.4.	PSHP modelling	38
3.4.1.	DFIM	39
3.4.2.	Synchronous Machine	40
3.5.	Mathematical formulation of Newton Raphson method	41
3.6.	Mathematical formulation of Three Phase Line to Line Fault	42
3.7.	Mathematical formulation of power system stability	45
3.7.1.	Mathematical formulation of rotor angle stability	46
3.7.1.1.	Swing equation	46
3.7.1.2.	Critical clearing time	47
3.7.2.	Mathematical formulation voltage stability	49
3.8.	Conclusion	52
	CHAPTER FOUR: IEEE 39 BUS SYSTEM COMPUTER MODELLING	53
4.1.	Introduction	53
4.2.	IEEE 39 bus system	53
4.2.1.	Generators	53
4.2.2.	Power transformers	54
4.2.3.	Transmission lines	56
4.2.4.	Loads	57
4.3.	DFIG Wind Turbines	59
4.3.1.	DFIG Controllers	59

4.3.1.1.	Composite frame of the DFIG	59
4.3.1.2.	Gen PQ-Controller	60
4.3.1.3.	Irot ctrl	61
4.3.1.4.	Pitch Control	61
4.3.1.5.	MPT Control	61
4.3.1.6.	Protection.....	62
4.3.1.7.	Rotor current measurement.....	63
4.3.1.8.	Shaft	64
4.3.2.	DFIG computation.....	65
4.4.	Pumped Storage Hydropower.....	66
4.4.1.	Variable-Speed PSHP Model	66
4.4.1.1.	Composite frame of the DFIG	66
4.4.1.2.	Active power reduction controller.....	67
4.4.1.3.	Irot ctrl.....	67
4.4.1.4.	Governor	67
4.4.1.5.	Hydraulic.....	68
4.4.1.6.	Protection	68
4.4.1.7.	PQ Control	69
4.4.2.	Fixed-Speed PSHP Model.....	71
4.4.2.1.	Composite frame of the DFIG	71
4.4.2.2.	Active power reduction controller.....	72
4.4.2.3.	Governor	72
4.4.2.4.	Hydraulic.....	72
4.4.2.5.	AVR	73
4.5.	Transient Analysis.....	74
4.6.	Conclusion.....	74
	CHAPTER FIVE: RESULTS AND DISCUSSION	75
5.1.	Introduction	75
5.2.	Benchmark case study: 39 Bus system.....	75
5.2.1.	Scenario 1: Normal operating conditions	75
5.2.1.1.	Voltage stability	76
5.2.1.2.	Rotor angle stability	80
5.2.2.	Scenario 2: 100MW of Wind integration.....	81
5.2.2.1.	Voltage stability	82
5.2.2.2.	Rotor angle stability	83
5.2.3.	Scenario 3: 150-millisecond fault at bus 30	84
5.2.3.1.	Voltage stability	84
5.2.3.2.	Rotor angle stability	85
5.2.4.	Scenario 4: 450-millisecond fault at bus 30.....	86

5.2.4.1.	Voltage stability	86
5.2.4.2.	Rotor angle stability	87
5.3.	Proposed solutions	88
5.3.1.	Case study 1: Synchronous Machine Pumped Storage hydropower (SM-PSHP). 88	
5.3.1.1.	Scenario 1: 150-millisecond fault at bus 30	89
5.3.1.1.1.	Voltage stability	89
5.3.1.1.2.	Rotor angle stability	90
5.3.1.2.	Scenario 2: 450-millisecond fault at bus 30	91
5.3.1.2.1.	Voltage stability	91
5.3.1.2.2.	Rotor angle stability	92
5.3.2.	Case study 2: Doubly Fed Induction Machine Pumped Storage hydropower (DFIM-PSHP)	93
5.3.2.1.	Scenario 1: 150-millisecond fault at bus 30	94
5.3.2.1.1.	Voltage stability	94
5.3.2.1.2.	Rotor angle stability	95
5.3.2.2.	Scenario 2: 450-millisecond fault at bus 30	96
5.3.2.2.1.	Voltage stability	96
5.3.2.2.2.	Rotor angle stability	97
5.4.	Discussion	98
5.4.1.	150-millisecond fault at bus 30	98
5.4.1.1.	Voltage stability	98
5.4.1.2.	Rotor angle stability	99
5.4.2.	450-millisecond fault at bus 30	100
5.4.2.1.	Voltage stability	100
5.4.2.2.	Rotor angle stability	101
5.5.	Conclusion	103
	CHAPTER SIX: CONCLUSION AND FUTURE WORK.....	104
7.	REFERENCES	106

LIST OF FIGURES

Figure 2.1: Schematic diagram of a primary configuration of an electrical power system.	7
Figure 2.2: Classification of power system stability	8
Figure 2.3: LG fault	11
Figure 2.4: LL fault	12
Figure 2.5: LLG fault	12
Figure 2.6: LLLG fault	12
Figure 2.7: LLL fault	13
Figure 2.8: Conversion of wind power to electrical power	14
Figure 2.9: grid connected squirrel cage induction generator	14
Figure 2.10: Example of inertia response emulation of a wind turbine generator.....	15
Figure 2.11: components of DFIG wind turbine	15
Figure 2.12: Wind turbine drive train model in DigSilent.....	16
Figure 2.13: PSHP connected to single machine infinite bus (SMIB) in generating model, a DFIM-based, b SM-based.....	16
Figure 2.14: Power system stabilizer block diagram.....	Error! Bookmark not defined.
Figure 3.1: Per phase equivalent circuit	30
Figure 3.2: Complex power phasor S and its components.	30
Figure 4.1 Generator G2 parameters in DigSilent.	54
Figure 4.2: Generator G2 load flow parameters in DigSilent.	54
Figure 4.3: Transformer parameters in DigSilent.....	55
Figure 4.4: Transformer load flow parameters in DigSilent.....	55
Figure 4.5: Line parameters in DigSilent.	57
Figure 4.6: Line load flow parameters in DigSilent.	57
Figure 4.7: General load computed in DigSilent.	58
Figure 4.8: General load voltage dependence computed in DigSilent.	59
Figure 4.9: DFIG composite frame.	60
Figure 4.10: PQ Control with synch.....	60
Figure 4.11: Irot_Ctrl block definition.....	61
Figure 4.12: Pitch-Ctrl block definition.....	61
Figure 4.13: MPT Common model.	62
Figure 4.14: Protection block definition.	62
Figure 4.15: Protection common model.....	63
Figure 4.16: Current measurement common model.	64
Figure 4.17: Shaft block definition.	64
Figure 4.18: DFIG Composite model.....	65
Figure 4.19: DFIG basic data.	65
Figure 4.20: Composite frame for VS-PSHP system.	66
Figure 4.21: Active power reduction controller.	67
Figure 4.22: Irot_Ctrl block definition.....	67
Figure 4.23: Governor block definition.	68
Figure 4.24: MPT Common model.	68
Figure 4.25: Protection block definition.	69
Figure 4.26: PQ Control block definition.....	70
Figure 4.27: DFIM-PSHP Composite model.....	70
Figure 4.28: Composite frame for FS-PSHP system.	71
Figure 4.29: Active power reduction controller.	72
Figure 4.30: Governor block definition.	72
Figure 4.31: MPT Common model.	73
Figure 4.32: AVR block definition.	73
Figure 4.33: SM-PSHP Composite model.....	74
Figure 5.1: Original 39 Bus 10 Machine New England Power System load flow.....	76
Figure 5.2: Network bus bar voltages.....	79

Figure 5.3: Generators' rotor angles in steady state.....	80
Figure 5.4: Generator 1 rotor angle in steady state	81
Figure 5.5: Wind integrated 39 Bus system.....	82
Figure 5.6: Bus 33 voltage with wind power and without PSHP	83
Figure 5.7: Generator 1 rotor angle with wind power and without PSHP.	84
Figure 5.8: Bus 33 voltage with wind power and without PSHP for a 150ms fault at bus 30.	85
Figure 5.9: Generator 1 rotor angle with wind power and without PSHP for a 150ms fault at bus 30.....	86
Figure 5.10: unstable voltage at Bus 33 for a 450ms fault at bus 30	87
Figure 5.11: Generator 1 out of step for a 450ms fault at bus 30	88
Figure 5.12: Load flow running of the wind integrated SM-PSHP 39 bus system.	89
Figure 5.13: Bus 33 voltage with SM-PSHP and wind power for a 150ms fault at bus 30	90
Figure 5.14: Generator 1 rotor angle with SM-PSHP and wind power for a 150ms fault at bus 30.	91
Figure 5.15: Bus 33 voltage with SM-PSHP and wind power for a 450ms fault at bus 30. ...	92
Figure 5.16: Generator 1 rotor angle with SM-PSHP and wind power for a 450ms fault at bus 30.	93
Figure 5.17: Load flow running of the wind integrated DFIM-PSHP 39 bus system.....	94
Figure 5.18: Bus 33 voltage with DFIM-PSHP and wind power for a 150ms fault at bus 30.	95
Figure 5.19: Generator 1 rotor angle with DFIM-PSHP and wind power for a 150ms fault at bus 30.....	96
Figure 5.20: Bus 33 voltage with DFIM-PSHP and wind power for a 450ms fault at bus 30.	97
Figure 5.21: Generator 1 rotor angle with DFIM-PSHP and wind power for a 450ms fault at bus 30.....	98
Figure 5.22: Bus 33 voltage variation for a 150ms fault at bus 30	99
Figure 5.23: Generator 1 rotor angle variation for a 150ms fault at bus 30.....	100
Figure 5.24: Bus 33 voltage variation for a 450ms fault at bus 30	101
Figure 5.25: Generator 1 rotor angle variation for a 450ms fault at bus 30.....	102

LIST OF TABLES

Table 2.1: Comparison between stability improvement devices.	26
Table 4.1: Data of generators in the PowerFactory model ($x'' = x''_d = x''_q$).....	53
Table 4.2: Data of transformers in the PowerFactory model.....	55
Table 4.3: Data of lines in the PowerFactory model.	56
Table 4.4: Load demand.	58
Table 5.1: Network bus voltage profile in steady-state	77
Table 5.2: Network grid summary	79
Table 5.3: Generator 1 out of step.	87
Table 5.4: comparison of the difference between the maximum and minimum rotor angle values of generator 1	100
Table 5.5: variation or difference of rotor angle for generator 1	102

ABBREVIATIONS AND SYMBOLS

AC	Alternating Current
BESS	Battery Energy Storage System
CCT	Critical Clearing Time
CDPES	Centre for Distributed Power and Energy Systems
DigSILENT	Digital Simulation and Electrical Network Calculation Program
DFIG	Doubly Fed Induction Generator
DFIM	Doubly Fed Induction Machine
IEC	International Electrotechnical Commission
IEEE	Institute of Electrical and Electronics Engineers
FACTS	Flexible Alternating Current Transmission Systems
Hz	Hertz
MPPT	Maximum Power Point Tracker
PCC	Point of Common Coupling
PSHP	Pumped Storage HydroPower
PoC	Point of Connection
PV	Photo-Voltaic
RES	Renewable Energy Source
RMS	Root Mean Square
STATCOM	Synchronous Compensator
SG	Synchronous generator
SM	Synchronous Machine
SGM	Synchronous Generator Model
TR	Transformer
VI	Virtual Inertia
WTG	Wind Turbine Generator
<i>I</i>	Current
<i>V</i>	Voltage
<i>Y</i>	Admittance
<i>Z</i>	Impedance

CHAPTER ONE: INTRODUCTION

1.1. Background

Due to ongoing demand growth, electric power transmission lines have grown more restricted in recent years. Increases in the power-carrying capacity of power transmission lines are urgently needed to minimize losses and reduce voltage instability, ensuring the overall dependability and security of the power system. Due to environmental issues such as pollution, human danger, regulatory restrictions and the closeness of the fuel used to produce electricity, power-producing stations are often located distant from the load centre. As a result, utilities rely on existing arrangements of power generating and transmission lines rather than developing new transmission lines, which are susceptible to economic and environmental concerns, to satisfy the ever-increasing power demand. Furthermore, several transmission lines operate considerably below their rated thermal limits, while others are overloaded, causing voltage collapse and lowering system dependability and stability.

The power system is the complicated and huge machine composed of power sources, transformers, transmission lines, loads, reactors, and protective systems. Voltage and frequency must constantly stay within a predetermined range to maintain the power system's dependability. Consequently, all of these components function in accordance with the system's integrity. Power systems are dynamic systems evolving in reaction to increased energy demand. Increase in populations and the industrialization have led to a larger need for energy in order to fulfil basic needs and improve the quality of life. Using renewable energy, contemporary power system structure has turned out to be very complex in order to supply electricity at an affordable price with reduced carbon emissions (Remon et al., 2017).

In recent years, renewable resources have increased fast over the world in response to the ever-widening energy shortfall. Nonetheless, they provide unique operating problems for electrical networks, including transient stability concerns. Particularly, power system stability of networks having large levels of wind production is degraded and has received more attention in recent years (S. Xia et al., 2018). Power system stability issues has been addressed in with Pumped storage hydropower plants (PSHPs) based on doubly fed induction machines, and conventional PSHPs based on synchronous machines.

1.2. Problem statement

An electrical network constantly faces unexpected events; such as faults which lead to stability issues or loss of synchronism. Loss of synchronism is a severe problem in power systems because it not only has safety consequences but can also lead to cascade outages and, eventually, a blackout. In addition, blackouts cause substantial economic losses to society. Therefore, loss of synchronism must be prevented.

1.3. Research question

Small or large disturbances can also happen in a wind integrated power system. That is why they are called unexpected events.

The following essential questions are set to be answered:

- ❖ How does renewable energy integration impact the system?
- ❖ How do significant disturbances like such as a fault affect the system's stability when renewable energy is present?
- ❖ How can the system's stability be enhanced after renewable energy penetration?

1.4. Significance of problem

In power system analysis, transient stability is considered a classical problem. Its goal is to determine if a set of interconnected generators remain in synchronism when a significant disruption occurs in the bulk transmission system. Large disturbances dealt with in this work are faults after renewable energy penetration. The renewable energy considered here is wind power connected to systems having synchronous generators. Introducing wind energy into a system may have a substantial effect on the system's stability (Morel, Obara, and Morizane, 2015) (Kerdphol, Rahman, and Mitani, 2018). (S. Xia et al., 2018). Even if renewable sources have brought a great deal of value to power systems, it is essential to note the challenges faced by power system operators. These obstacles show the power electronics impact of renewable power sources on the grid. As the proportion of renewable energy sources rises because of the development of bigger wind power plants, the significance of these consequences grows (Nguyen and Mitra, 2016). However, it is unclear whether and how these events influence the voltage and rotor angle, causing the system to become desynchronized. Therefore, the stability of the power system must be maintained to prevent serious issues such as synchronization loss. Several strategies will be used to enhance the stability of electricity grids. These approaches need the incorporation of a BESS, STATCOM, PSS, or the utilization of SM-PSHP and DFIM-PSHP, as shown in this study, due to their varying impacts on rotor angle and voltage oscillations. Simulations was carried out using DigSilent software.

1.5. Research objectives

The aim of this work was to enhance the stability of the IEEE 39 bus system penetrated by wind energy with faults occurring on bus 30. Renewable energy penetration and faults are disturbances in power systems because they might affect system stability. Thus, the list of the following research objectives can be established for stability enhancement:

- ❖ The first objective is to simulate IEEE 39 bus system without renewable energy and perform load flow to see whether the system is stable or not, as it is the network upon which the stability is performed. This step is crucial as it is the initial stage of the stability analysis.
- ❖ The second objective is to integrate wind energy into IEEE 39 bus system and perform load flow to see if the system is still stable and how the integration of wind energy affects the IEEE 39 bus system.
- ❖ The third objective was to enhance of the system's stability after the fault has occurred. For this, PSHP is implemented, and three-phase faults are injected into some lines of the system. Finally, the rotor angle and voltage variation are analysed and compared with SM-PSHP and DFIM-PSHP.

1.6. Methodology

The aforementioned aim and objectives was achieved by means of the following methodology:

Literature review of power system stability enhancement. This comprises conference papers, journals, and books used to acquire expertise about power system stability improvement.

DigSILENT, the used program, can model load flow, RMS variations, and transient events. It combines models for RMS electromechanical simulations with models for instantaneous transient electromagnetic simulations. DigSILENT offers a complete collection regarding the electrical component templates for power systems research. The collection also contains models of electrical machines with their controllers, and different passive network components such as transmission lines, power transformers, static loads, and shunts. Wind and pumped storage hydropower stations also have access to a variety of generators.

IEEE 39 bus system is utilized for stability studies as it is a real power network in the New England area of the United States. This means that the solutions for using PSHPs presented in this work can be implemented in reality. In this work, the solutions for stability improvement using the pumped storage hydropower plants are done in two

study cases with various case scenarios. Each of the two cases was done in the three following steps:

- ❖ After modelling the network, the first step is to Perform the power flow with the Newton-Raphson Method as adopted by (Chatterjee & Mandal, 2017), confirming that the system is stable before the fault occurs. The main information received from the load flow analysis was the amplitude of the rotor angle of each machine and the voltage at each bus (Chakravorty et al., 2015) was essential to ensure that the network was in steady state conditions before doing any other simulation.
- ❖ As adopted in (Manjul & Rawat, 2021) to simulate network disturbance, the second step is integrating wind power and simulation of three-phase faults classified as significant disturbances.
- ❖ After faults have been simulated, an analysis of voltages and rotor angle simulation results is done as adopted by (Dai & Dourian, 2018) and (Oh et al., 2018) to determine the wind integration impact and the three-phase fault on the system stability.
- ❖ The last step is the integration of PSHPs for stability improvement. Finally, comparisons between the use of SM-PSHP and DFIM-PSHP are made to determine the best stability enhancement tool, as done by (Alizadeh Bidgoli & Gonzalez-Longatt, 2021) and (Alizadeh Bidgoli et al., 2021).

1.7. Thesis outline

This thesis was organised in five chapters as follows:

Chapter 1 It gives the introduction, which includes the background of the research topic and the problem statement. It also covers the relevance of the topic and the research questions, which outline the aims and tasks of the study explicitly.

Chapter 2 first introduces power systems as well as their components. It also defines the concept of power system stability along with the different type of stability problems found in the power system. In addition, it describes the different techniques used for power system stability studies. As wind is the main renewable energy resource used in this study, this chapter also gives a brief description of wind power. This chapter further presents a literature review of power system stability enhancement and discusses papers dealing with power system stability enhancement.

Chapter 3 presents the power system elements of the existing IEEE 39 bus system with its mathematical modelling. As renewable energy is added to the network, this section will also describe the mathematical modelling of wind generators and PSHP used in this work for stability improvement. Wind generators were chosen because they are readily accessible and environmentally sustainable. Their mathematical models

taken from DigSilent are illustrated. However, one cannot perform stability studies without power flow studies. Therefore, this section gives the mathematical formulation of the Newton-Raphson method. As chapter 2 also mentioned the use of fault to perform stability studies, the mathematical formulation of three-phase fault is given. The last part of this chapter presents a mathematical formulation of rotor angle and voltage stability.

Chapter 4 presents the computer modelling of the IEEE 39 bus system in DigSilent Powerfactory. Generators, transmission lines, transformers, loads, and shunt components are just a few of the components that make up power systems. Their parameters are given in this chapter, along with their computation for the 39-bus system. This chapter also shows how wind generators are computed and implemented in the systems mentioned above. Finally, the chapter ends with implementing both SM-PSHP and DFIM-PSHP for stability enhancement.

Chapter 5 provides simulation outcomes for the IEEE 39 bus system. DigSILENT software is used to model and manage pumped storage hydropower plants (PSHP) employing two types of machines: a doubly fed induction machine (DFIM) that is a adjustable speed (VS) generator, and a synchronous machine (SM) that is a fixed speed (FS) generator in the generating operation mode for stability enhancement. Wind power is integrated into the system, and faults are created to study the system stability when disturbances occur. Various methods are presented to improve the system stability, and three main case studies are simulated using multiple scenarios. DFIM-PSHP based and SM-PSHP based are compared with rotor angle and voltage variations to point out the impact of the disturbance and determine the best stability improvement method.

Chapter 6 is the last chapter of the study, and it discusses the study's findings and gives suggestions for future work.

CHAPTER TWO: LITERATURE REVIEW

2.1. Introduction

This chapter introduces the power system as well as its components. It also defines the concept of power system stability, the different types of power system stability, and the tools used when performing power system stability studies. An overview of renewable energy is also given, but only wind energy is discussed as it is the only renewable energy resource used in this work. This chapter further presents a literature review of power system stability enhancement.

2.2. Basic concept

2.2.1. Power system

Power system is a complex and large machine made of generators, transformers, lines, loads, protective devices etc. (Kyriakides & Polycarpou, 2015). It consists of the synchronous generator, motor, transformer, circuit breaker, cable, and other interconnected components. The energy system is a network comprised of three parts: generation, distribution, and transmission. It converts the energy source to electrical energy. The six fundamental apparatuses of the power system are the power plant, the transformer, the transmission line, the substations, the distribution line, and the distribution transformer. The power plant produces electricity for transmission by means of the transformer. Next, the transmission line transfers electricity to the multiple substations. Last but not least, electricity is transferred from the substation to the distribution transformer, that reduces the power to the proper level for the clients. Transmission and distribution are the two modes of electric power transportation (The et al., 2017). Aside from the three significant duties, an additional responsibility comprises metering and protection. The primary and secondary systems are in charge of these responsibilities. Figure 2.1 graphically depicts the elementary configuration of an electrical power system. Because electrical power networks are made of meshed transmission lines cutting areas and linking many power plants and loads, they are significantly more complex than the visual portrayal in picture 2.1. This indicates that a power system is a profitable industry that may be divided into various subsystems, including substations for power production, transmission, and distribution.

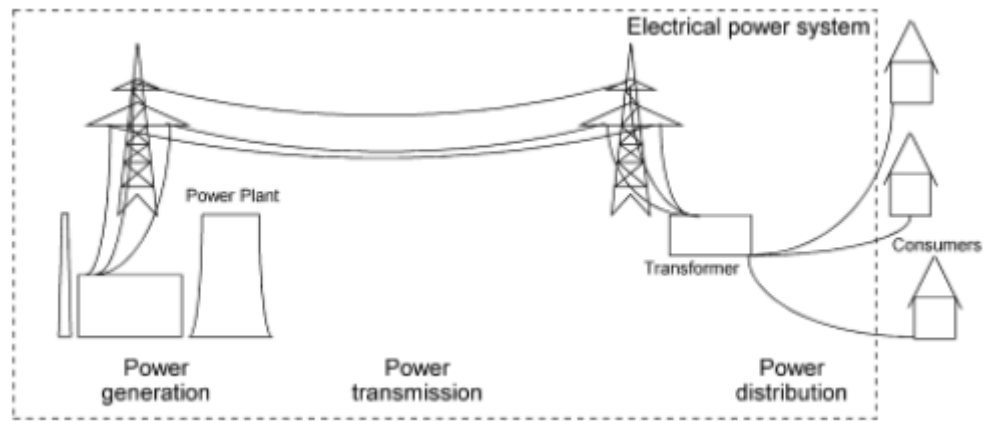


Figure 2.1: Schematic diagram of a primary configuration of an electrical power system
Adapted from (The et al., 2017)

2.2.1.1. Substation for Power Generation

Electricity can be generated at power station with Coal, oil, and gas which are burnt in power generating plant to provide thermal energy which is later converted into electricity (Grigsby, 2018). The generating station's major components are the generator and the transformer. Depending on the generator capacity, electricity may be produced in the scale of 11kV to 25kV, which is then transformed for longer distance transmission. The transformer efficiently transforms electricity from one level to another. This substation utilizes a step-up transformer to minimize line losses and permit transmission of electricity across extensive distances. In order to maintain stability, a power plant must maintain a balance between the power it generates and the electricity it consumes. In the event that power plants generate more energy than is required, the whole system might be shut down. Conversely, blackouts may occur if more power is used than is generated. Therefore, stability must be maintained at all times.

2.2.1.2. Substation for Transmission

In this substation, the overhead lines transfer electrical energy from the generation substations to the distribution substations. The primary functions of the transmission cables are to transfer energy from power plants to bulk receiving terminals and to connect two or more power plants. At a high voltage substation, the voltage is reduced to an acceptable level for the next part of the flow toward the load (Anon, 2020). Although the transmission system may be provided directly to huge industrial consumers or down at distribution substations, it must always be reliable. Thus, ensuring that stability is always maintained ensures continuity and reliability of supply.

2.2.1.3. Substation for distribution

Through the step-down transformer, the sub-transmission system links high-voltage substations to distribution substations. The sub-transmission voltage level ranges from 90 to 138 kV. (Grigsby, 2018). Some important industries are directly supplied by the sub-transmission system. Substations hold the capacitor and reactor that maintain the voltage stability of transmission lines. Distribution substations provide customers with electricity carried from power plants via transmission lines and substations. Standard low voltages are used to power ordinary homes, whereas higher voltages are used in factories, offices, and other structures depending on their size and function (Anon, 2020). Stability must always be maintained to supply customers in a reliable way, just as in the previous power generation and transmission substations.

2.2.2. Power system stability

Stability of a power system may be described in a number of ways, including the system's capacity to stay in equilibrium under normal operating circumstances and to recover equilibrium after being exposed to a disturbance. (Tavukcu & Türkay, 2017). Instability may develop even without the loss of synchronization of the power system's equipment, despite the fact that synchronization is a factor in the problem of instability. Generally, a power system is perturbed by big and tiny disturbances. Recognizing that tiny perturbations in load changes occur often, it is crucial that the system be able to adapt to these quickly changing circumstances and guarantee optimal functioning (S. W. Xia et al., 2018). Figure 2.2 shows the different types of power system stability.

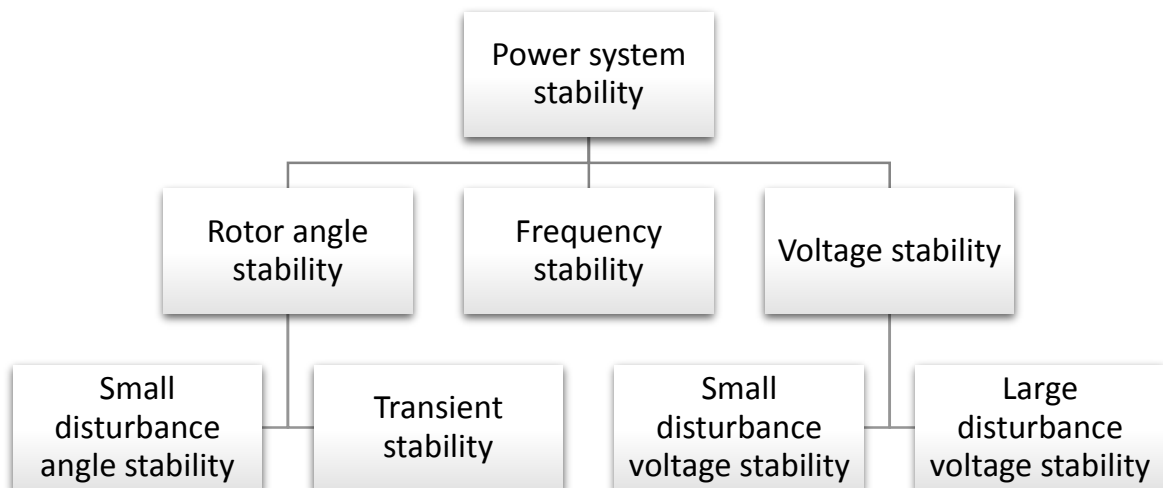


Figure 2.2: Power system stability
Adapted from (Rashid & Ali, 2015)

2.2.2.1. Rotor angle stability

Rotor angle stability refers to the ability of the power system synchronous machines to maintain synchronism even after the disturbance has occurred (Hatzargyriou et al., 2021). It usually involves analysing the variation of the rotor angle of each machine about the reference machine. The rotor angle is formed by fixed references on the stator's spinning magnetic field and the rotating shaft. When the power input fluctuates, the rotor angle is subject to a set load at the generator end, or the generator's power output is dependent on the rotor angle. This is explained by the fact that, when a system disturbance occurs, one of the machines will either accelerate or decelerate based on the rotor angle perturbation. Figure 2.2 also shows the different type of rotor angle stability, which is the subject of our investigation. Small signal stability is the capacity to sustain synchronization after a minor disruption, such as a load or generation change. Transient stability coping with major disturbances that might create fluctuations in rotor speed or angle is the system's capacity to maintain synchronization between the machines after a big disturbance, such as whether or not a renewable energy failure has occurred (Papadopoulos & Milanović, 2017). If the power system becomes stable again after a significant disruption, it automatically reaches a new state of equilibrium to preserve its integrity; otherwise, the system is said to be desynchronized (Vu & Turitsyn, 2017) because the rotor angle of the synchronous machine encounters important changes.

2.2.2.2. Voltage stability

Voltage stability is the capacity of a system to sustain steady-state voltage at each of its buses after a disruption. In most circumstances, it is dependent on the load profile function, since the increase in voltage results from the system's failure to satisfy the load demand owing to several restrictions. Loss of synchronism and transient stability are often triggered by an area's voltage instability, which trips the circuit (Xu et al., 2018). A voltage collapse, also known as a blackout or unusually low voltage, is a more serious occurrence caused by voltage instability in a significant portion of the electrical system. Figure 2.2 also shows the different type of voltage stability which are the system's capacity to sustain constant voltages in the face of small disturbances, such as incremental load shift. In contrast, big disturbance voltage stability is the system's ability to maintain stable voltages after a fault has occurred.

2.2.2.3. Frequency stability

Frequency stability is the capacity the system to maintain a steady frequency after an extreme system disruption that generates an important imbalance between generation and demand. It depends on the capacity to sustain or restore system generation and load equilibrium with minimum accidental load loss (Farmer & Rix, 2019). The

synchronous generator increases the power system's frequency as a result of exceeding the load demand, (Rahman et al., 2016).

2.2.3. Power system stability study tools

2.2.3.1. Power flow

A power flow analysis is a quantitative investigation of the electric power flow inside a system. It is the initial stage after simulating the network, as It specifies the voltage magnitude as well as the voltage angle (δ) of the buses, the active (P) and reactive (Q) power flow on the branch conductors (Aeggegn et al., 2020). Typically, two of these four values are utilised as parameters for network buses. Based on the provided quantities, the following categories may be applied to buses. (Netzberechnungssoftware, 2015):

2.2.3.1.1. PV bus

On the PV bus, the active power as well as the magnitude of the voltage are shown. This kind of node depicts generators and synchronous condensers (synchronous condensers $P=0$) with controlled active power and voltage magnitude. In addition, reactive power constraints for respective network apparatuses are used as input data to determine equipment limitations during fault.

2.2.3.1.2. PQ bus

In PQ bus, the active and reactive power are provided. This kind of bus represents machines and loads with constant values. Loads may also be configured to adjust their active and reactive power (from their nominal P_0 and Q_0 values) in response to the bus voltage to which they are connected.

2.2.3.1.3. Slack bus

In a slack bus, the amplitude and angle of the voltage cannot be changed. In conventional power flow calculations, the slack bus balances power in the system.

2.2.3.1.4. Device busses

Device busses are special busses used to represent devices with unique control conditions, such as HVDC converters, static var sources (SVSs), and so on (for example, an HVDC converter controlling active power flow at a given MW threshold, or an SVS controlling the voltage of a busbar).

In the paper by (Bannykh et al., 2018), The author used a system to calculate power flow using a unique model of power-energy flow. The nonlinear system of equations may be resolved using either the Newton–Raphson or Gauss–Seidel technique for conducting load flow analyses. The first phase of this method is to establish initial predictions about all undetermined variables (Sharma et al., 2017). Then, a Taylor

Series is generated for every power equation in the equation systems, leaving out the higher-order components.

2.2.3.2. Fault

Any anomalous condition inside a power system is known as a fault. This condition is nevertheless disturbed by sudden external or internal system modifications. A short circuit or fault occurs after the system's insulation is not responding or when a conducting item contacts a live point. Lightning, powerful winds, falling trees on the lines lines, automobiles hitting with towers, lines shorten by birds, aeroplanes touching wires, people stealing or damaging electrical installation, creatures accessing switchgear, and breaking of lines caused by overloads are among the many causes of faults. Open and short circuit remain the two main common type of faults.

2.2.3.2.1. Open circuit faults

An open circuit issue is caused by the failing of wires. They are known as series faults because they occur in sequence with the line. Such failures affect the system's reliability. The three forms of open circuit faults will be discussed in details below (AllumiaX Staff Engineers, 2019).

2.2.3.2.2. Short circuit faults

Short-circuit defects may be either symmetrical or asymmetrical. These faults are further classified into five groups. They are, in order of occurrence frequency:

- **Asymmetrical Faults** are common because they occur far more often than symmetric faults and are less severe than prior faults. Line-to-ground faults (LG) are the most common (65-70%), followed by line to line faults (5-10%) and double line to ground faults (15-20%) (Thakur, 2016). Single Line to Ground Faults occur when any of the phases is shorted to the ground, as seen in Figure 2.3.

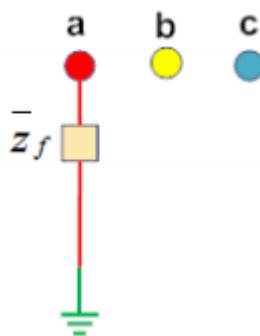


Figure 2.3: LG fault
Adapted from (NPTEL, 2019)

Line-Line Faults happen after 2 of the phases are shorted together just as seen in Figure 2.4.

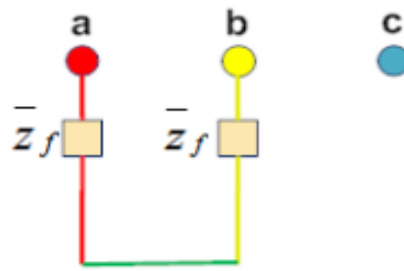


Figure 2.4: LL fault

Adapted from (NPTEL, 2019)

The line to Line-Ground Faults happen after 2 phases are shorted together and grounded, as seen in Figure 2.5.

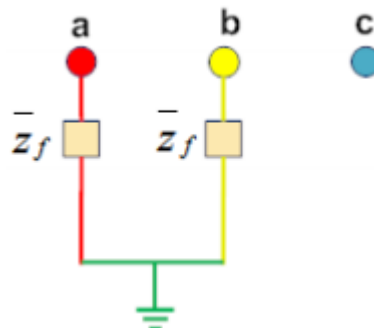


Figure 2.5: LLG fault

Adapted from (NPTEL, 2019)

- **Symmetrical Faults** only have positive sequence values. There are two types: three lines to ground LLLG faults and three lines LLL faults. In power systems, these faults occur just 1-5% of the time (Thakur, 2016). The three-phase line-ground faults occur when all 3 phases are linked and grounded, as shown in Figure 2.6.

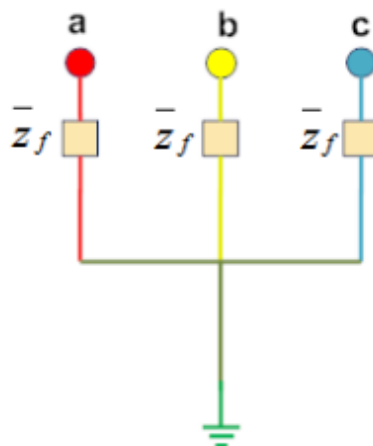


Figure 2.6: LLLG fault

Adapted from (NPTEL, 2019)

Three Phase Line to Line Faults happen after all the 3 phases are linked as seen in Figure 2.7. They are the toughest type of fault that occurring in power system. Luckily, three-phase failures are rare; approximately 1 to 5 percent of system issues are three-phase flaws (NPTEL, 2019).

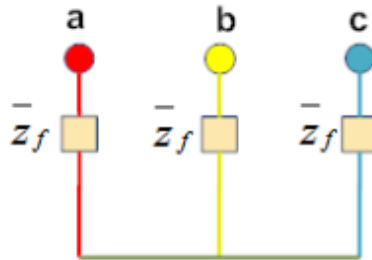


Figure 2.7: LLL fault
Adapted from (NPTEL, 2019)

2.2.3.3. Reasons for choosing DigSILENT Powerfactory

Computer simulations are also used by researchers in power system to explore load flow, and to conduct stability analysis. For complicated power-system experiments, such as simulations of wind power, these methodologies must now include strong modelling capabilities and powerful solution algorithms. The DigSILENT power system simulation software is an example of such a tool. DigSILENT can simultaneously simulate load flow, RMS variations, and transient events. It provides variants with varied degrees of information. It incorporates models for simulations of transient electromagnetic instantaneous values. This allows the models to be used to analyse grid failures and power quality issues. Additionally, DigSILENT offers a collection of component templates for power systems. This collection contains type of generators, engines, transformers, controllers, loads. As a consequence, the electrical parts of the wind turbine PSHP models are utilised as fundamental components in the present job's existing library. These components' built-in versions are DigSILENT standard models for different electrical components.

2.2.4. Wind energy

Renewable energy is derived from inexhaustible natural resources on Earth like wind and sunlight. Variable renewable energy production is connected to the electricity grid through an inverter. Interest in the addition of renewable producing resources to grid is developing rapidly in comparison to our normal centralised dispatch generation. (Muruganatham et al., 2017). This is the case of wind, the renewable energy selected for this work, as it is among the quickest-increasing renewable energy sources (European Commission, 2015). Wind farms use turbines to turn the wind's energy into

electricity. Wind energy conversion systems are available in several configurations. Single wind turbines are used to supplement pre-existing energy systems, while commercial-grade wind-powered generating systems may provide electricity to a range of users and organisations. Optionally, utility-scale wind farms may be bought on a contract or wholesale basis. Figure 2.8 shows the conversion of wind power to electrical power with the different components used for this purpose.

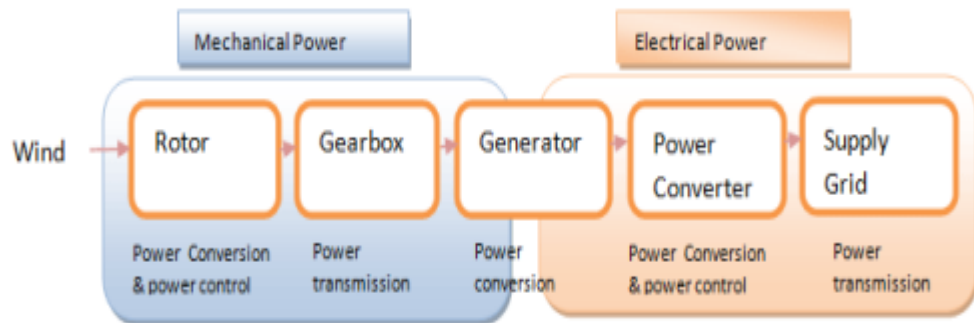


Figure 2.8: Wind power conversion
Adapted from (Rashid & Ali, 2015)

When dealing with wind turbines, induction generators are usually used. Figure 2.9 shows that in the example of grid-connected squirrel cage induction generator, both slip and rotor change with the quantity of power generated.

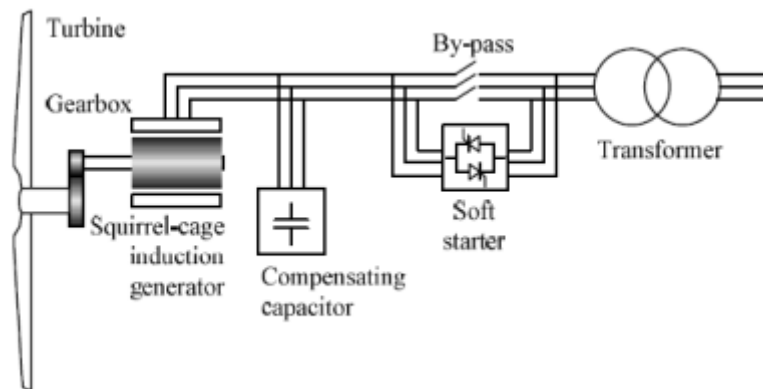


Figure 2.9: Squirrel cage induction generator connection type
Adapted from (Rashid & Ali, 2015)

The fact that the variations in the speed of the rotor are very small makes this kind of wind turbine have a constant speed. One of the objectives when developing active power control on wind turbines is to equal the conventional synchronous generators' inertia response in case the frequency becomes too low. The picture below shows the emulation power output of the inertia response.

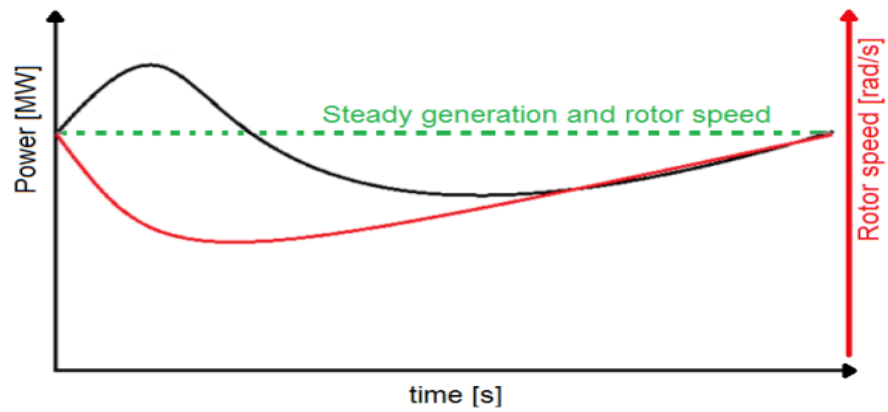


Figure 2.10: Inertia response emulation of a wind turbine generator
Adapted from (Farmer & Rix, 2019)

Currently, most wind turbines in the market are variable speed types meaning DFIG and full-scale converter types (Petinrin & Shaabanb, 2016). DFIG is made in a way that they avoid the grid from being disconnected during a fault. As seen in figure 2.11, the stator of a double-fed induction generation is connected directly to the network.

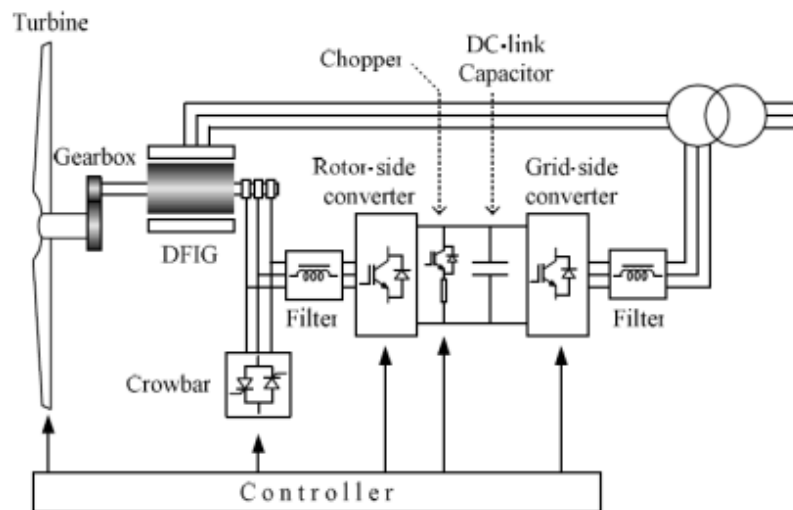


Figure 2.11: components of DFIG wind turbine
Adapted from (Rashid & Ali, 2015)

Wind energy is a clean energy source because, unlike other energy sources, it does not affect the environment. Regarding the mechanical model of the wind turbine, Figure 2.12 focuses primarily on the complicated configuration factors that contribute to its connection to the grid. Consequently, only the drive train is investigated, since this component of wind turbines has a large influence on power fluctuations.

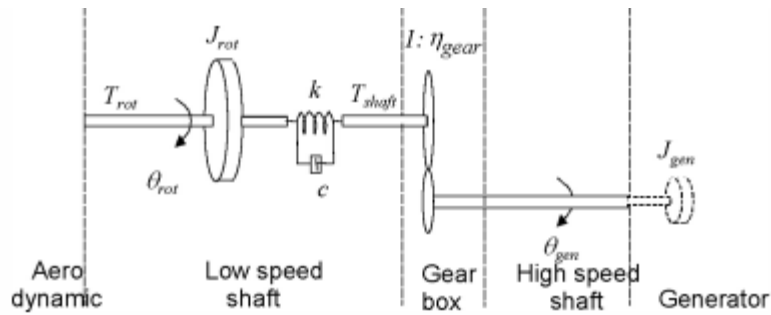


Figure 2.12: Wind turbine drive train model in DigSilent
Adapted from (Hansen et al., 2007)

2.2.5. Pumped storage hydropower

Pumped storage hydropower is a facility that stocks electricity for the purpose of load balancing. In excess electrical energy, gravitational potential energy is stored. When energy demand rises, the water that was stocked comes out to power the system's hydraulic turbines as well as an electrical generator. The upper reservoir's outlet flow may be adjusted to offer varying output power (Arabkoohsar & Namib, 2021). Pumped storage hydropower is a system with a century-long track record. By 2021, pumped storage will account for more than 90 percent of bulk electrical energy storage. As global energy networks transition to low-carbon generation, pumped storage is a critical component of grid design. To extend its future function, innovative concepts are being created that build on existing technologies (McWilliams, 2021).

A hydro turbine (HT) with a doubly-fed induction machine (DFIM) is compared to a synchronous machine (SM) of equal capacity in this study. When a DFIM is connected to an HT, it utilises a back-to-back converter consisting of a machine-side converter (MSC) and a grid-side converter (GSC), both of which have a power rating that is a fraction of the DFIM's rated power as illustrated in Figure 2.13.

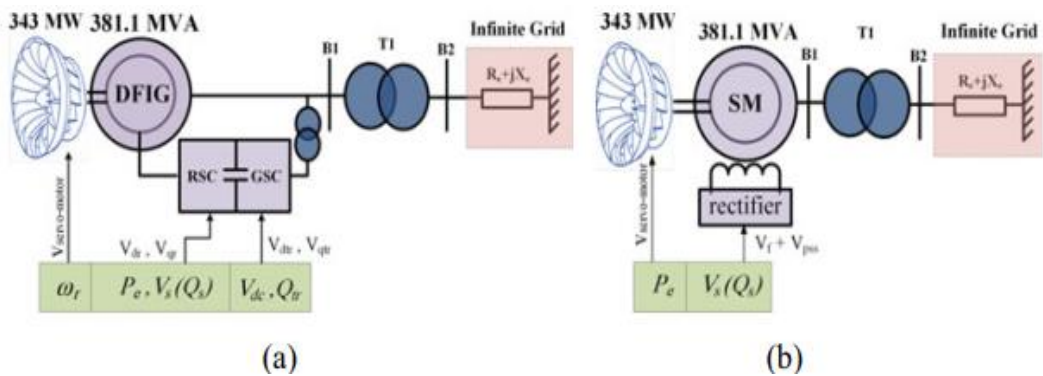


Figure 2.13: Doubly fed induction machine based (a) and Synchronous machine based (b) Pumped storage plant connection
Adapted from (Alizadeh Bidgoli et al., 2021)

The power system stabilizer (PSS), a static excitation device that changes the voltage of the stator winding and auxiliary input, is added to the excitation input to dampen local oscillations (Alizadeh Bidgoli & Bathaee, 2015). In producing mode, the turbine governor may regulate the unit's active power. However, the active power of the motor cannot be changed, and the guide vane aperture has been optimised to enhance the pump's efficiency. As a result, wicket gate throttling in pumping mode results in increased vibrations and losses. Notably, the reference gate opening of the pump is determined from the maximum efficiency point, as indicated in the hill chart (Bidgoli et al., 2015). Not only is the P-Q capability curve of a machine essential for plant controller design, but it is also necessary for grid power flow. Consequently, both the P-Q capability curves of SM- and DFIM-based PSHPs are studied. An FS unit with a salient pole synchronous machine (SM) can only adjust the plant's reactive power by modifying the machine's output voltage through the excitation system. In contrast to the FS unit, the variable speed (VS) unit that utilises the DFIM may adjust reactive power via the stator winding, the machine-side converter (MSC), and a grid-side converter (GSC). Although utilising the DFIM stator and the GSC concurrently to control reactive power may be a cost-effective solution, reactive current circulation between the GSC and the machine stator can result in uncoordinated reactive power management. Since the GSC is not included in the DFIM model, the power factor of the GSC is considered to be unity when producing the PQ capacity curve. In other words, in this experiment, DFIM can only generate reactive power on the stator side.

2.3. Power system stability enhancement

Maintaining synchronism is a necessity to ensure continuity of supply. Therefore, many researchers have provided methods for power system stability improvement. Among those methods, there are the use of battery energy storage systems, power system stabilizers, static synchronous compensators, and pumped storage hydropower plants.

2.3.1. Power System Stabilizer

In traditional power systems, Synchronous generators (SG) are the primary stability-maintaining component. However, the significant penetration of renewable energy is risky to the future of power system (Wei et al., 2017). The continued fast rise of renewable energy's high penetration has altered the operation and planning of electric power networks. (Xu et al., 2018) provide a global sensitivity analysis approach to rank the renewable energy variability impacting the voltage stability. This approach is implemented on IEEE 118 bus systems with an important proportion of renewable energy. This approach has shown that choosing the relative significance of factors yields more precise results. Recent study has shown that large levels of wind

production reduce the power system's transient stability (S. Xia et al., 2018). Large-scale grid Photovoltaic (PV) systems may potentially have an effect on the stability of the electricity supply (Yagami et al., 2014). As the PV penetration rate is one of the factors that impact voltage stability, particularly in the event of a failure, this implies that voltage sag may also be caused by a high PV penetration rate if voltage stability is not properly maintained. One may utilise the IEEE 14 Bus system to propose a method for evaluating voltage stability and calculating voltage under fault situation (Subramaniam et al., 2018). When analysing a power plant having a large PV penetration, it is found that the damping ratio increases but using power converters using synchronous power controllers (SPC) are harmoniously interacting with the grid just like synchronous machines would. This show that Photovoltaics plants having power converters that have Synchronous power converters help in frequency and voltage control, in the improvement of the oscillations damping, but mostly in a large disturbance because they limit the maximum deviation of the frequency of the system (Remon et al., 2017).

For improving inter-area stability, (Raghutu & Ramana Rao, 2020) presents an integer order power system stabilizer. The grey wolf optimization algorithm is used to optimize the settings of this controller. Comparing the action of the proposed controller to that of an ANFIS-based power system stabiliser reveals that the proposed controller effectively enhances inter-area stability. The Power System Stabilizer (PSS) lead-lag parameters are automatically modified online in (Mekhanet & Mokrani, 2020). The parameters of the proposed Self-Tuned Power System Stabilizer (STPSS) are changed in response to speed variations (gradient). As a result, it is more resistant to major disturbances than the CPSS. This controller is unique in that it adjusts its damping coefficient in real time in response to changes in its parameters (gain or time constant). In the steady state for a given load, this PSS, on the other hand, does not alter its parameters and acts like a basic CPSS. If there is a disturbance, the PSS reacts by auto-updating its settings in response to the fluctuation in the speed gradient. Simulations utilizing the proposed STPSS indicate that it consistently provides a steady response on speed variation with appropriate overshoots and settling durations. Among traditional PSSs simple to implement but under-performing and other adaptive PSSs, the suggested PSS is a solid alternative (high-performing but very complex). (Dasu, Siva Kumar, et al., 2019) proposes a novel method for building a robust Power System Stabilizer (PSS) that enhances the power system's dynamic stability. The results reveal that the suggested stabilizer increases the power system's dynamic stability throughout a wide range of operating situations. (Dey et al., 2017) provides an innovative approach to optimising the design of power system stabilisers. In large-scale interconnected systems, small-scale disturbances are the main concern. Therefore, the stability and reaction of a system must be determined by analysing the stability and performance of

small signals. By delivering additional controlled signals to generators, PSS are used to attenuate low-frequency oscillations in these large interconnected systems. Using a collective choice optimization approach, a meta-heuristic methodology based on human decision making, the optimum design of PSS was accomplished. In the paper by (Dasu, Sivakumar, et al., 2019), the Whale Optimization Algorithm (WOA) is used to develop a PSS design approach that considers the eigenvalue objective function. A new power system stabiliser (PSS) structure is presented in (Kim & Park, 2021) to enhance the stability of synchronous generators (SGs) in microgrids. Due to their diminutive size and low inertia, microgrids are especially susceptible to instability. As a consequence, the inquiry into how to include microgrid characteristics into the PSS of SGs and increase existing advantages has been completed. The PSS presented in this paper not only dampens the frequency oscillations, it also employs a synchronous impedance characteristic to provide additional damping torque dependent on the disturbance amplitude. By enhancing the SG's synchronisation power, the proposed Lyapunov energy function-based control method may also improve transient stability. For performance verification, a comparison and evaluation of the present PSS and the proposed PSS utilising PSO-generated parameters are performed. Using frequency response analysis, the influence of the proposed micro-power system stabiliser (PSS) is explored, and small-signal stability analysis and transient stability performance are confirmed using MATLAB/Simulink time-domain simulation (TDS). (Verdejo et al., 2020) offers a PSS tuning strategy based on PSO that is suited to multiple machines systems. The application of this approach to a range of test systems demonstrates the technique's usefulness and potential. MATLAB/SIMULINK is used to simulate the Power System Stabilizer (Prathap & Krishna, 2011). (Marić et al., 2021) provides an approach for improving PSS tuning for multimachine systems. The technique is based on a research of system participation characteristics and the pole placement method, while taking into consideration the system's time domain behaviour after a minor disturbance. The time-domain outputs of the synchronous generator, namely active power, speed, and rotor angle, were codified and approved. On an IEEE 14-bus system, the suggested algorithm's performance is verified. On a test system, Eigen values analysis and temporal domain analysis were performed to investigate the local mode of power oscillation in (B, 2015). The characteristics of a power system stabilizer were developed using a standard design to reduce power oscillations, and simulation results demonstrate that it is successful. (Peres et al., 2018) offers 3 mixed metaheuristics to design of power system stabilisers. In closed-loop operation, the tuning process is characterised as an optimization issue whose objective is to optimise the damping ratio coefficients. Multiple operating scenarios are used throughout the

design phase to satisfy the demand for robustness. The proposed hybrid algorithms are validated by applying them to benchmark systems.

It is also important to considerate the fact that power systems can also rely on power system stabiliser for the safety on their operation in dampening the oscillations of the generator rotor by using an auxiliary stabilizing signal to control its excitation (Kamble et al., 2017). To enhance system stability, (Gurung et al., 2019) offers a probabilistic method for generating optimum parameter values for power-system controllers such as power system stabilisers and battery energy storage devices.

2.3.2. FACTS devices

In the paper by (Kaur & Kumar, 2016), the three phase-phase balanced fault that may develop when a phase connects to another phase or in the event of insulation degradation or natural phenomena such as lightning, wind damage, or trees falling across power lines is used for transient stability analysis. All of these occurrences cause the current to climb according to their severity. It describes the enhancement of the power system using exciters, Static Var Compensators (SVC), and the inclusion of a parallel transmission line utilising the Runga technique. SVC are used in power systems to reduce oscillations and enhance the voltage stability. Also illustrates the efficacy of SVC in reducing system oscillations based on its appropriate placement. (Asija et al., 2015) also presents power system stability analysis can be done with help of three-phase balanced fault. It is usually important to notice how the system behaves in the pre fault condition and after introducing the fault. A methodology for rotor angle stability enhancement is offered in (Aguero et al., 2014) with the use of the following flexible alternating current transmission system devices (Aguero et al., 2014) using DigSilent Power Factory program for its application in electric power system stability studies. The above devices are also used for performance optimization and congestion control. They've been around for three decades and help us make more use of existing systems. They are used to monitor power flow, voltage regulation, transient stability enhancement, and oscillation damping in transmission lines (Ou et al., 2017). Because of its potential to improve power system voltage, angle, and frequency stability, FACTS has become a focal device in the power system. The same method has been used by many other researchers (Renuka & Kesavarao, 2017) (Karami & Mahmoodi Galougahi, 2019), (Asija et al., 2015), (Kaur & Kumar, 2016) regarding the efficiency of STATCOM to improve voltage stability as well as incorporate wind farms into the grid. Many experiments have been conducted using distribution FACTS and control systems to improve power quality problems in the distribution system with other power system simulation tools such as PowerWorld simulator or MATLAB Simulink. Although this study is complete, the system used only has 9 busses. This system is small to make

this methodology universal. An excitation system can be used to improve the generator power that decreases after the fault has occurred(Asija et al., 2015). Another technical approach of enhancing the power system stability is proposed in (Eidiani et al., 2011) which shows that the system can work steadily by disconnecting a number of units of a certain unit. As they can absorb important quantities of energy fastly, brake resistors may also be employed to regulate the generator's excitation. This resistor acts as a rapid artificial electrical charge and boosts power consumption when a disturbance occurs.

2.3.2.1. SVC

In (S. Bhole & Nigam, 2015) and (Li, 2016), a novel approach for appropriate Static Var Compensator (SVC) placement was presented to enhance voltage profiling, decrease power losses, decrease voltage derivations in power systems employing Voltage Stability Limit (VSL), and promote power system efficiency. The inclusion and impacts of Static Var Compensator were investigated when researching on power systems voltage stability (SVC). The model was based on the Thyristor Controlled Reactor TCR's controller being configured as variable impedance that changes with the firing angle (Naeem & Atif, 2018).For the voltage regulator of the SVC controller, the Coordinated Transformation approach is recommended. A MATLAB simulation of an SVC controller was used to assess the reaction of the SVC controller when linked to a transmission line to demonstrate the design and functioning of this approach. The results suggest that the approach is less expensive, more accurate, and has a faster reaction time (Abidin, 2020). In (AJAY et al., 2020), SVC was used to a power system to see if it might improve real power transfer capabilities in a grid. The stability study of the system demonstrates an improvement in bus voltage profile and increased power flow following fault clearing by time domain analysis.

2.3.2.2. STATCOM

In the paper by (Dorile et al., 2021), a research integrating STATCOM and SSSC demonstrates how STATCOM is utilised to enhance a wind-dominated power systems' stability via reactive power adjustment. By injecting reactive power, compensation attempts to maintain bus voltage values close to their nominal levels. In the absence of a STATCOM, the voltage at the PCC drops to almost zero when a fault occurs. However, installing a STATCOM to maintain voltage magnitudes within permissible ranges demonstrates its limits. Battery Energy Storage System and STATCOM are both used to increase the system's transient stability (Manjul & Rawat, 2021). The paper by (Kishore et al., 2020) examines the impact of adding a renewable energy source (wind) to a power system network on the system's stability. In order to include the renewable energy source, the IEEE 14 bus test system is modified. After the voltage stability study was done using continuous power flow, and the findings show that

STATCOM has a lot of potential in terms of improving system voltage stability by raising their limits. Similar observations are made in (Sengupta et al., 2018), in which a hybrid wind-PV farm that has been integrated with STATCOM. Series compensation are used to smooth out power variations. For the purpose of assessing the efficiency of STATCOM attached to the PCC, a time domain simulation is performed at several sites subjected to three-phase and line-to-ground faults. Researchers found that STATCOM enabled a large-scale hybrid wind-PV farm to become more compact and stable. In (AJAY et al., 2020), The synchronisation between the STATCOM damping stabilisers and its internal voltage controller was considered to enhance system dynamic stability and voltage regulation. For voltage stability and reactive power adjustment, a STATCOM with IGBT-based VSC that has been tuned by a genetic algorithm is used in (Applications & Transmission, 2015). The simulation results for inductive and capacitive load conditions demonstrate that STATCOM adjusted with Genetic Algorithm has the greatest performance closest to the nominal value of the voltage of 1 per unit when compared to the system without STATCOM compensation. (Kumar & Nijhawan, 2016) and (Govindasamy & Rangaswamy, 2020) explored the dynamic operation of a unique control strategy for STATCOM and SSSC. The Power System Blockset was used to simulate STATCOM and SSSC digitally in the MATLAB/Simulink environment (PSB). Two new controllers based on a decoupled current control approach are provided for the STATCOM and SSSC, and the performance of both devices when connected to a 230kV line is evaluated. The sample power transmission system is used to verify STATCOM and SSSC operation in capacitive and inductive38 modes. When the system was exposed to a load disturbance, the controllers demonstrated high voltage regulation and reactive power compensation efficiencies. (Mohanty et al., 2016). (Abaci et al., 2021) introduced a new coordinated voltage management technique for optimizing network voltage profile and minimizing STATCOM steady-state loads to efficiently support system contingencies. STATCOM enhanced the system voltage profile and reduced losses, according to modelling data. (Tanaka et al., 2019) investigates the capacity of a STATCOM to produce reactive power necessary at a wind farm under various scenarios and reports on the findings; it is observed that it enhances the system's steady-state stability limit. When used as an active voltage or VAR supporter in a system, STATCOM also enhanced transient and short-term generator stability (Manjul & Rawat, 2021), (Nagababu et al., 2019), (Petersen et al., 2017). In contrast to THYROIR-based SVCs, STATCOM relies on voltage level at the connection point to calculate the compensating current, and the compensating current does not decrease as the voltage decreases. (Zheng et al., 2017). Stability and active power compensation (Garba & Sani, 2018), low frequency oscillation (LFO) damping (Ou et al., 2017), enhancement of transient stability (Khan &

Kassas, 2019), voltage flicker control (Abaci et al., 2018), and power quality improvement (Ashok Kumar et al., 2015) are some of the most common STATCOM applications.

In (Darabian et al., 2016), The network's load was supplied by a hybrid system consisting of wind farm and photovoltaic. A line commutated HVDC connection was used to connect these services to a nine-bus power grid. In this instance, the BAT search method was used to identify the optimal solution for the objective function of Generalized Predictive Control. The practicality of the proposed GPC-BAT procedure is shown. To further test the effectiveness of this method, a PID controller managing inverter current regulators of an HVDC connection was designed. Other methodologies proposed by using either IEEE 9 bus system as done in (Kaur & Kumar, 2016), IEEE 12 bus system presented in (Remon et al., 2017), IEEE 14 bus system proposed in (Subramaniam et al., 2018).

When discussing methods enhancing the power systems' stability, it is also crucial to note that stability requirements are often assessed in terms of the critical clearance time of the fault that has occurred. The critical clearing time is the amount of time required for the system to tolerate a defect before synchronisation is lost. In other words, the critical clearance time quantifies the system's resilience against any disruption. In order to boost the system's transient stability margin, the critical clearing time might be increased. (Mrehel & Shenbisha, 2021) It examines the transient stability of power systems based on wind-type technologies. Wind turbines with constant speed generators and wind turbines with variable speed generators, among others. A STATCOM device is used as part of this research that uses the IEEE 14 bus system for improving the transient stability of Continuous Speed Wind Turbines. If the STATCOM device is connected to bus 1, the system is stable even with a failure. Furthermore, when the STATCOM is deployed, the crucial clearing time increases. In (Pico, 2017), a computational framework based on Taylor polynomials is presented, in which variables are connected to the quantity of renewable energy generated. Additionally, the essential clearing time is calculated and enhanced for superior outcomes. The research in (Firouzi et al., 2017) examines how Wind Farms are linked to the power grid utilising a unified inter-phase power controller. It addresses the connection of wind farms (WFs) to the power system utilising a power controller to enhance the transient stability of the power system. During an outage, the WF connected to UIPC functions as a STATCOM. (Petersen et al., 2017) offers an exhaustive tuning of a voltage regulation for a wind power plant with reactive power contributions. (Perilla, Torres, et al., 2020) Offers basic research on increasing the percentage of power electronic interfaced generation in electrical power systems to

improve transient stability. After a major disturbance in the system, a power-angle modulation controller is recommended to modify the wind generator type IV's post-fault active power response. Similar research (Perilla, Papadakis, et al., 2020) using the IEEE 39 bus system demonstrate that wind turbines may function using either current control or quick voltage management

2.3.3. Battery Energy Storage System (BESS)

(Som et al., 2022) proposes a synthesis-based robust control for BESS dc link microgrid voltage and frequency regulation. The operating state of the BESS' converter is affected by changes in the ac microgrid's operating condition. This controller synthesis takes into consideration variables like parametric uncertainty. For constrained parametric fluctuations, the suggested controller's stability and performance may be assured. The parameter constraints were chosen based on BESS's practical restrictions. (Shadabi & Kamwa, 2022) proposes a decentralized control technique for a hybrid energy storage system built on nonlinear dynamic droop control (NLDDC) in order to improve transient stability. The suggested method increases system transient stability in the event of grid failures while also improving primary frequency responsiveness in the event of net load fluctuation and generating outages. To solve the stability problem, (Zhang et al., 2022) provides a model predictive control, in which the voltage management and frequency control objectives are met. This design is composed of two tiers. The suggested scheme's efficacy is demonstrated by simulation results. (Su et al., 2021) proposes a distributed arrangement of batteries having synchronised control machinery to fix the stability issues. To begin, each BESS is given its own double-closed loop decoupling controller, allowing it to perform decentralized control based on its local correlation information. According to simulation data, the particle swarm optimization-optimized distributed BESS controllers are better able to interact with one another, and the system's transient stability is considerably improved. The effect of battery on distribution network stability at large amounts DG penetration is explored and researched in (Bangash et al., 2019). The observed results indicate that suitable BESS charging and discharging procedures may enhance the transient stability of the network. To preserve system equilibrium during transient fault disturbances, it would be advantageous to rapidly transition between charging and discharging modes. In (Tephiruk et al., 2018), the concert of the BESS controller for frequency/voltage fluctuations resulting from a microgrid disturbance is evaluated. Moreover, electrical unpredictability might result in power quality concerns and power outages. The DlgSILENT is used in order to build and validate the microgrid system's BESS modelling. The simulation findings demonstrate that both control strategies enable the microgrid to retain dynamic stability and appropriate frequency and voltage levels. (Cifuentes et al., 2019) offers a one-of-a-kind

optimization approach for effective battery distribution in big CBGT-containing systems. The approach enhances system stability by using batteries with voltage provision capabilities during emergencies. Stability issue is solved using an evolutionary method that accounts for transient voltages. The approach was adopted in New England's 39-busbar system. The suggested BESS allocation mechanism, when compared to standard methodologies, allows for considerable gains in system stability under crucial situations.

2.3.4. Pumped Storage Hydropower Plants (PSHP)

Power system stability is influenced differentially by modern pumped storage hydropower plants based on variable-speed doubly fed induction machines and fixed-speed synchronous machines. (Alizadeh Bidgoli & Gonzalez-Longatt, 2021) show how to model and control DFIM-based PSHPs in DIgSILENT software for variable-speed and fixed-speed PSHPs. The IEEE 10-machine 39-bus system is employed as a significant power network. By adopting DFIM-based VS-PSHP in interconnected power grids, not only are PSHP oscillation modes eliminated, but also the rotor angle and voltage transient stability of the power system is substantially enhanced. In the paper by (Alizadeh Bidgoli & Yang, 2020) comparison between a double-fed induction machine and a conventional PSHP based on a synchronous machine. As a research case, a 343 MW hydro pump-turbine coupled to DFIM with 381 MVA is compared to an SM with the same capacity, i.e. 381 MVA. The detailed model (discrete mode) in MATLAB/SimPowerSystem is used to conduct simulations under a range of conditions. Fixed speed (FS) pumped storage power plants exhibit the same low frequency power oscillations as other synchronous power plants. A power system stabiliser is meant to reduce these oscillations. in (Alizadeh Bidgoli et al., 2021). A comparison is made between the impacts of DFIM and SM-based PSHP with different PSS tuning strategies. A 343 MW hydro pump-turbine linked to DFIM with 381 MVA is utilised as a case study in contrast to an SM with the same capacity and an aggregated wind farm. Digsilent PowerFactory is used to do computations and simulations in many scenarios. In the presence of a wind farm, a modified New England test system consisting of 10 generators and 39 buses is also employed as a large power network. The results demonstrate that combining PSS and WAS in FS-PSHP can help dampen low-frequency oscillations. (Zhao et al., 2021) presents an innovative technique for improving the performance of a pumped storage unit. It might be useful in ensuring the stability of renewable energy networks containing many hydropower units. The competitive advantage of the co-optimization method in multi-machine systems is verified by comparing three measurements comprising 12 scenarios. (Majidi et al., 2020) Proposes an optimization approach for integrating tiny PSH units into WDS

operations in order to reduce WDS operating expenses related to power and water usage. The suggested model considers WDS's hydraulic restrictions and proposes the most cost-effective operating strategies based on WDS's available units. The findings point to ways to improve the test system's functioning. They also serve as a foundation for enhancing the performance of more complicated WDS systems, such as evaluating PSH design and integration. (Wang et al., 2018) proposes a strategy to take advantage of these renewable energy sources' distribution and regulation features by presenting two models.

2.4. Stability improvement summary table

Table 2.1 summarizes the various stability improvement methods by comparing the stability improvement devices (Som et al., 2022; Alizadeh Bidgoli & Yang, 2020; Karlsson, 2017; Hemeida et al., 2018).

Table 2.1: Comparison between stability improvement devices.

Devices	advantages	disadvantages
PSS	<ul style="list-style-type: none"> - Improve damping; - Improve dynamic stability; - Reduce power losses. 	<ul style="list-style-type: none"> - Tuning take time; - Low efficiency range
FACTS	<ul style="list-style-type: none"> - lower the cost of power delivery; - Reactive power support - fast voltage regulation; - Improve power transmission over lengthy AC wires; - increase the reliability of AC grids 	<ul style="list-style-type: none"> - can only carry a certain amount of power; - Conductors and equipment may be damaged by overheating if too much current is drawn; - The angle changes based on system load and generation, and a 90-degree angle are not recommended.
BESS	<ul style="list-style-type: none"> - Available in a wide range of sizes; - Good low-temperature performance; - Economically priced; - Maintenance free 	<ul style="list-style-type: none"> - Not environmentally friendly; - Slow charge; - Relatively low specific energy as compared to new systems.
PSHP	<ul style="list-style-type: none"> - Long-term durability; - Low-cost losses; - Relatively high efficiency; - Possibility of installing a massive storage capacity; - Improve damping; - Improve dynamic stability. 	<ul style="list-style-type: none"> - Upper and lower reservoirs have different geographical characteristics; - Low energy density and low power; - The time for planning and building is long, and the initial expenditure is large;

2.5. Conclusion

The components of a power system include generators, transformers, wires, loads, and protective devices. It is a big organisation that may be divided into 3 subsystems coordinated or synchronised to assure supply quality and continuity. Although faults

are used for stability analysis, load flow investigations are required while doing stability studies and simulations. Numerous researchers have concentrated on approaches that may be used for power system improvement regardless of the existence of renewable energy. However, there is a lack of understanding of which and how these events impact the voltage and rotor angle leading the system to become desynchronised. In this work, the system stability is improved by using SM-PSHP and DFIM-PSHP because of their various advantages, such as dynamic stability improvement, damping improvement, low-cost losses and the possibility of installing large storage capacity. The next chapter will also discuss the 39-bus system mathematical modelling with the wind generator along with the two types of PSHP used for stability enhancement in this work.

CHAPTER THREE: IEEE 39 BUS SYSTEM MATHEMATICAL MODELLING

3.1. Introduction

This chapter presents the IEEE 39 bus system elements with their mathematical modelling. These elements include generators, transformers and loads. This section also describes the mathematical modelling of DFIM, which are used as wind generators. As mentioned in chapter 2, stability studies cannot be performed without power flow studies. Therefore, this section gives the mathematical formulation of the Newton-Raphson method. Chapter 2 also mentioned the different types of faults. Thus, the mathematical formulation of faults is also given along with the mathematical formulation of rotor angle and voltage stability.

3.2. Power system elements of 39 bus systems

3.2.1. Synchronous generator

Synchronous generators are crucial electromechanical energy converter (Hanson & Grigsby, 2017). They provide electricity to all sectors. The application of DC to its rotor winding produces a rotor magnetic field. Synchronous generators must be driven at synchronous speed to generate an alternating current of the desired frequency as seen in the equation below (Lyshevski & Lyshevski, 2018):

$$f_e = \frac{p}{120} n_m \quad (3.1)$$

Where

f_e represents the electrical frequency in Hz;

n_m represents the rotor speed of the machine;

P represents the number of poles.

The armature response and armature winding leakage cause comparable internal voltage decreases across the synchronous reactance X_s whereas the open circuit armature voltage E_f accounts the field excitation. The impedance is given by the following equation (Lyshevski & Lyshevski, 2018):

$$Z_s = R + jX_s \quad (3.2)$$

Where X_s is the synchronous impedance and R is the armature resistance. The field voltage is given by (Lyshevski & Lyshevski, 2018):

$$E_f = V + I * Z_s \quad (3.3)$$

To specify these variables, the open circuit test and the short circuit test are conducted. During the open circuit test, the generator is spun at its rated speed with all terminals

detached from loads; the field current is set to zero before being incrementally raised; and the generator's voltage is monitored. Because the armature current is 0, the phase voltage is equal to the voltage produced internally E_A because the armature current is zero. During the short circuit test, the generator is spun at its rated speed with the field current set to zero before all terminals are shorted using ammeters. The armature current I_A is then monitored as the field current is raised in increments. The short-circuit characteristic is a straight line because the amplitude of the armature current at the shorted terminals is (Lyshevski & Lyshevski, 2018):

$$I_A = \frac{E_A}{\sqrt{R_A^2 + X_S^2}} \quad (3.4)$$

Those two tests can be summarized to find the synchronous reactance X_S at a given field current by first getting the internal generated voltage E_A from the open circuit characteristic at the field current; then getting the short-circuit current $I_{A,SC}$ at that field current from the short circuit characteristic; and find X_S with the formula (Lyshevski & Lyshevski, 2018):

$$X_S = \frac{E_A}{I_{A,SC}} \quad (3.5)$$

Since the internal machine impedance is (Lyshevski & Lyshevski, 2018):

$$Z_S = \sqrt{R_A^2 + X_S^2} = \frac{E_A}{I_{A,SC}} = X_S \quad (3.6)$$

A synchronous generator has a limit amount of power that it can supply to an infinite bus without losing synchronism. From figure 3.1, V_t is taken as the reference phasor. The following three equations (Lyshevski & Lyshevski, 2018) are used to derive the Power and Torque characteristics mathematically

$$V_t = |V_t| \angle 0^\circ \quad (3.7)$$

$$E_t = |E_t| \angle \delta \quad (3.8)$$

$$Z_s = R_a + jX_s = |Z_s| \angle \phi_s \quad (3.9)$$

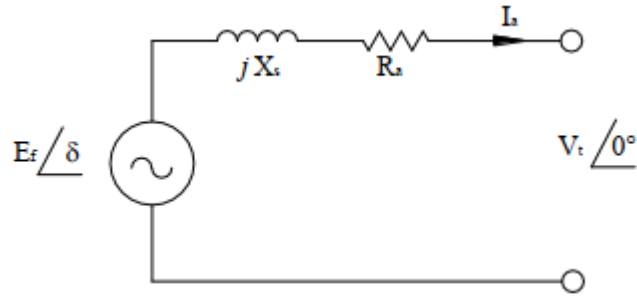


Figure 3.1: Per phase equivalent circuit

Adapted from (Lyshevski & Lyshevski, 2018)

And the per phase complex power at the machine terminals is given by (Lyshevski & Lyshevski, 2018):

$$S = V_t I_a^* \quad (3.10)$$

The conjugate of the current I_a is used to conform to the convention that leading reactive power is considered as negative and lagging reactive power is positive as seen in Figure 3.2.

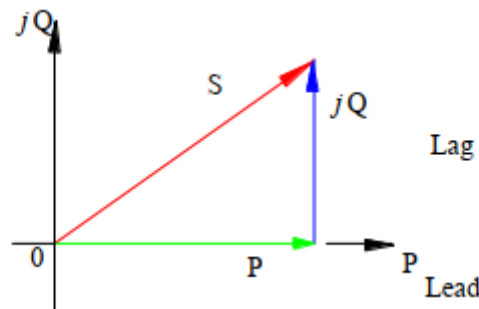


Figure 3.2: Complex power phasor S and its components

Adapted from (Lyshevski & Lyshevski, 2018)

$$I_a^* = \left| \frac{E_f - V_t}{z_s} \right|^* = \frac{E_f^*}{z_s} - \frac{V_t^*}{z_s} = \frac{|E_t| \angle -\delta}{|z_s| \angle -\varphi_s} - \frac{|V_t| \angle 0^\circ}{|z_s| \angle -\varphi_s} = \frac{|E_t|}{|z_s|} \angle (\varphi_s - \delta) - \frac{|V_t|}{|z_s|} \angle 0^\circ \quad (3.11)$$

The complex power can now be written as (Lyshevski & Lyshevski, 2018):

$$S = \frac{|E_t| |V_t|}{|z_s|} \angle (\varphi_s - \delta) - \frac{|V_t|^2}{|z_s|} \angle \varphi_s \text{ VA per phase} \quad (3.12)$$

The real power P and reactive power Q expressed as follow (Lyshevski & Lyshevski, 2018):

$$P = \frac{|E_t| |V_t|}{|z_s|} \cos(\varphi_s - \delta) - \frac{|V_t|^2}{|z_s|} \cos \varphi_s \text{ W per phase} \quad (3.13)$$

And

$$Q = \frac{|E_t||V_t|}{|Z_s|} \sin(\varphi_s - \delta) - \frac{|V_t|^2}{|Z_s|} \sin\varphi_s \text{ VAR per phase} \quad (3.14)$$

If R_a is neglected, then $Z_s = X_s$ and $\varphi_s = 90^\circ$. This gives us (Lyshevski & Lyshevski, 2018):

$$P_{3\varphi} = \frac{3|E_t||V_t|}{|X_s|} \sin\delta \text{ or } P_{3\varphi} = P_{max} \sin\delta \text{ where } P_{max} = \frac{3|E_t||V_t|}{|X_s|} \quad (3.15)$$

And

$$Q_{3\varphi} = \frac{3|E_t||V_t|}{|X_s|} \cos\delta - \frac{3|V_t|^2}{|X_s|} \quad (3.16)$$

3.2.2. Transformers

A transformer is a machine used to transfer electrical power from several circuits without altering the frequency (Del Vecchio, 2018). This is a simple definition of the term "transformer." Transformers are static devices because they lack any rotating or moving parts. They are also among the primary components of a power system that enables the transmission of electricity over great distances with little loss. Transformers are often used to transmit power from one level of voltage to another at a very high efficiency. Except for transformer losses, the power transported to the secondary side is almost identical to the one supplied to the main side (Gross, 2017). Transformers operate on ac supply and are used to increase or decrease the alternating voltages in electric power applications. PowerFactory transformers are utilised in this project. The two-winding transformer model illustrated in Figure 3.3.

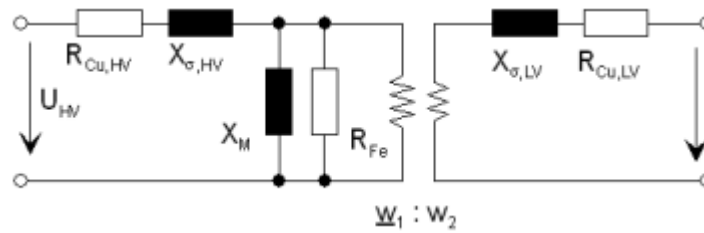


Figure 3.3: Positive sequence model of the 2-winding transformer (in Ohms)

Adapted from (DlG SILENT GmbH, 2015d)

This two-winding transformer model incorporates the HV and LV side leakage reactance and winding resistances, as well as the magnetization reactance and iron loss admittance, which are near to the ideal transformer. Figure 3.4 shows the model with relative impedances which has a complicated winding ratio of 1:1 and simulates the phase shift represented by the vector groups of the two windings.

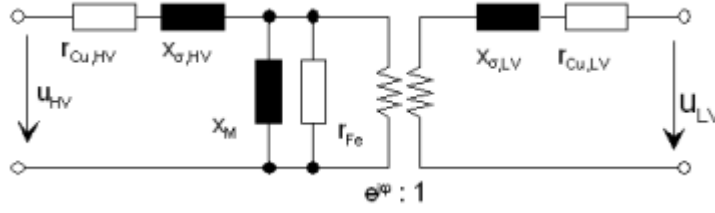


Figure 3.4: Positive sequence model of the 2-winding transformer (in p.u.)
Adapted from (DlgsILENT GmbH, 2015d)

. The following (DlgsILENT GmbH, 2015d) is a description of the relationship between the mathematical parameters in the model and the parameters in the type and element dialogs:

$$Z_{r,HV} = \frac{U_{r,HV}^2}{s_r} \quad (3.17)$$

$$Z_{r,LV} = \frac{U_{r,LV}^2}{s_r} \quad (3.18)$$

$$Z_{sc} = U_{sc}/100 \quad (3.19)$$

$$r_{sc} = \frac{P_{Cu}/1000}{s_r} \quad (3.20)$$

$$x_{sc} = \sqrt{Z_{sc}^2 - r_{sc}^2} \quad (3.21)$$

$$r_{Cu,HV} = \gamma_{R,HV,1} * r_{sc} \quad (3.22)$$

$$r_{Cu,LV} = (1 - \gamma_{R,LV,1}) * r_{sc} \quad (3.23)$$

$$x_{\sigma,HV} = \gamma_{x,HV,1} * x_{sc} \quad (3.24)$$

$$x_{\sigma,LV} = (1 - \gamma_{x,LV,1}) * x_{sc} \quad (3.25)$$

$$Z_M = \frac{1}{i_0/100} \quad (2.26)$$

$$r_{Fe} = \frac{s_r}{P_{Fe}/1000} \quad (3.27)$$

$$x_M = \frac{1}{\sqrt{\frac{1}{Z_M^2} - \frac{1}{r_{Fe}^2}}} \quad (3.28)$$

Where $z_{r,HV}$, $z_{r,LV}$ are the HV/LV side nominal impedances in Ω ;

$U_{r,HV}$, $U_{r,LV}$ are the HV/LV side rated voltages in kV;

s_r is the rated power in MVA;

P_{Cu} is the copper losses in kW;

U_{sc} is the relative short circuit voltage in %;

Z_{sc} , r_{sc} and x_{sc} are the short circuit impedance, resistance and reactance respectively in p.u;

$\gamma_{R,HV,1}$ and $\gamma_{x,HV,1}$ are the transformer short circuit resistance and reactance respectively value;

$r_{Cu,HV}$, $r_{Cu,LV}$ and $x_{\sigma,HV}$, $x_{\sigma,LV}$ are the resistances and reactances respectively on the HV/LV sides;

i_0 and P_{Fe} are the no-load current and no-load losses respectively;

r_{Fe} is the shunt resistance;

And x_M is the magnetizing impedance.

3.2.3. Transmission Lines

Transmission lines, also known as power lines, are used to link generators to loads and carry electrical power with low losses from one location to another. Transmission lines are a network of cables used to transmit electrical impulses from one location to another. This conductor system has four parameters: resistance, inductance, capacitance, and shunt conductance (Grigsby, 2018). These parameters are spread equally along the line. This is why they are also known as the transmission line's scattered parameters. An effective conductor's resistance is (Anon, 2020):

$$R = \frac{P}{I^2} \Omega \quad (3.29)$$

where P represents the power expressed in watts and I is the RMS conductor current expressed in amperes. The direct current resistance is given by the formula (Anon, 2020):

$$R_0 = \frac{\rho l}{A} \Omega \quad (3.30)$$

where ρ represents the resistivity of conductor (Ωm), l the length (m) and A is the cross-section area (m^2).

The change in the transmission line's current will cause a variation in the magnetic flux owing to the induced emf in the circuit. The magnitude of electromotive force generated relies on the rate of flux change. The transmission line's electromotive force will impede the passage of current in the conductor. Following is the equation used to determine inductance: (Anon, 2020):

$$L = \frac{\psi}{I} \quad (3.31)$$

where I is the current (A) and γ is Instantaneous flux linkages (Wb). The conductor's capacitance is defined as the current of charge per unit of potential difference and it is expressed as (Anon, 2020):

$$C = \frac{q}{v} \quad (3.32)$$

where q is the conductor Charge and v is the potential difference between the conductors. Resistance, inductance, and capacitance are measured in unit length, with the resistance measured in Ω/km , inductance measured in mH/km , and capacitance measured in F/km . The parameters are implemented in the PowerFactory program using the lumped parameter model, which breaks down a transmission line into discrete "lumps" and ignores electrical variations inside each lump. Figure 3.5 illustrates this estimation technique for representing its parameters (R, L, C) for load flow and transient analysis.

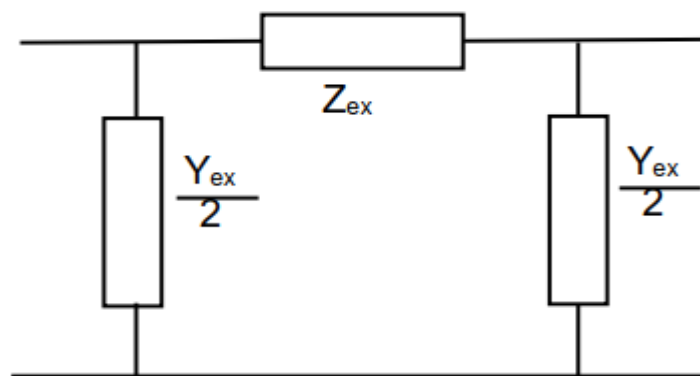


Figure 3.5: PowerFactory π -equivalent circuit for a transmission line
Adapted from (DIgSILENT GmbH, 2015d)

Equations 3.33 and 3.34 (The et al., 2017) are used to determine the impedance Z_{ex} and Y_{ex} of the PowerFactory-equivalent.

$$Z_{ex} = z_s \sinh \gamma L \quad (3.33)$$

$$Y_{ex} = \frac{2}{z_s} \tanh \frac{\gamma L}{2} \quad (3.34)$$

Where Z represents the series impedance, Y represents the shunt admittance, and L is the line length. Both equations are derived from equation 3.35 (The et al., 2017), which shows a matrix representation of the current and voltage magnitudes at transmitting and receiving ends of the line. $\gamma = \sqrt{ZY}$ while $z_s = \sqrt{\frac{Z}{Y}}$

$$\left. \begin{aligned} A &= \cosh \gamma L \\ B &= -z_s \sinh \gamma L \\ C &= \frac{-1}{z_s} \sinh \gamma L \\ D &= \cosh \gamma L \end{aligned} \right\} \quad (3.35)$$

$$\begin{bmatrix} v_r \\ i_r \end{bmatrix} = \begin{bmatrix} A & B \\ C & D \end{bmatrix} = \begin{bmatrix} v_s \\ i_s \end{bmatrix}$$

This study utilises the three-phase Digsilent transmission line concept for the transmission line. Figure 3.6 depicts the PowerFactory equivalent distributed parameters model, often known as the Lumped parameters model (π -nominal) (Karlsson, 2017). Figure 3.6 illustrates the analogous circuit for Lumped parameters model balanced three-phase line in PowerFactory. The subscriptions A, B, and C reflect the three stages of the sending s and receiving end r, respectively. The total of all admittances associated with the relevant phase is represented by Y_s , while Y_m is the negative value of the admittances

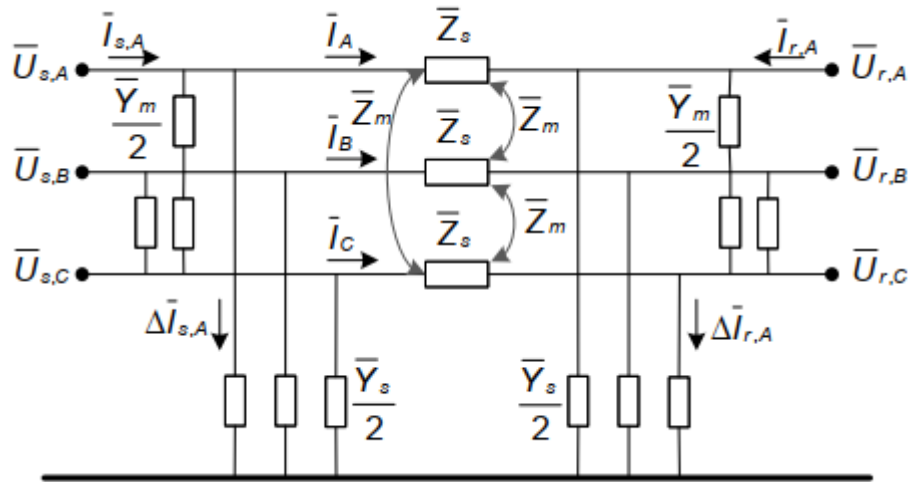


Figure 3.6: π -nominal equivalent circuit

Adapted from (DIgSILENT GmbH, 2015c)

Dimensions of the matrices are determined by phase technology. Following are the impedance and admittance matrices: (DIgSILENT GmbH, 2015c):

$$[Z_{ABC}] = \begin{bmatrix} Z_s & Z_m & Z_m \\ Z_m & Z_s & Z_m \\ Z_m & Z_m & Z_s \end{bmatrix} \quad (3.36)$$

And

$$[Y_{ABC}] = \begin{bmatrix} Y_s & Y_m & Y_m \\ Y_m & Y_s & Y_m \\ Y_m & Y_m & Y_s \end{bmatrix} \quad (3.37)$$

the voltage can be calculated as followed (DIgSILENT GmbH, 2015c):

$$\begin{bmatrix} U_{s,A} \\ U_{s,B} \\ U_{s,C} \end{bmatrix} - \begin{bmatrix} U_{r,A} \\ U_{r,B} \\ U_{r,C} \end{bmatrix} = \begin{bmatrix} Z_s & Z_m & Z_m \\ Z_m & Z_s & Z_m \\ Z_m & Z_m & Z_s \end{bmatrix} * \begin{bmatrix} I_A \\ I_B \\ I_C \end{bmatrix} \quad (3.38)$$

And the current can be calculated as followed (DIgSILENT GmbH, 2015c):

$$\begin{bmatrix} I_{s,A} \\ I_{s,B} \\ I_{s,C} \end{bmatrix} = \frac{1}{2} \begin{bmatrix} Y_s & Y_m & Y_m \\ Y_m & Y_s & Y_m \\ Y_m & Y_m & Y_s \end{bmatrix} * \begin{bmatrix} U_{s,A} \\ U_{s,B} \\ U_{s,C} \end{bmatrix} + \begin{bmatrix} I_A \\ I_B \\ I_C \end{bmatrix} \quad (3.39)$$

3.2.4. Load

The precise mix of static and dynamic network loads might be difficult to discern. The content of the load might also vary according on the season, time of day, and other factors. In the case of an HV system, the word 'load' may also apply to MV feeders or LV feeders. Figure 3.7 depicts the load model used for balanced power flow analysis.

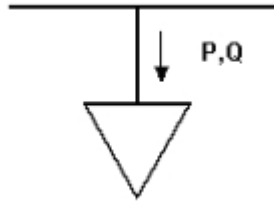


Figure 3.7: Balanced load model
Adapted from (DIgSILENT GmbH, 2015b)

The powerfactory load model used in this project is the general load which load flow calculation is defined by (Karlsson, 2017):

$$P = P_0 \left(a_P \left(\frac{v}{v_0} \right)^{e_{al}} + b_P \left(\frac{v}{v_0} \right)^{e_{al}} (1 - a_P - b_P) * \left(\frac{v}{v_0} \right)^{e_{al}} \right) \quad (3.40)$$

And

$$Q = Q_0 \left(a_Q \left(\frac{v}{v_0} \right)^{e_{al}} + b_Q \left(\frac{v}{v_0} \right)^{e_{al}} (1 - a_Q - b_Q) * \left(\frac{v}{v_0} \right)^{e_{al}} \right) \quad (3.41)$$

The impedance is calculated as (Karlsson, 2017):

$$Z = \frac{v^2}{S} \quad (3.42)$$

Where v is voltage magnitude.

3.2.5. Busbars

During load flow modelling, several boundary conditions may be used based on the kind of busbar. The most common varieties are load, generator, and swing buses. The load buses have no generator boundary condition (Karlsson, 2017). As long as the reactive power restrictions are not exceeded, the generators on the generator buses are configured to maintain their scheduled voltage. Remote control can also be used to operate the generator buses. At the swing bus, at least one generator must be installed. All generators on the swing bus are kept at a constant voltage and phase angle during the load flow computation. The powerfactory busbar model chosen for this work is the single Busbar.

3.3. DFIG-based Wind Power

In wind turbines, induction generators are often used (Anon, 2012). The wind generator chosen for this study is a Doubly fed induction generator (DFIG). The double-fed induction generator was selected for this research (DFIG). Their design seen in Figure 3.8 may be found in the DigSilent toolkit.



Figure 3.8: Doubly-Fed Induction Machine circuit

Adapted from (DIGSILENT GmbH, 2015)

When the amplitude and phase angle of the generator's AC voltage output U_{AC} on the rotor side change is as follows (Khomami Pamsari et al., 2011):

$$U_{ACr} = \left(\frac{\sqrt{3}}{2\sqrt{2}}\right) * U_{DC} * P_{WMr} \quad (3.43)$$

Where P_{WMr} is the real imaginary component of the modulation factor

$$U_{ACi} = \left(\frac{\sqrt{3}}{2\sqrt{2}}\right) * U_{DC} * P_{WMi} \quad (3.44)$$

Where P_{WMi} is the real imaginary component of the modulation factor.

It is presumed that the converter is designed using a regular six-transistor bridge and that a model sinusoidal pulse width modulation is used. Assuming that the PWM converter is lossy, the following is the relationship between AC and DC currents (DIGSILENT GmbH, 2015):

$$P_{AC} = Re(U_{AC} * I_{AC}^{\phi}) = U_{DC} * I_{DC} = P_{DC} \quad (3.45)$$

The following per-unit system are also used (DIgSILENT GmbH, 2015):

- Rated apparent power, Rated Voltage:

$$S_r, V_r, Z_b = \frac{V_r^2}{S_r} \quad (3.46)$$

- Rated electrical active power:

$$P_{er} = S_r \cos(\varphi_r) \quad (3.47)$$

- Rated mechanical power:

$$P_{mr} = P_{er} \eta_r \quad (3.48)$$

Where η_r is the rated efficiency.

- Rated mechanical torque:

$$M_r = \frac{P_{mr}}{\omega_r} = \frac{P_{mr}}{(1-S_r)\omega_n} \quad (3.49)$$

Where S_r is the rated slip and ω_n the nominal electrical angular velocity.

3.4. PSHP modelling

In the following equations, the state space equations of the hydraulic subsystem in turbine mode are given. (Bidgoli et al., 2015):

$$\dot{q}_t = (h'_s - h_t)/T_w \quad (3.50)$$

$$\dot{g} = -k_a g + k_a v_{sm} \quad (3.51)$$

Where q is the water flow, g is the gate opening, v_{sm} is the servomotor voltage, T_w is the pipe's water start time, k_a is the constant gain for servomotor modelling, and f_{eq} is the equivalent frictional coefficient. Furthermore, h_s and h_t are the net static head and net head in the turbine's operating point, respectively, and are defined as follows (Bidgoli et al., 2015):

$$\begin{aligned} h'_s &= h_s - f_{eq} q_t^2 \\ h_t &= (q_t / (g / (g_n - g_{nl})))^2 \\ T_w &= \frac{L q_n}{g' A h_n} \end{aligned} \quad (3.52)$$

where $h_s = 1$ is the static head, L is the pipe length, A is the pipe area, and g is the gravitational acceleration, which is 9.81 m/s^2 ; note that the subscripts n and n_l are nominal and no-load values, respectively. In addition, the turbine's mechanical power is defined as follows (Bidgoli et al., 2015):

$$P_m = \eta p_r h_t (q_t - q_{nl}) \quad (3.53)$$

Where $p_r = P_n(\text{MW})/S_n(\text{MVA})$ is a constant number for per unit value conversion from the turbine base to the electric machine (DFIM or SM) base; η is the efficient of the turbine. P_n and S_n represent nominal power of the turbine and apparent nominal power of the machine in generating mode, respectively.

3.4.1. Doubly-fed induction machine

By choosing the kind of simulation technique, it is possible to choose models with the appropriate degree of complexity depending on the goal of the research. This model may characterise DFIM as a PV or a PQ. DFIM can only determine as PQ when the GSC model is used in DIgSILENT. Positive stator and rotor current direction is termed a motor conversion. Moreover, all numbers and equations are expressed per unit, with the exception of time, which is expressed in seconds. The DFIM dynamic equations are computed as follows (Alizadeh Bidgoli et al., 2021):

$$\frac{1}{\omega_b} \frac{d\varphi_{qr}}{dt} = -R_r i_{dr} + s\varphi_{qr} + v_{dr} \quad (3.54)$$

$$\frac{1}{\omega_b} \frac{d\varphi_{dr}}{dt} = -R_r i_{qr} - s\varphi_{dr} + v_{qr} \quad (3.55)$$

$$\frac{d\omega_r}{dt} = \frac{1}{2H} (T_m + T_e) \quad (3.56)$$

where the d-q axis rotor currents and voltages are i_{dr} , i_{qr} , v_{dr} , v_{qr} ; R_r is the rotor resistance; s is the slip, and $\omega_b = 377$ (rad/sec); T_m , T_e , and ω_r are the mechanical torque, electric torque, and rotor speed, respectively. φ_{ds} , φ_{qs} , φ_{dr} , and φ_{qr} are the d-q axis stator and rotor flux magnitudes, which are written as follows:

$$\begin{cases} \varphi_{ds} = L_s i_{ds} + L_m i_{dr} \\ \varphi_{qs} = L_s i_{qs} + L_m i_{qr} \\ \varphi_{dr} = L_r i_{dr} + L_m i_{ds} \\ \varphi_{qr} = L_r i_{qr} + L_m i_{qs} \end{cases} \quad (3.57)$$

where i_{ds} and i_{qs} are the d-q axis stator currents, respectively; The stator and rotor inductances are L_s and L_r , respectively; the magnetizing inductance is L_m . The following equations can also be constructed if the stator transients are ignored:

$$v_{ds} = R_s i_{ds} - \varphi_{ds}$$

$$v_{qs} = R_s i_{qs} + \varphi_{ds}$$

$$(3.58)$$

$$T_e = (L_m/L_s)(-\varphi_{ds}i_{qr} + \varphi_{qs}i_{dr})$$

$$Q_s = v_{ds}i_{qs} - v_{qs}i_{ds} \quad (3.59)$$

where T_e represents electrical torque, Q_s is stator reactive power, and P_e is active power. The MSC's modulation is a sinusoidal pulse width modulation (PWM). The d-q components of rotor voltage are determined as follows for $|P_m| < 1$:

$$\begin{aligned} v_{rd} &= K_0 P_{md} U_{DC} \\ v_{rq} &= K_0 P_{mq} U_{DC} \end{aligned} \quad (3.60)$$

where K_0 is a constant coefficient that varies on modulation type and is equal to $\frac{\sqrt{3}}{2\sqrt{2}}$ for sinusoidal modulation; P_{md} , P_{mq} are d-q axis PWM coefficients that govern the MSC in DlgSILENT.

3.4.2. Synchronous Machine

Following the procedure from equation 3.61 to equation 3.65, the fifth-order model of a salient-pole synchronous machine is generated in the rotor reference frame. As part of motor conversion, the positive direction of the stator and field currents is evaluated. Time is expressed in seconds as follows (Alizadeh Bidgoli & Bathaee, 2015).

$$\frac{1}{\omega_b} \frac{d\varphi_{ds}}{dt} = -R_s i_{ds} + \omega_r \varphi_{qs} + V_{ds} \quad (3.61)$$

$$\frac{1}{\omega_b} \frac{d\varphi_{qs}}{dt} = -R_s i_{qs} + \omega_r \varphi_{ds} + V_{qs} \quad (3.62)$$

$$\frac{1}{\omega_b} \frac{d\varphi_{fd}}{dt} = -R_{fd} i_{fd} + V_{fd} \quad (3.63)$$

$$\frac{1}{\omega_b} \frac{d\varphi_{kd}}{dt} = -R_{kd} i_{kd} \quad (3.64)$$

$$\frac{1}{\omega_b} \frac{d\varphi_{kq}}{dt} = -R_{kq} i_{kq} \quad (3.65)$$

Where i_{ds} , i_{qs} , i_{fd} and i_{kd} represent the d-q axis stator, field, and damper winding currents, respectively; V_{fd} is the field winding voltage, and R_s , R_{fd} , R_{kd} and R_{kq} are the stator, field, and damper winding resistances. The rotor speed is sometimes denoted as ω_r . φ_{ds} , φ_{qs} , φ_{fd} , φ_{kd} and φ_{kq} are the flux magnitudes of the d-q axis stator, field, and damper windings, which may be represented as follows:

$$\begin{cases} \varphi_{ds} = L_d i_{ds} + L_{md} i_{fd} + L_{md} i_{kd} \\ \varphi_{qs} = L_q i_{qs} + L_m i_{qr} \\ \varphi_{fd} = L_{fd} i_{fd} + L_{md} i_{ds} + L_{md} i_{kd} \\ \varphi_{kd} = L_{kd} i_{kd} + L_{md} i_{fd} + L_{md} i_{ds} \\ \varphi_{kq} = L_{kq} i_{kq} + L_{mq} i_{qs} \end{cases} \quad (3.66)$$

Where L_d , L_q are self-inductances of d-q axis stator windings, L_{kd} , L_{kq} are self-inductances of d-q axis damper windings, L_{md} , L_{mq} are d-q axis magnetizing

inductances, and L_{fd} field self-inductance. Furthermore, the following are the swing equations for the dynamic model of the generator rotor:

$$\frac{d\omega_r}{dt} = \frac{1}{2H}(T_m + T_e) \quad (3.67)$$

$$\frac{d\delta}{dt} = \omega_r - \omega_0 \quad (3.68)$$

Where δ is the generator's rotor angle and ω_0 is the basic angular speed, which is 1 p.u.

3.5. Mathematical formulation of Newton Raphson method

The Newton Raphson Method is an iterative technique for solving several nonlinear equations with the same set of unknowns. In load flow analysis, Newton Raphson is an effective method for solving nonlinear algebraic equations. Traditionally, software systems calculated power flow using a mathematical model based on the nodal admittance equation. As stated earlier, the load flow analysis of a power system is an essential investigation. The research provides the steady-state electrical performance and power flows (real and reactive) for a certain condition (Wende et al., 2107). It is expressed with the following power flow equations (Sharma et al., 2017):

$$P_i(\text{real power}) = |V_i| \sum_{j=1}^m (|V_j| |Y_{ij}| \cos(\phi_{ij} + \delta_j - \delta_i)) \quad (3.69)$$

$$Q_i(\text{reactive power}) = -|V_i| \sum_{j=1}^m (|V_j| |Y_{ij}| \sin(\phi_{ij} + \delta_j - \delta_i)) \quad (3.70)$$

Where V_i and V_j represent the voltages at i^{th} and j^{th} busses respectively;

Y_{ij} the admittance of i^{th} and j^{th} bus;

ϕ_{ij} the admittance angle;

δ_i and δ_j are the phase angles of i^{th} and j^{th} busses respectively.

J is the jacobian matrix used to solve the Newton-Raphson method and it is expressed as (Sharma et al., 2017):

$$J = \begin{bmatrix} \frac{dP}{d\delta} & \frac{dP}{|V|} \\ \frac{dQ}{d\delta} & \frac{dQ}{|V|} \end{bmatrix} \quad (3.71)$$

and Y_{ij} is the bus matrix, and it is expressed as (Sharma et al., 2017):

$$Y_{bus} = \begin{bmatrix} Y_{11} & \dots & Y_{1j} \\ \dots & \dots & \dots \\ Y_{ji} & \dots & Y_{jj} \end{bmatrix} \quad (3.72)$$

As for the iteration algorithm, it is done in the following steps (Sharma et al., 2017)::

The 1st step considers one bus as slack bus in a system whose both voltage and phase angle are 1 < 0 and assumes all the other buses as PQ and PV buses.

In the 2nd step, for the r^{th} iteration,

$$P_i^r = |V_i|^r \sum_{j=1}^m (|V_j| |Y_{ij}| \cos(\phi_{ij} + \delta_j - \delta_i)) \quad (3.73)$$

$$Q_i^r = -|V_i|^r \sum_{j=1}^m (|V_j| |Y_{ij}| \sin(\phi_{ij} + \delta_j - \delta_i)) \quad (3.74)$$

Let,

$$e_i^r = |V_i|^r \cos \delta_i^r \quad \text{and} \quad f_i^r = |V_i|^r \sin \delta_i^r \quad (3.75)$$

$$G_{ij} = |Y_{ij}| \cos \phi_{ij} \quad (3.76)$$

$$B_{ij} = |Y_{ij}| \sin \phi_{ij} \quad (3.77)$$

Then calculate,

$$\Delta P_i^r = P_i(\text{scheduled}) - P_i^r \quad \text{for PQ and PV buses} \quad (3.78)$$

$$\Delta Q_i^r = Q_i(\text{scheduled}) - Q_i^r \quad \text{for PQ buses} \quad (3.79)$$

In this step, if all the ΔP_i^r and ΔQ_i^r values are lower than the threshold, iterations are terminated, P1 and Q1 are computed, and the solution is found.

In the 3rd step, if the convergence criteria is not found, the Jacobian matrix elements are calculated;

In the 4th step, the voltage magnitude and phase angles are corrected.

In the 5th step, the voltage magnitude and phase angles are updated as follow:

$$|V_i|^{(r+1)} = |V_i|^r + \Delta |V_i|^r \quad (3.80)$$

$$\delta^{(r+1)} = \delta^r + \Delta \delta^r \quad (3.81)$$

Step 2 is repeated till the convergence is obtained.

3.6. Mathematical formulation of three phase line to line fault

In this kind of fault, all three phases are simultaneously short-circuited. The network is analysed phase by phase since it maintains equilibrium. Similar currents are present in the other two phases, although they are 120 degrees out of phase (Thakur, 2016). A network fault is simulated by connecting network impedances at the site of the defect. Then, Thevenin's analogous network, as viewed from the position of the problem, is

used to repair the faulty network. Figure 3.9 shows an example of bus in an n-bus power system network.

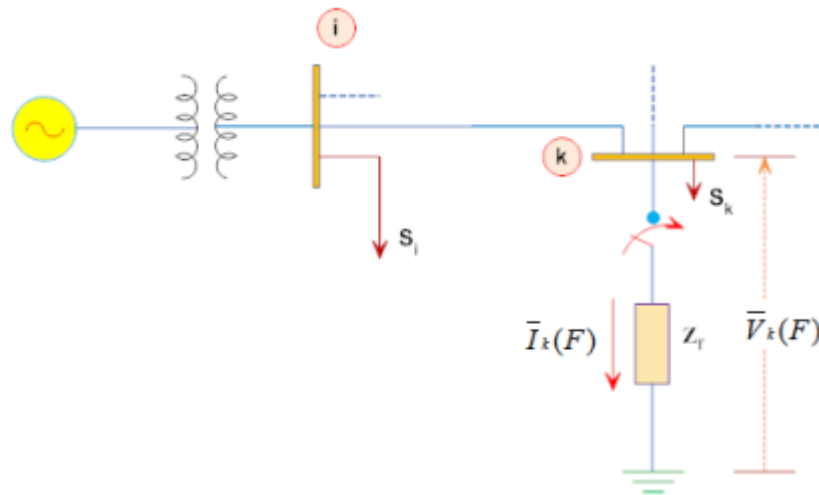


Figure 3.9: Fault at k^{th} bus

Adapted from (NPTEL, 2019)

A balanced three-phase fault is also expected to occur at the k^{th} bus, as illustrated in the picture above, through a fault impedance \bar{Z}_f . A pre-fault load flow provides information regarding the pre-fault bus voltage. Let $[\bar{V}_{Bus}(0)]$ be the pre-fault bus voltage vector, which is equal to $[\bar{V}_1(0) \dots \bar{V}_k(0) \dots \bar{V}_n(0)]^T$ p.u. Due to the passage of large currents across the transmission lines, the fault at the k^{th} bus will induce a change in the voltage of all the buses $[\Delta\bar{V}_{Bus}]$. By supplying a voltage $\bar{V}_k(0)$ to the k^{th} bus and short-circuiting all other voltage sources, this change may be computed. The equivalent impedances are used to replace the sources and loads, as seen in Figure 3.10.

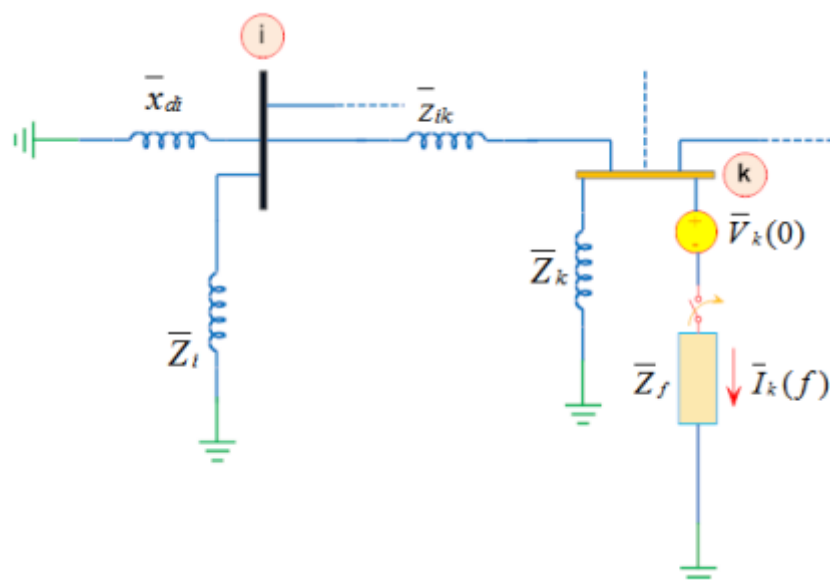


Figure 3.10: Network representation for calculating $[\Delta\bar{V}_{Bus}]$

Adapted from (NPTEL, 2019)

The picture also shows \bar{Z}_i and \bar{Z}_k which are the equivalent load impedances for bus i and k , respectively, and \bar{Z}_{ik} is the line impedance between i^{th} and k^{th} buses. The suitable generator reactance is \bar{x}_{di} , the fault impedance is \bar{Z}_f , the fault current is $\bar{I}_k(F)$ and the prefault voltage at the k^{th} bus is $\bar{V}_k(0)$. The bus voltages owing to a failure may be calculated using the superposition theorem below as the sum of prefault bus voltages and the change in bus voltages due to fault (NPTEL, 2019):

$$[\bar{V}_{Bus}(F)] = [\bar{V}_{Bus}(0)] + [\Delta\bar{V}_{Bus}] \quad (3.82)$$

Where

$[\bar{V}_{Bus}(F)]$ is the bus voltage vector during fault expressed as $[\bar{V}_1(F) \dots \bar{V}_i(F) \dots \bar{V}_n(F)]^T$ (NPTEL, 2019);

$[\bar{V}_{Bus}(0)]$ is the prefault bus voltage vector expressed as $[\bar{V}_1(0) \dots \bar{V}_i(0) \dots \bar{V}_n(0)]^T$ (NPTEL, 2019);

$[\Delta\bar{V}_{Bus}]$ is the bus voltage vector of change expressed as $[\Delta\bar{V}_1 \dots \Delta\bar{V}_k \dots \Delta\bar{V}_n]^T$ (NPTEL, 2019)

Also the bus injected current $[\bar{I}_{Bus}]$ can be expressed as (NPTEL, 2019):

$$[\bar{I}_{Bus}] = [\bar{Y}_{Bus}][\bar{V}_{Bus}] \quad (3.83)$$

Where $[\bar{V}_{Bus}]$ is the bus voltage vector and $[\bar{Y}_{Bus}]$ is the bus admittance matrix.

When considering all the bus currents besides the faulted bus k which is zero, the node equation for the network of the picture above can be expressed as (NPTEL, 2019):

$$\begin{bmatrix} 0 \\ \vdots \\ -\bar{I}_k(F) \\ \vdots \\ 0 \end{bmatrix} = \begin{bmatrix} \bar{Y}_{11} & \dots & \bar{Y}_{1k} & \dots & \bar{Y}_{1n} \\ \vdots & & \vdots & & \vdots \\ \bar{Y}_{k1} & \dots & \bar{Y}_{kk} & \dots & \bar{Y}_{kn} \\ \vdots & & \vdots & & \vdots \\ \bar{Y}_{n1} & \dots & \bar{Y}_{nk} & \dots & \bar{Y}_{nn} \end{bmatrix} * \begin{bmatrix} \Delta\bar{V}_1 \\ \vdots \\ \Delta\bar{V}_k \\ \vdots \\ \Delta\bar{V}_n \end{bmatrix} \quad (3.84)$$

The fault current $\bar{I}_k(F)$ is taken as a negative current entering the bus as it is leaving the bus. Hence (NPTEL, 2019)

$$[\bar{I}_{Bus}(F)] = [\bar{Y}_{Bus}][\Delta\bar{V}_{Bus}] \quad (3.85)$$

$[\Delta\bar{V}_{Bus}]$ Can be calculated as (NPTEL, 2019):

$$[\Delta\bar{V}_{Bus}] = [\bar{Y}_{Bus}]^{-1}[\bar{I}_{Bus}(F)] = [\bar{Z}_{Bus}][\bar{I}_{Bus}(F)] \quad (3.86)$$

Where $[\bar{Z}_{Bus}]$ is the impedance matrix $[\bar{Y}_{Bus}]^{-1}$

Substituting the expression of from equation 6.4 in equation 6.5 one can write (NPTEL, 2019):

$$[\bar{V}_{Bus}(F)] = [\bar{V}_{Bus}(0)] + [\bar{Z}_{Bus}(F)][\bar{I}_{Bus}(F)] \quad (3.87)$$

Expanding the above equation one can write (NPTEL, 2019):

$$\begin{bmatrix} \bar{V}_1(F) \\ \vdots \\ \bar{V}_k(F) \\ \vdots \\ \bar{V}_n(F) \end{bmatrix} = \begin{bmatrix} \bar{V}_1(0) \\ \vdots \\ \bar{V}_k(0) \\ \vdots \\ \bar{V}_n(0) \end{bmatrix} + \begin{bmatrix} \bar{Z}_{11} & \cdots & \bar{Z}_{1k} & \cdots & \bar{Z}_{1n} \\ \vdots & & \vdots & & \vdots \\ \bar{Z}_{k1} & \cdots & \bar{Z}_{kk} & \cdots & \bar{Z}_{kn} \\ \vdots & & \vdots & & \vdots \\ \bar{Z}_{n1} & \cdots & \bar{Z}_{nk} & \cdots & \bar{Z}_{nn} \end{bmatrix} * \begin{bmatrix} 0 \\ \vdots \\ -\bar{I}_k(F) \\ \vdots \\ 0 \end{bmatrix} \quad (3.88)$$

The bus voltage of k^{th} bus can be written as (NPTEL, 2019):

$$\bar{V}_k(F) = \bar{V}_k(0) - \bar{Z}_{kk}\bar{I}_k(F) \quad (3.89)$$

Also from the above picture (NPTEL, 2019):

$$\bar{V}_k(F) = \bar{Z}_F\bar{I}_k(F) \quad (3.90)$$

For bolted fault $\bar{Z}_F = 0$ hence $\bar{V}_k(F)$ thus the bolted fault current can be expressed as (NPTEL, 2019):

$$\bar{I}_k(F) = \frac{\bar{V}_k(0)}{\bar{Z}_{kk}} \quad (3.91)$$

For faulty with non-zero fault impedance \bar{Z}_F , the fault current can be expressed as (NPTEL, 2019):

$$\bar{I}_k(F) = \frac{\bar{V}_k(0)}{\bar{Z}_{kk} + \bar{Z}_F} \quad (3.92)$$

Thevenin's impedance or open circuit impedance of the network as observed from the faulty bus k is the amount \bar{Z}_{kk} in equations 6.8, 6.10 and 6.11. The bus voltage following a fault for unfaulted or healthy buses may be calculated as (NPTEL, 2019):

$$\bar{V}_i(F) = \bar{V}_i(0) - \bar{Z}_{ik}\bar{I}_k(F) \quad \forall i = 1, 2, \dots, n. \quad i \neq k \quad (3.93)$$

$\bar{V}_i(F)$ can then be expressed as (NPTEL, 2019):

$$\bar{V}_i(F) = \bar{V}_i(0) - \frac{\bar{Z}_{ik}}{\bar{Z}_{kk} + \bar{Z}_F} \bar{V}_k(0) \quad (3.94)$$

The fault current $\bar{I}_{ij}(F)$ flowing in the line connecting i^{th} and k^{th} bus can be calculated as (NPTEL, 2019):

$$\bar{I}_{ij}(F) = \frac{\bar{V}_i(F) - \bar{V}_j(F)}{\bar{Z}_{ij}} \quad (3.95)$$

Where \bar{Z}_{ij} represents the impedance of line connecting buses i and j.

3.7. Mathematical formulation of power system stability

Mathematical formulation of rotor angle and voltage stability are expressed in this part.

3.7.1. Mathematical formulation of rotor angle stability

3.7.1.1. Swing equation

When the mechanical and electrical torques acting on the rotor are out of equilibrium, the net torque inducing acceleration or deceleration is described in the equation 3.96 (NTEKA, 2013) with T being the acceleration torque and T_m and T_e the mechanical and electrical torque respectively.

$$T = T_m - T_e \quad (3.96)$$

If we consider f as the frequency, $\dot{\theta}_m$ the mechanical angle in radian and rpm the revolution per minute, the electrical angle (Kehinde, 2012) related to the mechanical is expressed as:

$$\dot{\theta}_e = \frac{60f}{rpm} \dot{\theta}_m \quad (3.97)$$

The same electrical angle is also expressed in the electrical angular position equation (Kehinde, 2012) as:

$$\delta \dot{=} \theta_e - \omega_0 t \quad (3.98)$$

Where ω_0 is the rated synchronous speed expressed in rad/sec, t is the time in sec, ω_0 the electrical angle in rad and δ the rotor angle in radians with respect to the reference machine. The angular acceleration comes from the second derivative of equation (14) and is expressed (Kehinde, 2012) as:

$$\frac{d^2\delta}{dt^2} = \frac{d^2\dot{\theta}_e}{dt^2} \quad (3.99)$$

The synchronous machine is also under the influence of a net torque is computed as followed (Kehinde, 2012):

$$T = \frac{WR^2}{g} \alpha \quad (3.100)$$

Where WR^2 represents the moment of inertia in $\text{kg}\cdot\text{m}^2$ (R being the radius of gyration and W the weight of rotating parts) and α the mechanical angular acceleration (Kehinde, 2012) in rad/s^2 expressed as follow:

$$\alpha = \frac{d^2\dot{\theta}_m}{dt^2} = \frac{rpm}{60f} \frac{d^2\dot{\theta}_e}{dt^2} \quad (3.101)$$

the following expression (Kehinde, 2012) is the second derivative of equation 7.2 combined with equation 7.5 and equation 7.6

$$T = \frac{WR^2}{g} \frac{rpm}{60f} \frac{d^2\dot{\theta}_e}{dt^2} \quad (3.102)$$

Knowing that the kinetic energy expression is:

$$K.E = \frac{1}{2} \frac{WR^2}{g} \omega_0^2 \quad (3.103)$$

Where $\omega_0 = 2\pi \frac{rpm}{60} = 2\pi f$

The inertia constant H is expressed as (Kehinde, 2012):

$$H = \frac{\text{kinetic energy at rated speed}}{\text{Base VKA}} \quad (3.104)$$

$$\text{Thus } H = \frac{1}{2} \frac{WR^2}{g} \left(2\pi \frac{rpm}{60}\right)^2 \frac{1}{\text{Base VKA}} \quad (3.105)$$

If the base torque is expressed as (NTEKA, 2013):

$$\dot{T}_{Base} = \frac{\text{Base KVA}}{2\pi \left(\frac{rpm}{60}\right)} \quad (3.106)$$

the following expression allowing to get torque \bar{T} in per unit is the substitution of the combination of equation 7.10 with equation 7.11 into equation 7.7.

$$\frac{T}{\dot{T}_{Base}} = \bar{T} = \frac{H}{\pi f} * \frac{d^2\delta}{dt^2} \quad (3.107)$$

Rewriting equation 7.12 gives the following

$$\bar{T}_m - \bar{T}_e = \frac{H}{\pi f} * \frac{d^2\delta}{dt^2} \quad (3.108)$$

Knowing that $\bar{P}_m = \omega \bar{T}_m$ and $\bar{P}_e \equiv \omega \bar{T}_e$ with being the synchronous speed in per unit, if speed deviation is neglected the following expression (Kehinde, 2012) can be given:

$$\bar{P}_m - \bar{P}_e = \frac{H}{\pi f} * \frac{d^2\delta}{dt^2} \quad (3.109)$$

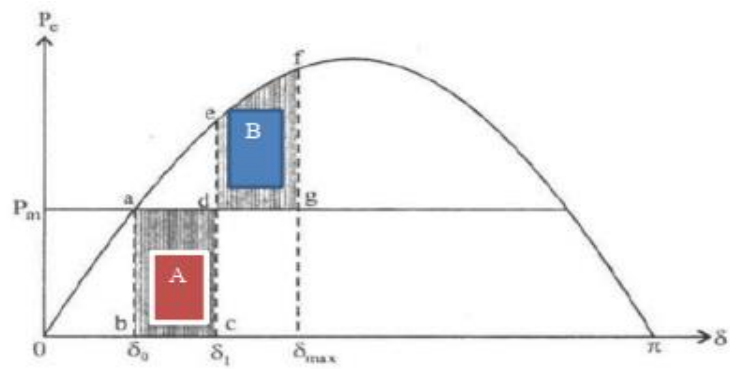
Where \bar{P}_m is the mechanical power and \bar{P}_e the electrical power.

Equation (24) and equation (25) called swing equations (Kehinde, 2012) can be used and modified to obtain:

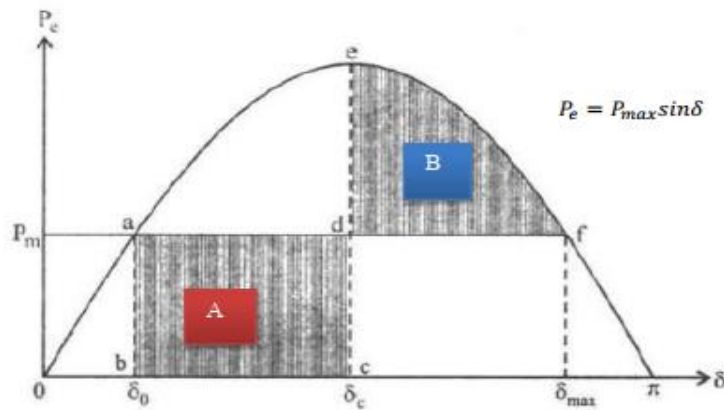
$$\frac{2H}{\omega_s} * \frac{d^2\delta}{dt^2} = \bar{P}_m - \bar{P}_e = \bar{P} \quad (3.111)$$

3.7.1.2. Critical clearing time

The $P - \delta$ curve is illustrated in Figure 3.11. It is worth noting that $P_m = P_e$ in the steady state.



a



b

Figure 3.11: Calculating CCT using Equal Area Criterion
Adapted from (Kehinde, 2012)

If a three-phase failure happens close to the generator bus on a radial transmission line, the power generation transmitted over the line to the external bus is reduced to zero, but the mechanical energy is unaffected. The equipment is believed to have restored to its initial condition once the error has been rectified. The unit is driven by the mechanical energy represented by the region abcd in Figure 3.11, and the rotor angle direction switches from δ_0 which is the original rotor angle to δ_1 , assuming the fault is cleared at δ_1 . The operation point then shifts from c to e. The region defg is created at point f. The rotor returns to point f and settles at point a, with $P_m = P_e$. Stability is retained if area A is equal to area B. The clearing angle δ_1 is the fault clearing angle, and the fault clearing time t is the time it takes to clear the fault. The equal area criteria is based on this. When the fault clearance time is changed from t to t_c , and area δ_1 equals area δ_c , t equals t_c , and area A equals area B, additional increases in t would not hold area A equal to area B. Figure 20(b) depicts this. The critical clearing time (CCT) is represented by the value of t_c at this point, and the critical clearing angle is represented by δ_c . The power flow path varies as the fault travels closer to the reference bus, and the CCT changes with gradual reduction. If the equal area condition

is met, area A equals area B, so area A and Area B can be determined as follows (Kehinde, 2012) from figure 3.11(a):

$$A = \int_{\delta_0}^{\delta_c} (P_m - 0) d\delta = P_m(\delta_c - \delta_0) \quad (3.112)$$

$$B = \int_{\delta_c}^{\delta_{max}} (P_{max} \sin \delta - P_m) d\delta \quad \text{since } P_e = P_{max} \sin \delta \quad (3.113)$$

$$B = P_{max}(\cos \delta_c - \cos \delta_{max}) - P_m(\delta_{max} - \delta_c) \quad (3.114)$$

Having in mind that area A equals area B and $\delta_{max} = \pi - \delta_0$

$$\delta_c = \cos^{-1} \left[\frac{P_m}{P_{max}} (\pi - 2\delta_0) - (\cos \delta_0) \right] \quad (3.115)$$

When the fault occurs, the swing equation from equation 7.14 becomes:

$$\frac{H}{\pi f} * \frac{d^2 \delta}{dt^2} = P_m \quad \text{when } P_e = 0 \quad (3.116)$$

When equation 7.20 is integrated twice on both sides, equation 7.20 becomes:

$$\delta_c = \frac{\pi f}{2H} P_m t^2 + k \quad (3.117)$$

$$\text{At } t = 0, \delta_0 = \delta \text{ hence } k = \delta_0 \quad (3.118)$$

$$\text{Hence } \delta_c = \frac{\pi f}{2H} P_m t^2 + \delta_0 \quad (3.119)$$

As δ_c represents the critical clearing angle, the critical clearing time is given as (Kehinde, 2012):

$$CCT = t_c = \sqrt{\frac{2H(\delta_c - \delta_0)}{\pi f P_m}} \quad (3.120)$$

$$\delta_c = \cos^{-1}((\pi - 2\delta_0) \sin \delta_0 - \cos \delta_0) \quad (3.121)$$

Where CCT represents the critical clearing time, δ_0 is the critical clearing angle and H is the inertia. The critical clearing time for multi-machine systems is determined by increasing the fault clearing time until the system is about to lose synchronism, at which point additional increases would cause the system to fall out of phase (Kehinde, 2012).

3.7.2. Mathematical formulation for voltage stability

Voltage stability problems are often studied as steady-state issues with power flow modelling as the principal research tool and simulated "snapshots" in time following an outage or during load build-up. PV and VQ curves are two further power flow-based

methodologies frequently employed in addition to these post-disturbance power flows. These two approaches provide steady-state loadability limitations based on voltage stability. For an approximation study, conventional load flow algorithms can be employed. P–V curves are useful for studying radial systems and for conceptual research of voltage stability as seen Figure 3.12

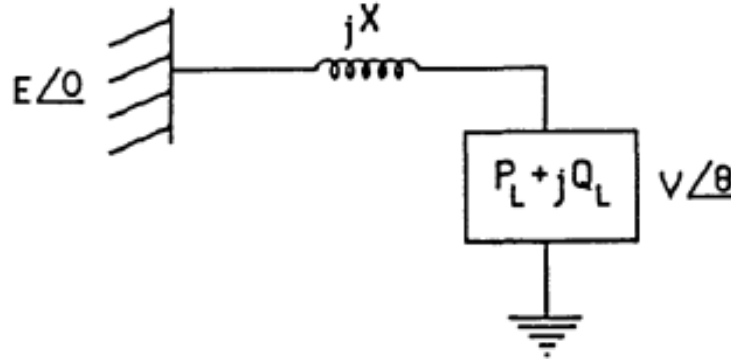


Figure 3.12: Single load served by an infinite bus
Adapted from (Christy, 1990)

The load voltage is expressed as follow (Yadav et al., 2014):

$$V = \sqrt{\frac{(E^2 - 2Q_L X) - \sqrt{(2Q_L X - E^2)^2 - 4X^2(Q_L^2 - P_L^2)}}{2}} \quad (3.122)$$

Equation 3.130 is obtained from figure 3.12 in the following steps (Yadav et al., 2014) (Araga & Aioboman, 2021):

- ❖ Active power at load bus is:

$$0 = P_{Generation} - P_{Load} - P_{Injection} = -P_L - VE\left(\frac{1}{X}\right) \cos(-\theta - 90) \quad (3.123)$$

- ❖ Reactive Power at load bus is:

$$0 = Q_{Generation} - Q_{Load} - Q_{Injection} = -Q_L - VE\left(\frac{1}{X}\right) \sin(-\theta - 90) - V^2\left(\frac{1}{X}\right) \quad (3.124)$$

- ❖ Solving for $\cos(-\theta - 90)$ and $\sin(-\theta - 90)$:

$$\cos(-\theta - 90) = \frac{P_L X}{VE} \quad (3.125)$$

And

$$\sin(-\theta - 90) = \frac{-(Q_L X + V^2)}{VE} \quad (3.126)$$

❖ Using the $\cos^2 x + \sin^2 x = 1$ identity;

$$1 = \left(\frac{Q_L X + V^2}{VE}\right)^2 + \left(\frac{P_L X}{VE}\right)^2 \quad (3.127)$$

❖ Then solving for V^2 ;

$$V^4 + V^2(2Q_L X - E^2) + Q_L^2 X^2 + P_L^2 X^2 = 0 \quad (3.128)$$

$$V^2 = \frac{(E^2 - 2Q_L X) \pm \sqrt{(2Q_L X - E^2)^2 - 4X^2(Q_L^2 - P_L^2)}}{2} \quad (3.129)$$

Knowing that voltage should be positive, V is the positive square root of V^2 and it is expressed as:

$$V = \sqrt{\frac{(E^2 - 2Q_L X) \pm \sqrt{(2Q_L X - E^2)^2 - 4X^2(Q_L^2 - P_L^2)}}{2}} \quad (3.130)$$

As previously stated, the fundamental phenomenon of voltage instability may be shown if this equation is applied to a rising load. The so-called "P-V curve" depicts this phenomenon. Figure 3.13 depicts the load bus voltage in relation to the load active power when the load is increased at unity power factor.

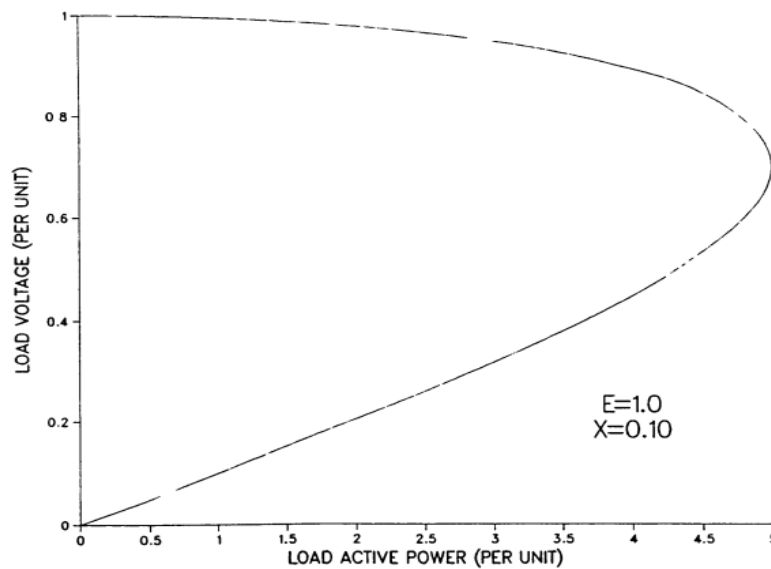


Figure 3.13: P- V curve
Adapted from (Christy, 1990)

3.8. Conclusion

In this chapter, mathematical modelling of the power system apparatuses used for this work has been presented. Those components are synchronous generators, transformers, transmission lines, general load and generators. Mathematical modelling of SM-PSHP and DFIM-PSHP was also done as they are the power system stability enhancement components chosen in this work. To study the stability of a network, load flow studies must first be done. As Newton Raphson's method was the load flow analysis method chosen for this work, its mathematical formulation was presented. Mathematical formulations of power system stability analysis tools, such as critical clearing time, were also presented. Power system stability has also been presented with its mathematical formulation. The next chapter will give the IEEE 39 bus system's computer modelling into DigSilent Powerfactory.

CHAPTER FOUR: IEEE 39 BUS SYSTEM COMPUTER MODELLING

4.1. Introduction

This chapter presents implementing the IEEE 39 bus system components in Digsilent powerfactory. As generators, transmission lines, transformers, loads, and shunt components are the components that makeup power systems, their parameters are given in this chapter, along with their computation for the 39-bus system. Wind generators are also computed and implemented in the systems mentioned above, along with both SM-PSHP and DFIM-PSHP used to improve the system stability.

4.2. IEEE 39 bus system

The 39 Bus New England System is a modified representation of the high-voltage transmission system in the north-eastern United States (New England) (Shadabi & Kamwa, 2022). It was initially introduced in 1970 and has since been widely utilized in scientific research and publishing (Abaci et al., 2018) and (Abaci et al., 2021). The New England 39 Bus System comprises 39 buses, ten generators, 19 loads, 34 lines, and 12 transformers (Sahami & Kamalasadnan, 2019). The network data utilized for the load flow computation is described in the subsections below (DlG SILENT GmbH, 2015a).

4.2.1. Generators

The link to the remainder of the transmission system (US and Canadian) is represented by Generator "G 01," which is directly connected at the 345 kV level. Transformers link all the generators together. The generator "G 02" represents the slack element of the network model, hence the voltage magnitude and angle are provided (0.982 p.u., 0.0 degrees) (DlG SILENT GmbH, 2015a). The parameters used in the PowerFactory model are listed in Table 4.1 (DlG SILENT GmbH, 2015a).

Table 4.1: Data of generators in the PowerFactory model ($x'' = x''^d = x''^q$)

Unit No.	Sr in MVA	H in s	Ra in p.u.	x'd in p.u.	x'q in p.u.	xd in p.u.	xq in p.u.	T'd0 in s	T'q0 in s	xl in p.u.	x'' in p.u.	T''d0 in s	T''q0 in s
1	10000	5.0	0	0.6	0.8	2.	1.9	7	0.7	0.3	0.4	0.05	0.035
2	700	4.3	0	0.5	1.2	2.1	1.97	6.6	1.5	0.2	0.4	0.05	0.035
3	800	4.5	0	0.4	0.7	2	1.9	5.7	1.5	0.2	0.4	0.05	0.035
4	800	3.6	0	0.3	1.3	2.1	2.1	5.7	1.5	0.2	0.3	0.05	0.035
5	300	4.3	0	0.4	0.5	2	1.9	5.4	0.4	0.2	0.3	0.05	0.035
6	800	4.3	0	0.4	0.7	2.	1.9	7.3	0.4	0.2	0.3	0.05	0.035
7	700	3.8	0	0.3	1.3	2.1	2.0	5.7	1.5	0.2	0.3	0.05	0.035
8	700	3.5	0	0.4	0.6	2.	1.9	6.7	0.4	0.2	0.3	0.05	0.035
9	1000	3.4	0	0.6	0.6	2.1	2.1	4.8	1.9	0.3	0.4	0.05	0.035
10	1000	4.2	0	0.3	0.5	1	0.7	10.2	0.0	0.1	0.2	0.05	0.035

Figures 4.1 and 4.2 show a computation of the generator parameters in DigSILENT PowerFactory 2015.

Synchronous Machine Type - Generator Types\ Type Gen 02.TypeSym

Basic Data	Name	Type Gen 02		OK
Load Flow	Nominal Apparent Power	700	MVA	Cancel
VDE/IEC Short-Circuit	Nominal Voltage	16.5	kV	
Complete Short-Circuit	Power Factor	0.85		
ANSI Short-Circuit	Connection	YN		
IEC 61363				
DC Short-Circuit				
RMS-Simulation				
EMT-Simulation				
Harmonics/Power Quality				
Protection				
Optimal Power Flow				
Reliability				
Generation Adequacy				
Description				

Figure 4.1 Generator G2 parameters in DigSilent

Synchronous Machine Type - Generator Types\ Type Gen 02.TypeSym

Basic Data	Synchronous Reactances		OK
Load Flow	xd	2.065 p.u.	Cancel
VDE/IEC Short-Circuit	xq	1.974 p.u.	
Complete Short-Circuit	Reactive Power Limits		
ANSI Short-Circuit	Minimum Value	-1 p.u.	
IEC 61363	Maximum Value	1 p.u.	
DC Short-Circuit	Zero Sequence Data		
RMS-Simulation	Reactance x0	0.1 p.u.	
EMT-Simulation	Resistance r0	0 p.u.	
Harmonics/Power Quality	Negative Sequence Data		
Protection	Reactance x2	0.2 p.u.	
Optimal Power Flow	Resistance r2	0 p.u.	
Reliability			
Generation Adequacy			
Description			

Figure 4.2: Generator G2 load flow parameters in DigSilent

4.2.2. Power transformers

In accordance with generator ratings, realistic ratings were produced for the PowerFactory model, and the parameters were recalculated based on these values. The PowerFactory model's transformer parameters are listed per unit in Table 4.2. (DigSILENT GmbH, 2015a.) according to Figures 4.3 and 4.4

Table 4.2: Data of transformers in the PowerFactory model

Transformer	From Bus	To Bus	Sr in MVA	Ur HV in kV	Ur LV in kV	R in p.u.	X in p.u.	Z in p.u.
Trf 12 - 11	Bus 12	Bus 11	300	345.0	138.0	0.0048	0.1305	0.1306
Trf 12 - 13	Bus 12	Bus 13	300	345.0	138.0	0.0048	0.1305	0.1306
Trf 06 - 31	Bus 06	Bus 31	700	345.0	16.5	0.0000	0.1750	0.1750
Trf 10 - 32	Bus 10	Bus 32	800	345.0	16.5	0.0000	0.1600	0.1600
Trf 19 - 33	Bus 19	Bus 33	800	345.0	16.5	0.0056	0.1136	0.1137
Trf 20 - 34	Bus 20	Bus 34	2 x 300	230.0	16.5	0.0054	0.1080	0.1081
Trf 22 - 35	Bus 22	Bus 35	800	345.0	16.5	0.0000	0.1144	0.1144
Trf 23 - 36	Bus 23	Bus 36	700	345.0	16.5	0.0035	0.1904	0.1904
Trf 25 - 37	Bus 25	Bus 37	700	345.0	16.5	0.0042	0.1624	0.1625
Trf 02 - 30	Bus 02	Bus 30	1000	345.0	16.5	0.0000	0.1810	0.1810
Trf 29 - 38	Bus 29	Bus 38	1000	345.0	16.5	0.0080	0.1560	0.1562
Trf 19 - 20	Bus 19	Bus 20	1000	345.0	230.0	0.0070	0.1380	0.1382

2-Winding Transformer Type - Transformer Types\Trf Type 06 - 31 YNy0.TypeTr2

The screenshot shows the configuration window for a transformer. The 'Basic Data' tab is selected. The 'Name' field contains 'Trf Type 06 - 31 YNy0'. The 'Technology' is set to 'Three Phase Transformer'. The 'Rated Power' is 700 MVA and the 'Nominal Frequency' is 60 Hz. The 'Rated Voltage' section shows HV-Side at 345 kV and LV-Side at 16.5 kV. The 'Vector Group' is set to YN on the HV side and Y on the LV side. The 'Phase Shift' is 0.0 degrees. The 'Name' field at the bottom is 'YNy0'. There are also sections for Positive and Zero Sequence Impedance with fields for Short-Circuit Voltage and SHC-Voltage.

Figure 4.3: Transformer parameters in DigSilent

2-Winding Transformer Type - Transformer Types\Trf Type 06 - 31 YNy0.TypeTr2

The screenshot shows the 'Load Flow' tab of the transformer configuration window. It includes sections for 'Magnetizing Impedance' (No Load Current: 0.0%, No Load Losses: 0.0 kW) and 'Zero Sequence Magnetizing Impedance' (Mag. Impedance/uk0: 100.0, Mag. R/X: 0.0). There are also sections for 'Distribution of Leakage Reactances (p.u.)' and 'Distribution of Leakage Resistances (p.u.)', both with HV and LV side values set to 0.5.

Figure 4.4: Transformer load flow parameters

4.2.3. Transmission lines

Table 4.3 displays line data per unit (p.u.) based on 100 MVA, but provides no information on line length. The PowerFactory model needs input data in the units of Ω/km and $\mu\text{F}/\text{km}$, respectively. Recalculated line data for a network model with nominal voltage of 345 kV and nominal frequency of 60 Hz is also shown. Because no line length is provided, the length of each line in the PowerFactory model was computed using the assumption that the reactance per length is $0.3 \Omega/\text{km}$ (DigSILENT GmbH, 2015a). Table 4.3 shows the line data utilized in the PowerFactory model.

Table 4.3: Data of lines in the PowerFactory model (345 kV, 60 Hz)

Line	From Bus	To Bus	Length in km	R' in Ω/km	X' in Ω/km	C' in $\mu\text{F}/\text{km}$
Line 01 - 02	Bus 01	Bus 02	163.06425	0.02554745	0.300	0.0095491
Line 01 - 39	Bus 01	Bus 39	99.18750	0.01200000	0.300	0.0168514
Line 02 - 03	Bus 02	Bus 03	59.90925	0.02582781	0.300	0.0095677
Line 02 - 25	Bus 02	Bus 25	34.12050	0.24418605	0.300	0.0095360
Line 03 - 04	Bus 03	Bus 04	84.50775	0.01830986	0.300	0.0058386
Line 03 - 18	Bus 03	Bus 18	52.76775	0.02481203	0.300	0.0090296
Line 04 - 05	Bus 04	Bus 05	50.78400	0.01875000	0.300	0.0058892
Line 04 - 14	Bus 04	Bus 14	51.18075	0.01860465	0.300	0.0060177
Line 05 - 06	Bus 05	Bus 06	10.31550	0.02307692	0.300	0.0093763
Line 05 - 08	Bus 05	Bus 08	44.43600	0.02142857	0.300	0.0074026
Line 06 - 07	Bus 06	Bus 07	36.50100	0.01956522	0.300	0.0068993
Line 06 - 11	Bus 06	Bus 11	32.53350	0.02560976	0.300	0.0095149
Line 07 - 08	Bus 07	Bus 08	18.25050	0.02608696	0.300	0.0095247
Line 08 - 09	Bus 08	Bus 09	144.02025	0.01900826	0.300	0.0058864
Line 09 - 39	Bus 09	Bus 39	99.18750	0.01200000	0.300	0.0269622
Line 10 - 11	Bus 10	Bus 11	17.06025	0.02790698	0.300	0.0095230
Line 10 - 13	Bus 10	Bus 13	17.06025	0.02790698	0.300	0.0095230
Line 13 - 14	Bus 13	Bus 14	40.07175	0.02673267	0.300	0.0095825
Line 14 - 15	Bus 14	Bus 15	86.09475	0.02488479	0.300	0.0094740
Line 15 - 16	Bus 15	Bus 16	37.29450	0.02872340	0.300	0.0102184
Line 16 - 17	Bus 16	Bus 17	35.31075	0.02359551	0.300	0.0084699
Line 16 - 19	Bus 16	Bus 19	77.36625	0.02461538	0.300	0.0087569
Line 16 - 21	Bus 16	Bus 21	53.56125	0.01777778	0.300	0.0106018
Line 16 - 24	Bus 16	Bus 24	23.40825	0.01525424	0.300	0.0064740
Line 17 - 18	Bus 17	Bus 18	32.53350	0.02560976	0.300	0.0090353
Line 17 - 27	Bus 17	Bus 27	68.63775	0.02254335	0.300	0.0104420
Line 21 - 22	Bus 21	Bus 22	55.54500	0.01714286	0.300	0.0102914
Line 22 - 23	Bus 22	Bus 23	38.08800	0.01875000	0.300	0.0108013
Line 23 - 24	Bus 23	Bus 24	138.86250	0.01885714	0.300	0.0057937
Line 25 - 26	Bus 25	Bus 26	128.15025	0.02972136	0.300	0.0089213
Line 26 - 27	Bus 26	Bus 27	58.32225	0.02857143	0.300	0.0091555
Line 26 - 28	Bus 26	Bus 28	188.05950	0.02721519	0.300	0.0092457
Line 26 - 29	Bus 26	Bus 29	247.96875	0.02736000	0.300	0.0092480
Line 28 - 29	Bus 28	Bus 29	59.90925	0.02781457	0.300	0.0092627

Figures 4.5 and 4.6 show a configuration of the line parameters in Digsilent PowerFactory 2015.

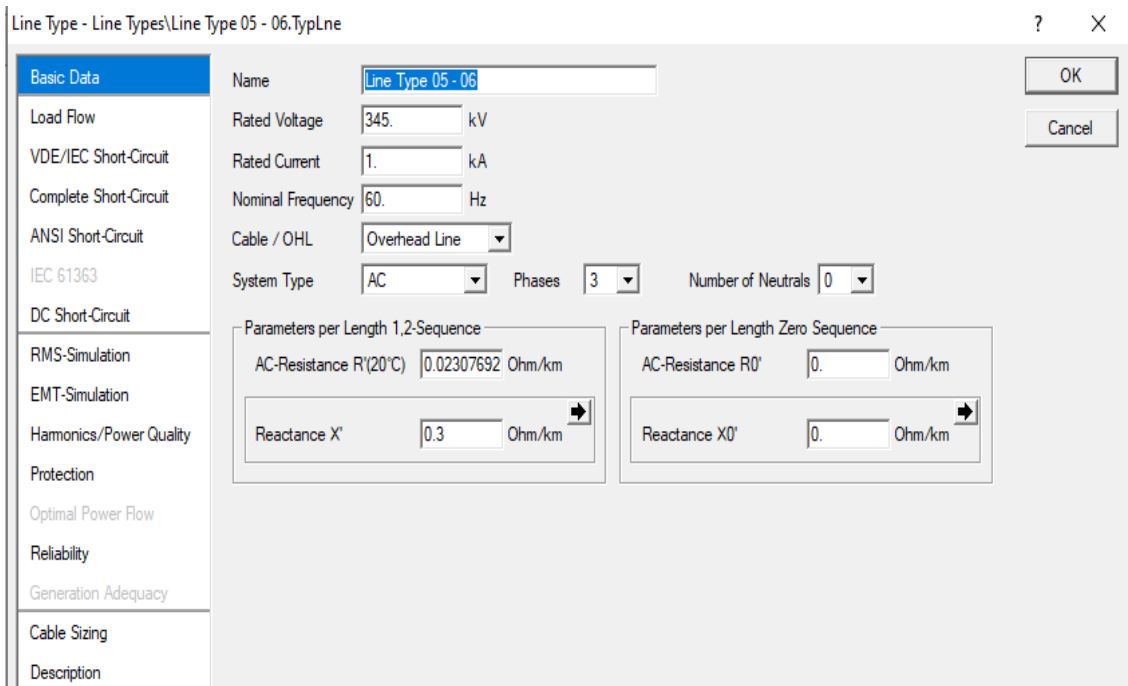


Figure 4.5: Line parameters

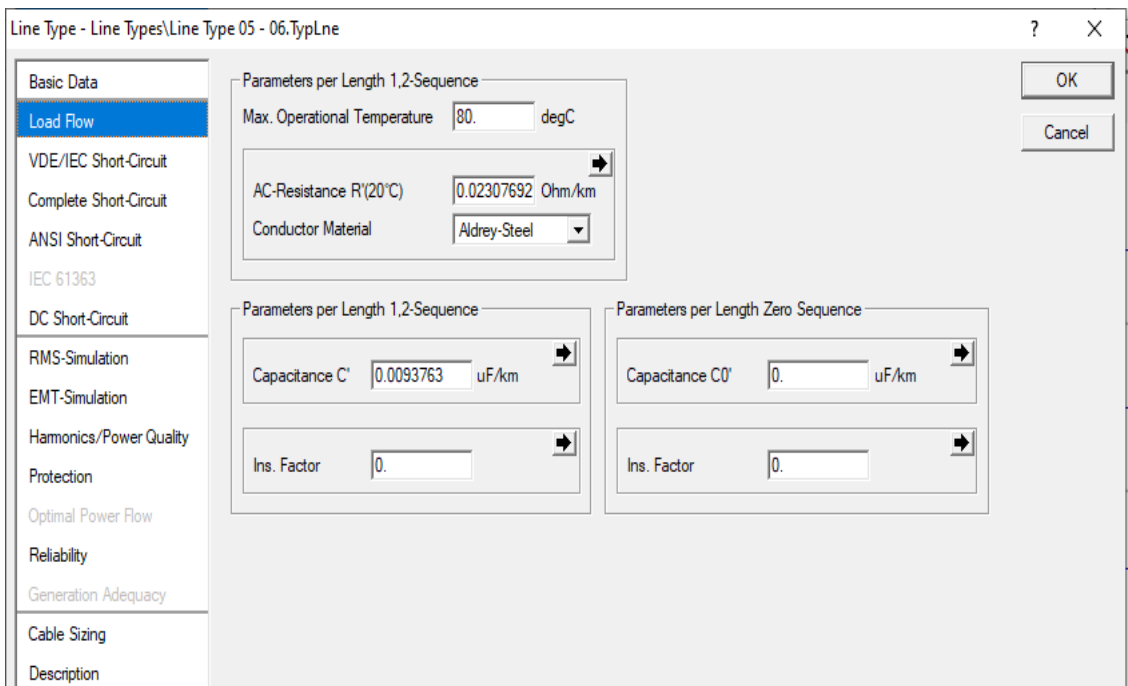


Figure 4.6: Line load flow parameters

4.2.4. Loads

The loads are not voltage-dependent, and their active and reactive power demands are constant. This is accomplished using the PowerFactory load flow calculation command to disable the load option "Consider Voltage Dependency of Loads." Table 4.4 lists the load data (active power P and reactive power Q) obtained from (DIgSILENT GmbH, 2015a).

Table 4.4: Load profil

Load	Bus	P in MW	Q in Mvar
Load 3	Bus 3	322.0	2.4
Load 4	Bus 4	500.0	184.0
Load 7	Bus 7	233.8	84.0
Load 8	Bus 08	522.0	176.0
Load 12	Bus 12	7.5	88.0
Load 15	Bus 15	320.0	153.0
Load 16	Bus 16	329.0	32.3
Load 18	Bus 18	158.0	30.0
Load 20	Bus 20	628.0	103.0
Load 21	Bus 21	274.0	115.0
Load 23	Bus 23	247.5	84.6
Load 24	Bus 24	308.6	-92.2
Load 25	Bus 25	224.0	47.2
Load 26	Bus 26	139.0	17.0
Load 27	Bus 27	281.0	75.5
Load 28	Bus 28	206.0	27.6
Load 29	Bus 29	283.5	26.9
Load 31	Bus 31	9.2	4.6
Load 39	Bus 39	1104.0	250.

Those parameters according to tables 2.40 and 2.41 are computed as shown in Figures 4.7 and 4.8.

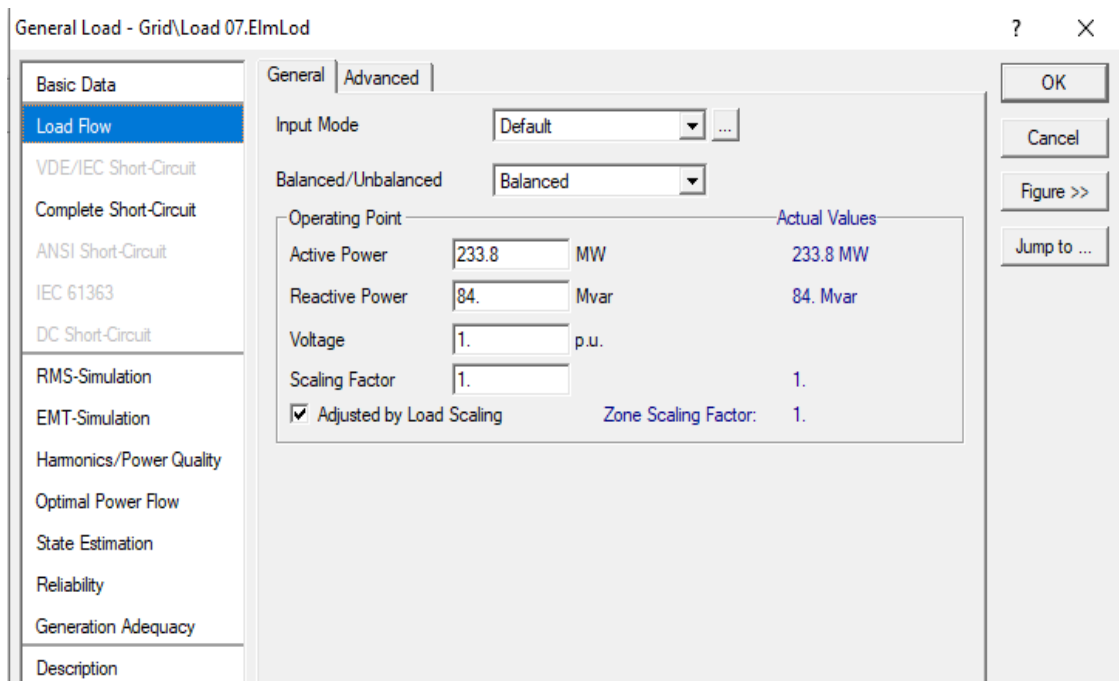


Figure 4.7: General load computed

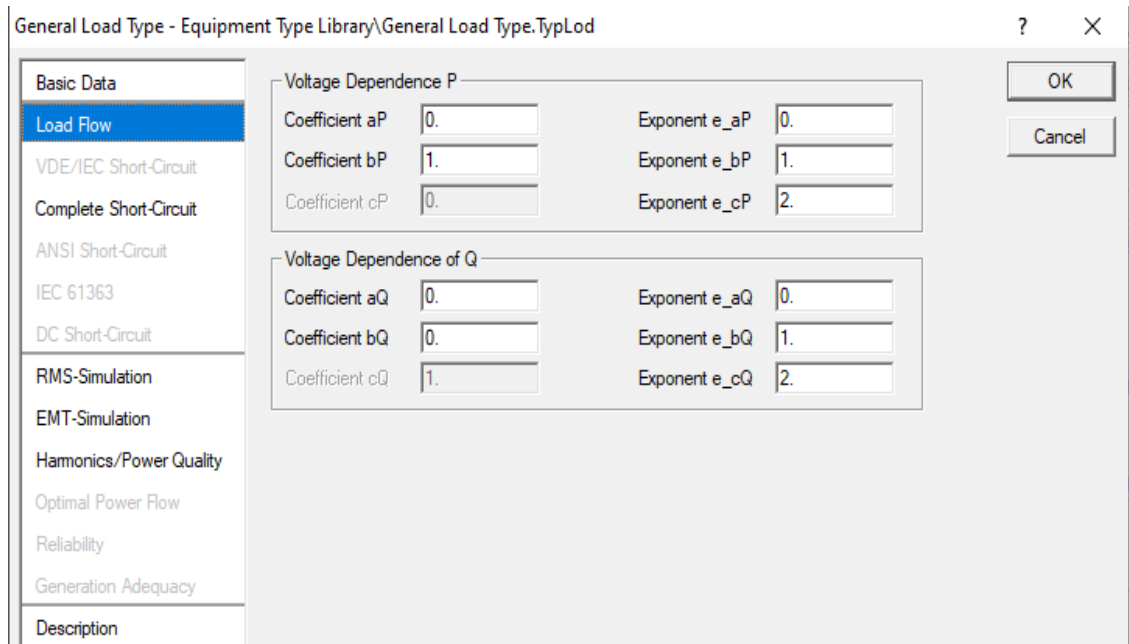


Figure 4.8: General load voltage dependence computed

4.3. DFIG Wind Turbines

Wind energy is modelled with doubly-fed induction generators in this work as wind energy. The following sessions will describe the controllers of the DFIG and how it is computed.

4.3.1. DFIG Controllers

4.3.1.1. Composite frame of the DFIG

The frame of the DFIG model in PowerFactory is shown in Figure 4.9. The prime mover model is shown in blue, the converter controllers are in the middle, and the DFIG is in green. On the left side of the frame are the other controllers and measurements. The controllers will be described in the following sections.

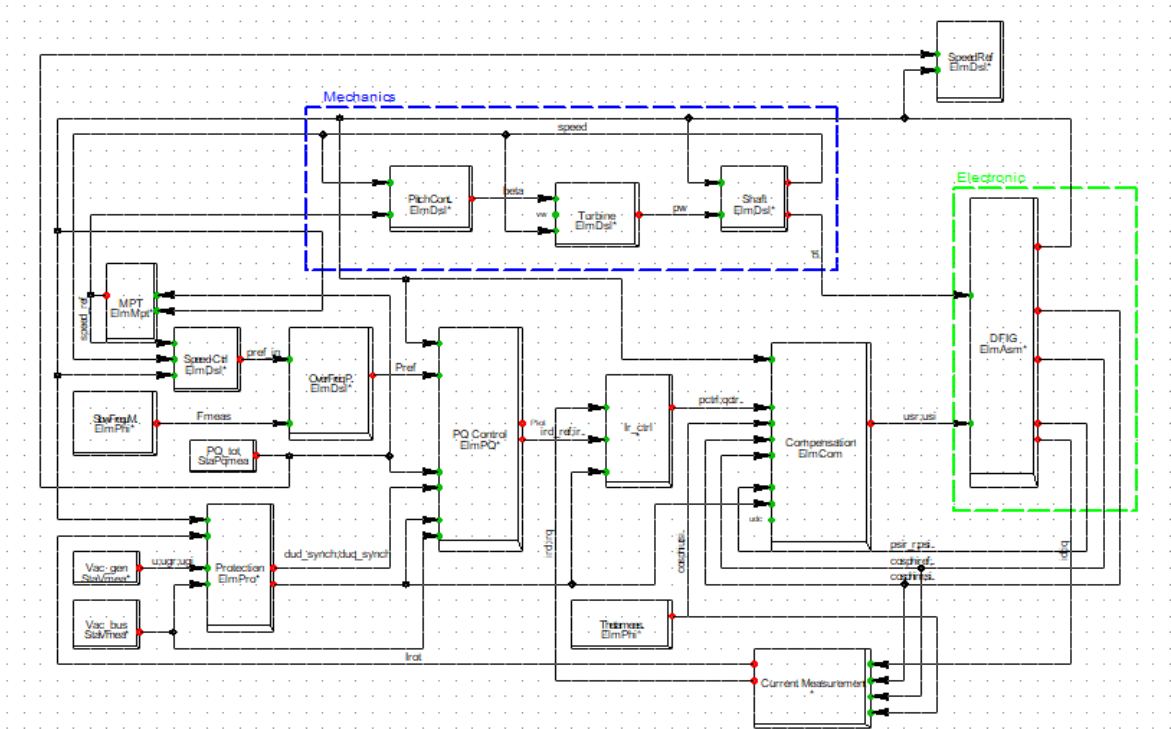


Figure 4.9: DFIG composite frame

4.3.1.2. Gen PQ-Controller

It is the rotor-side converter's active and reactive power management. It calculates the reference rotor current's dq-components. It is shown in Figure 4.10.

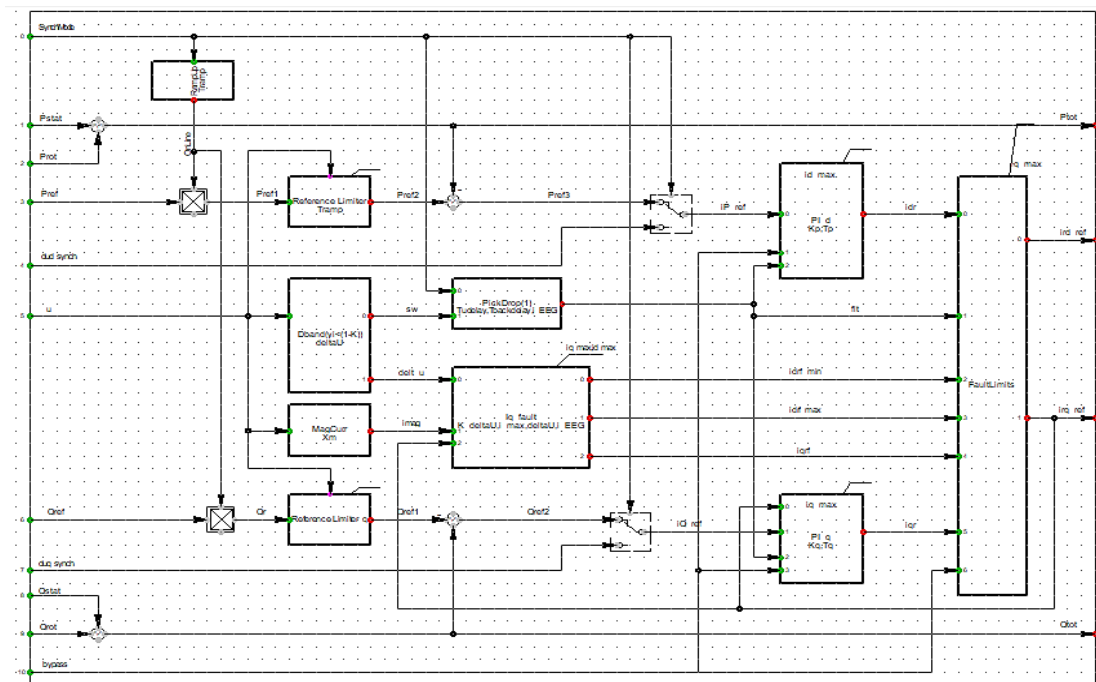


Figure 4.10: PQ Control with synch

4.3.1.3. Rotor current controller (Irot ctrl)

Irot ctrl is the rotor current controller that compares the GenPQ-dq-components controller of the reference rotor current to the actual dq-components of the rotor current. Its outputs are the delta multiplied by a gain and the PT1 term. Its block definition is shown in Figure 4.11.

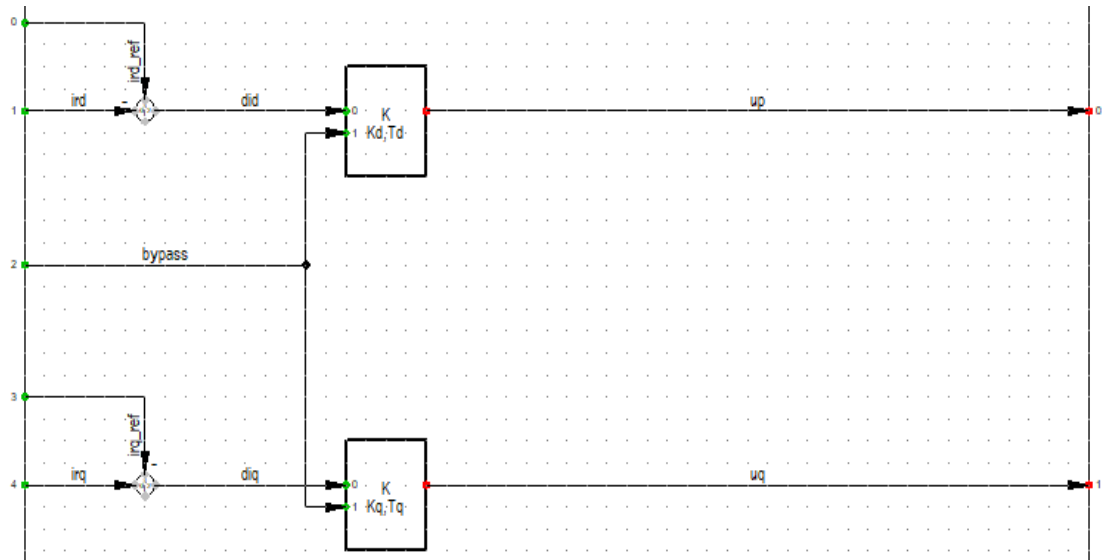


Figure 4.11: Irot_Ctrl block definition

4.3.1.4. Pitch Control

The pitch control is a PI controller that works as a function of the wind turbine's rotational speed. The pitch control only kicks in above the normal rotational speed or when the power cap in the maximum power point tracking (MPPT) model is reached. The variable speed follows the maximum power point tracking characteristics below the nominal rotational speed. Its block definition is seen in Figure 4.12.

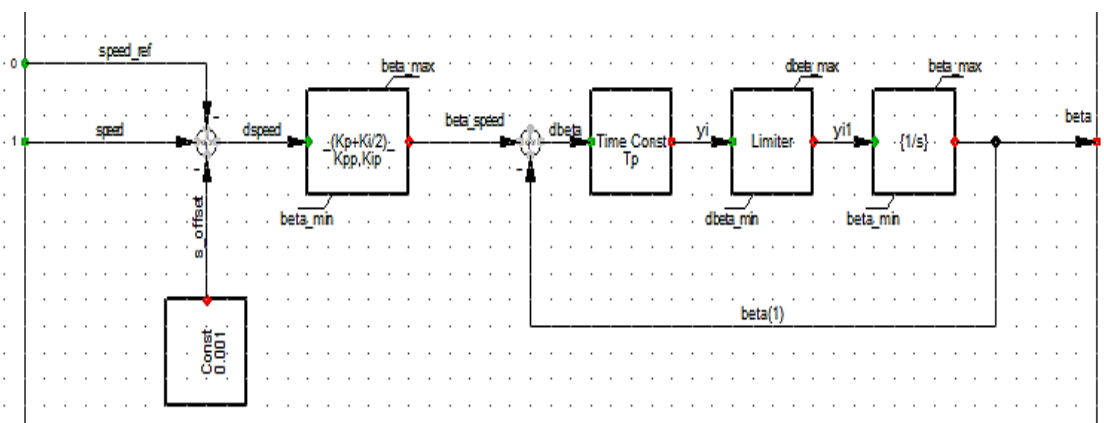


Figure 4.12: Pitch-Ctrl block definition

4.3.1.5. MPPT Control

The maximum power point tracking control provides the active power reference as a function of the rotating generator speed. Because efficiency is a function of tip-speed ratio and pitch angle, this measures the maximum efficiency for continually changing

wind speeds. The rotor converter size determines the minimum and maximum generator speeds. The converter size is 30% of the generator's apparent power in the implemented model. Figure 4.13 shows its common model.

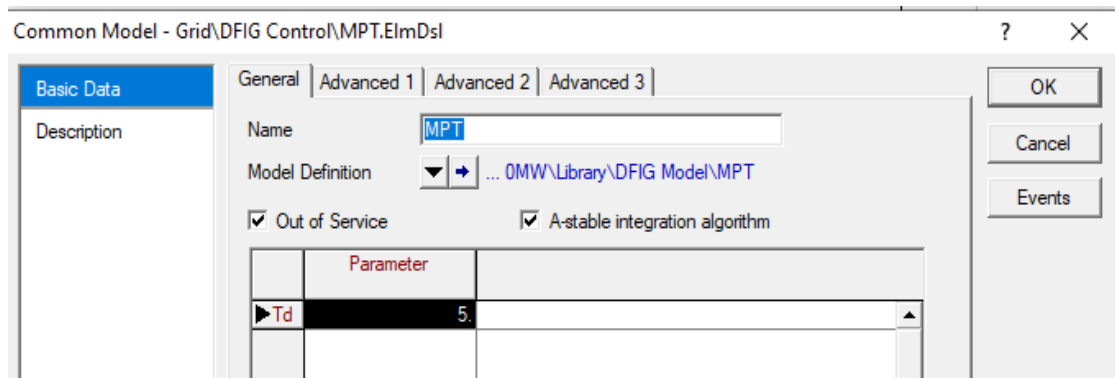


Figure 4.13: MPPT Common model

4.3.1.6. Protection

The wind turbine is safeguarded in three distinct ways. As soon as the overspeed/underspeed and overvoltage/undervoltage safeguards are triggered, the machine breaker is engaged and the turbine is shut off. The rotor current protection inserts the crowbar to prevent the rotor converter from being overloaded and ensures that the machine will continue to function despite the issue. For the speed and voltage safeguards, there are two trigger systems: one for more severe and one for less severe violations. Its block definition is shown in Figure 4.14.

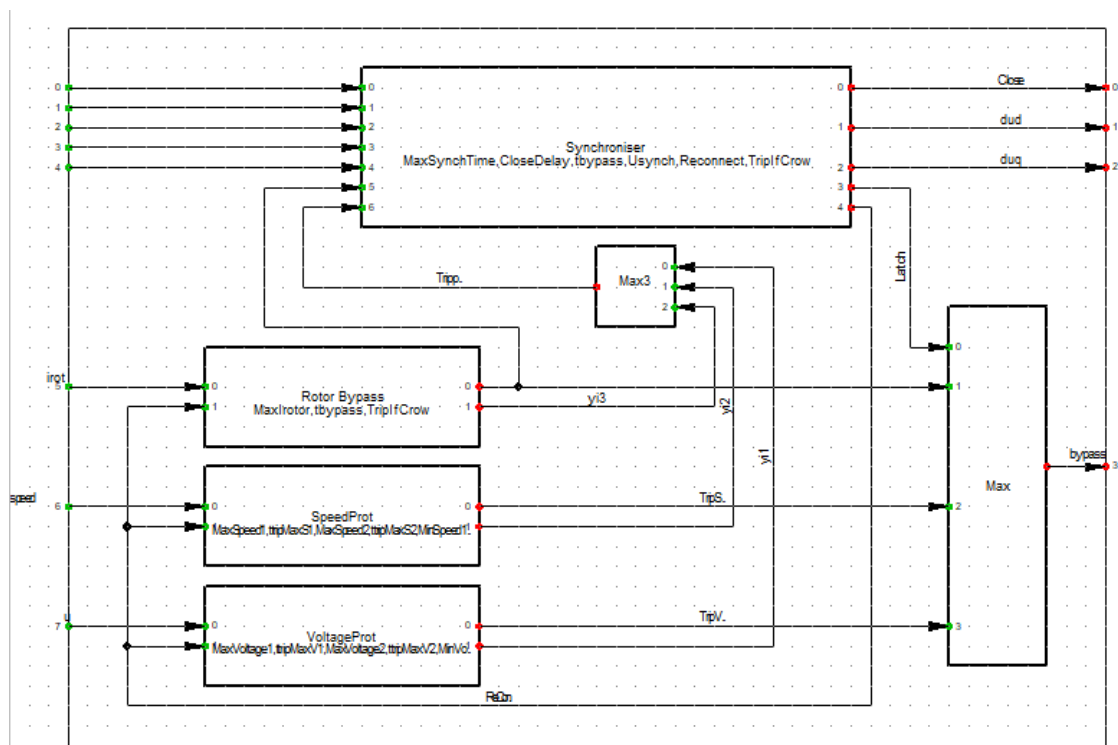


Figure 4.14: Protection block definition

If the voltage falls below 0.2 pu for more than 1 second or below 0.4 pu for more than 2 seconds, the undervoltage protection will trigger and unplug the machine. These values are seen in Figure 4.15, representing the protection common model in Powerfactory.

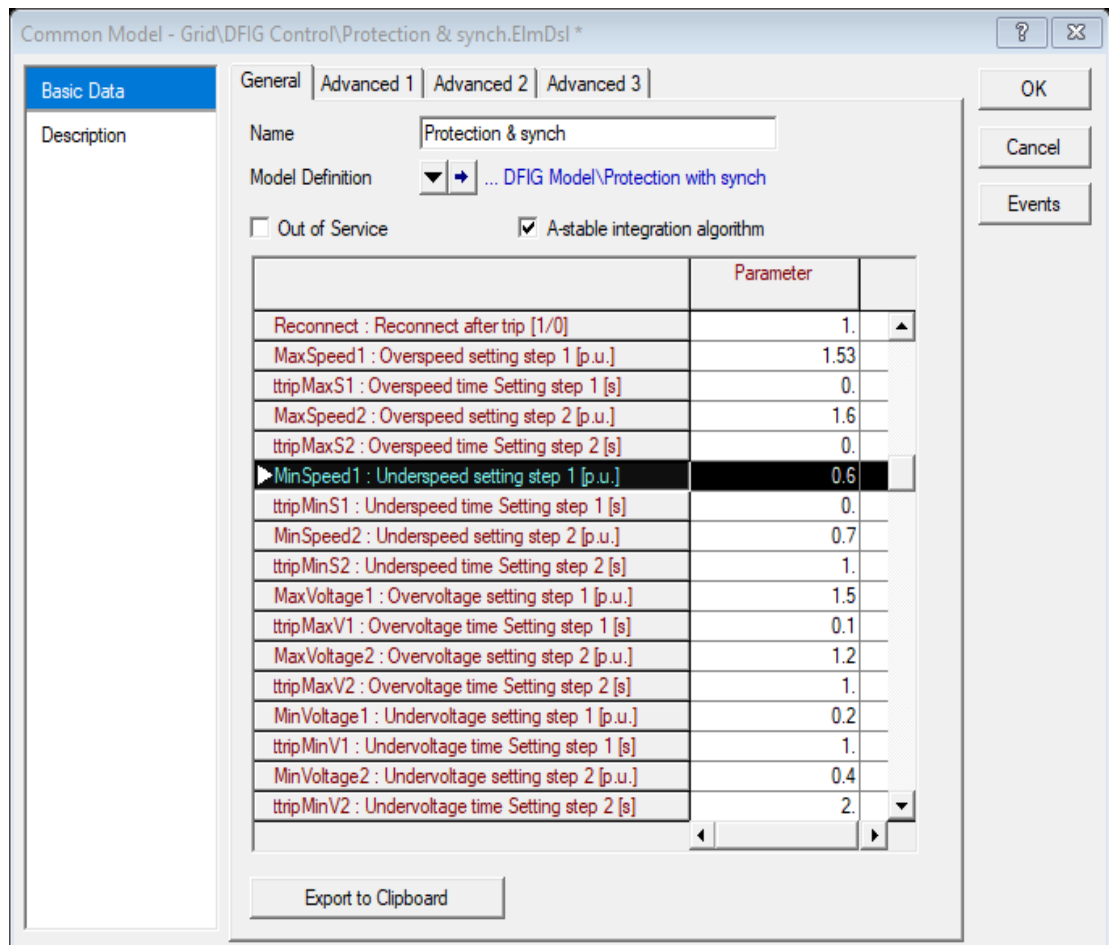


Figure 4.15: Protection common model

4.3.1.7. Rotor current measurement

The dq-components of the rotor current are transformed from rotor-referenced to stator-referenced coordinates. The resultant dq-rotor currents are utilized as current measurements of rotor current in rotor current control. Also estimated and utilized in the protection model is the absolute rotor current (in kA). Figure 4.16 shows its common model.

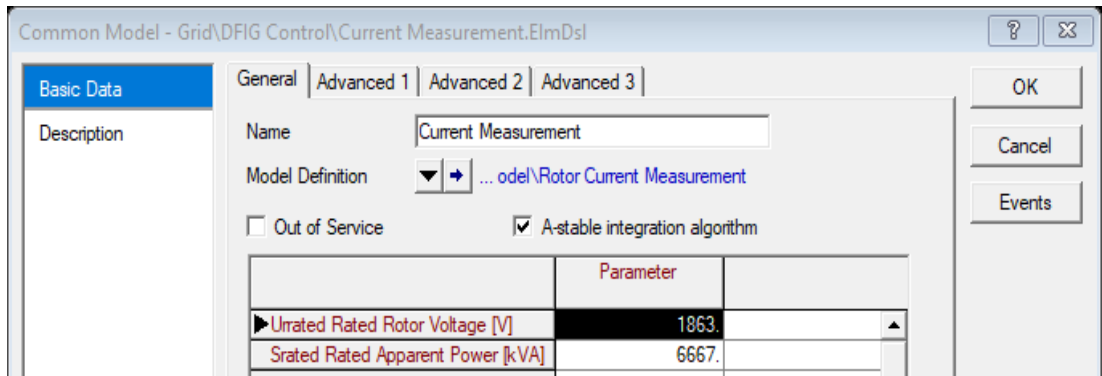


Figure 4.16: Current measurement common model

4.3.1.8. Shaft

The shaft is represented as a two-mass model to correctly depict oscillations caused by rapid changes in mechanical or electrical force. For example, wind gusts or grid faults might create unexpected torque variations. Its block definition is shown in Figure 4.17.

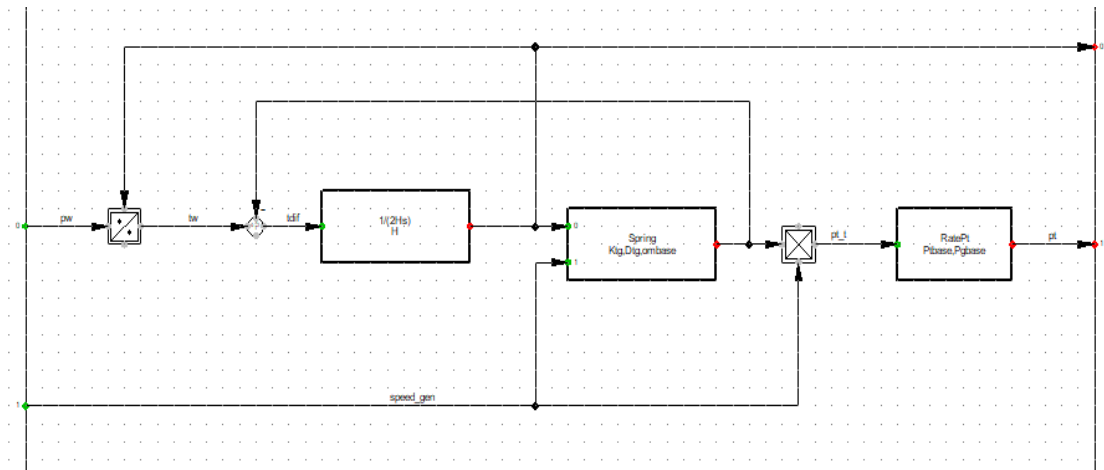


Figure 4.17: Shaft block definition

All these common models can be seen in Figure 4.18, representing the composite model of the DFIG.

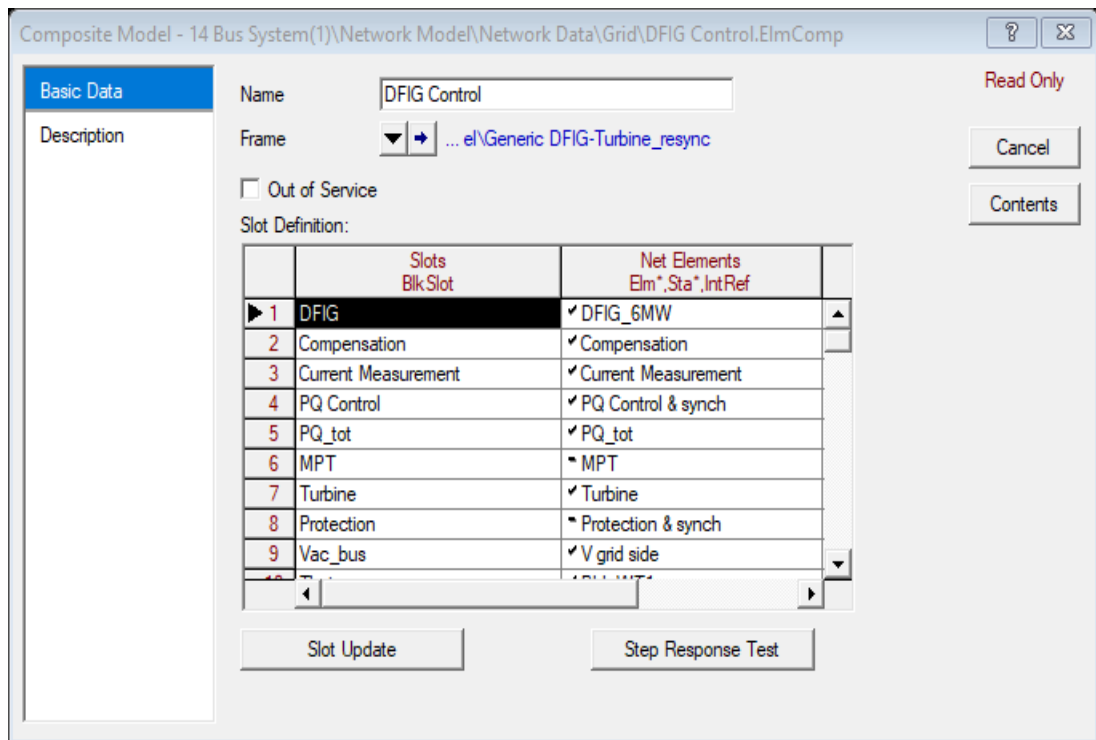


Figure 4.18: DFIG Composite model

4.3.2. DFIG computation

The wind farms used in this work are 13 parallel DFIG wind turbines with 6 MW capacity each, as seen in Figure 4.19.

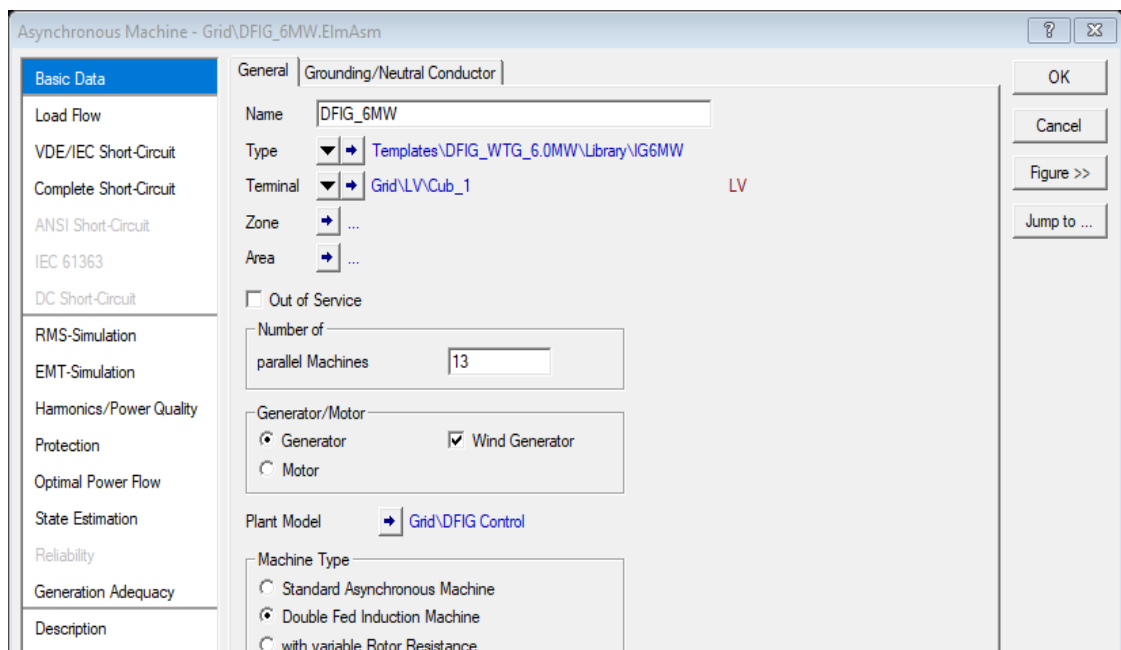


Figure 4.19: DFIG basic data

4.4. Pumped Storage Hydropower

This section provides an overview of how to create a PSHP model in DlgSILENT. Some slots (DFIG) are chosen from the library, while others are built as common models and connected to the appropriate model description.

4.4.1. Variable-Speed PSHP Model

4.4.1.1. Composite frame of the DFIG

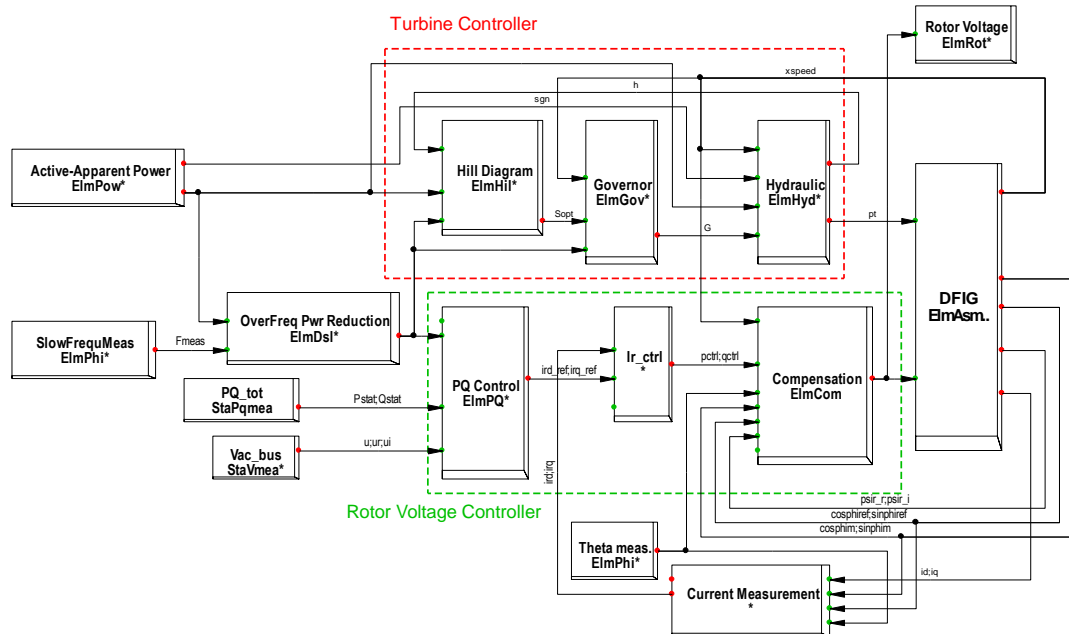


Figure 4.20: Composite frame for VS-PSHP system

Figure 4.20 illustrates the hydro pump-turbine (HPT) and DFIM/MSCom model, which was created as a composite model and includes the following elements: 1-DFIG (ElmAsm): DFIG and MSCom's basic PowerFactory model; 2-current measurement: voltage-oriented reference transformation of the stator; 3-Ir_ctrl: current controller; 4-Vac_gen (StaVmea): voltage measurement of the stator; 5-Vac_bus (StaVmea): bus voltage measurement; 6-PQ_tot (StaPqmea): measurement of the machine's total active and reactive power; 7-PQ control (ElmPQ): machine side converter (MSCom) active and reactive controller; 8-Theat_meas (ElmPhi): angle measurement; 9-hill diagram (ElmHil): determination of reference speed; 10-Over Freq Pwr Reduction: avoiding over frequency; 11-Slow Freq Meaa (ElmPhi): frequency measurement; 12-Rotor Voltage (ElmRot); 13-Hydraulic (ElmHyd); 14-Compensation (ElmCom); 15-protection (ElmPro): crow bar protection, and 16-SlowFrequMeas (ElmPhi). The following are the variables in Figure 4.20: Pt is the HPT power in per unit. usr and usi are the real and imaginary portions of the rotor voltage in p.u., xspeed is the rated rotor speed in p.u., pgn is the nominal power of the HT in kW, sgn is the apparent power of the DFIM in kVA, and pgn is the nominal power of the HPT in kW. Psir_r, psir_i are real and

imaginary parts of rotor flux in p.u., i_{dr} , i_{qr} are d-q axis rotor current in p.u., $\sin\phi_{im}$, $\cos\phi_{im}$ are sin and cos of rotor angle, $\sin\phi_{pi}$, $\cos\phi_{pi}$ are sin and cos of power angle.

4.4.1.2. Active power reduction controller

It is the rotor-side converter's active power management. It calculates the reference rotor current's dq-components. It is shown in Figure 4.21

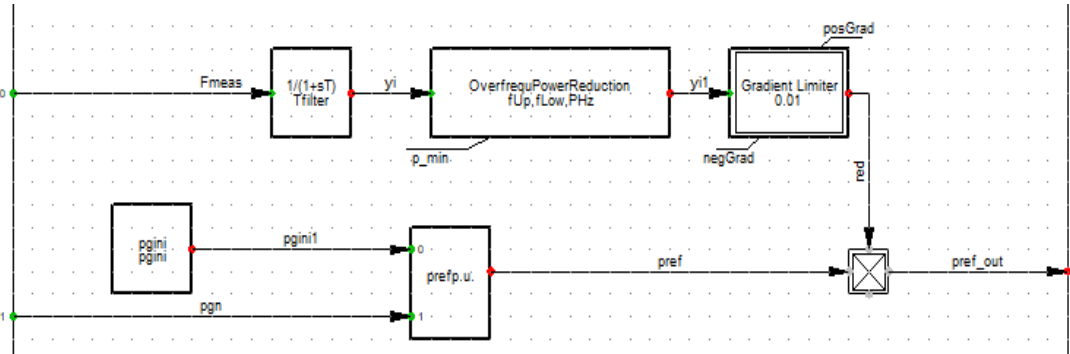


Figure 4.21: Active power reduction controller

4.4.1.3. Rotor current controller (Irot ctrl)

Irot ctrl is the rotor current controller that compares the reference rotor current's GenPQ-dq-components controllers to the actual rotor current's dq-components. Additionally, its outputs consist of the delta multiplied by a gain and the PT1 term. Its block definition is shown in Figure 4.22.

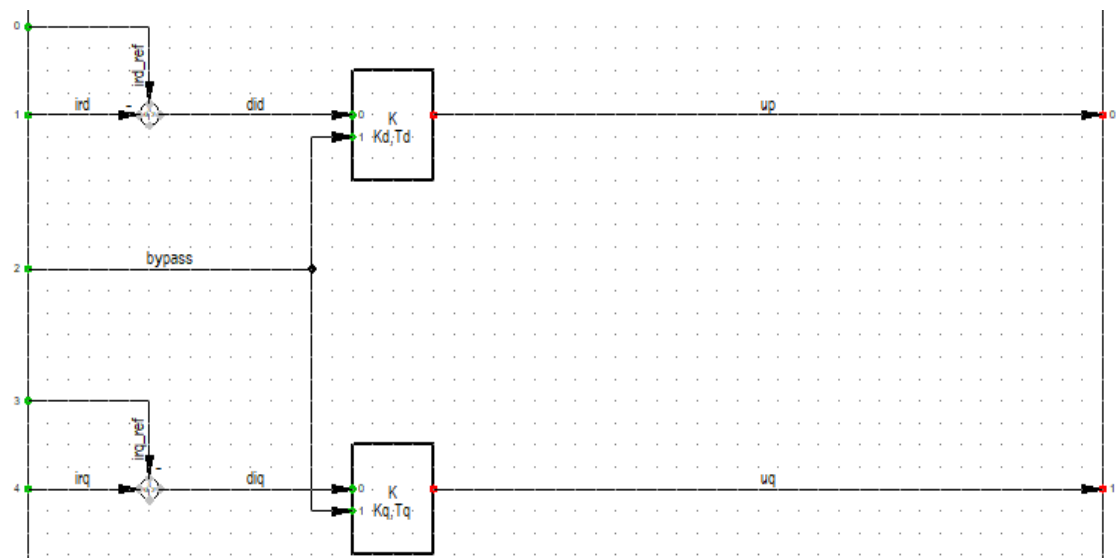


Figure 4.22: Irot_Ctrl block definition

4.4.1.4. Governor

The objective of the governor is to manage the unit's speed under all load conditions imposed on the engine-driven generator. Its block definition is seen in figure 4.23.

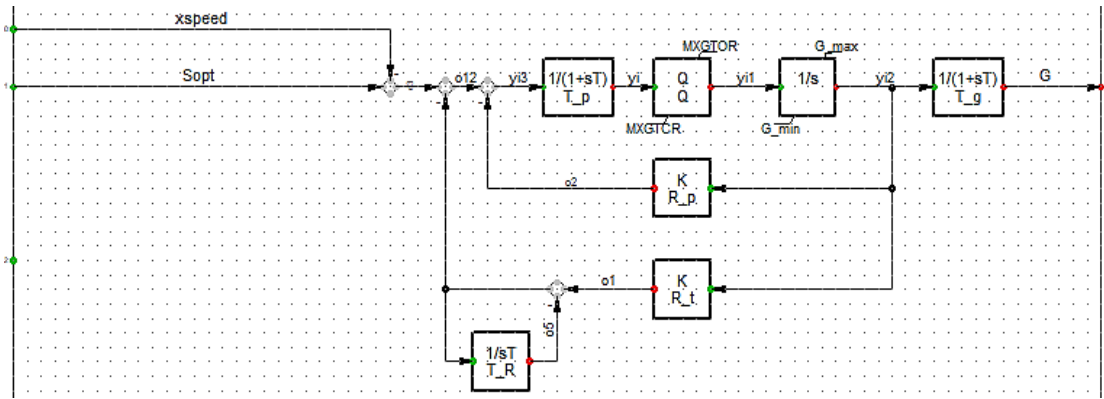


Figure 4.23: Governor block definition

4.4.1.5. Hydraulic

The most important hydraulics functions on a wind turbine are pitch adjustment, yaw and rotor braking, cooling and lubrication, and power transfer. It is important to regulate the spinning of blades that weigh tons in wind turbines. The turbine will be harmed by the blades rotating too quickly in strong winds. Hydraulics are commonly used in large equipment due to the enormous power of liquid fuel in hydraulics. Figure 4.24 shows its common model.

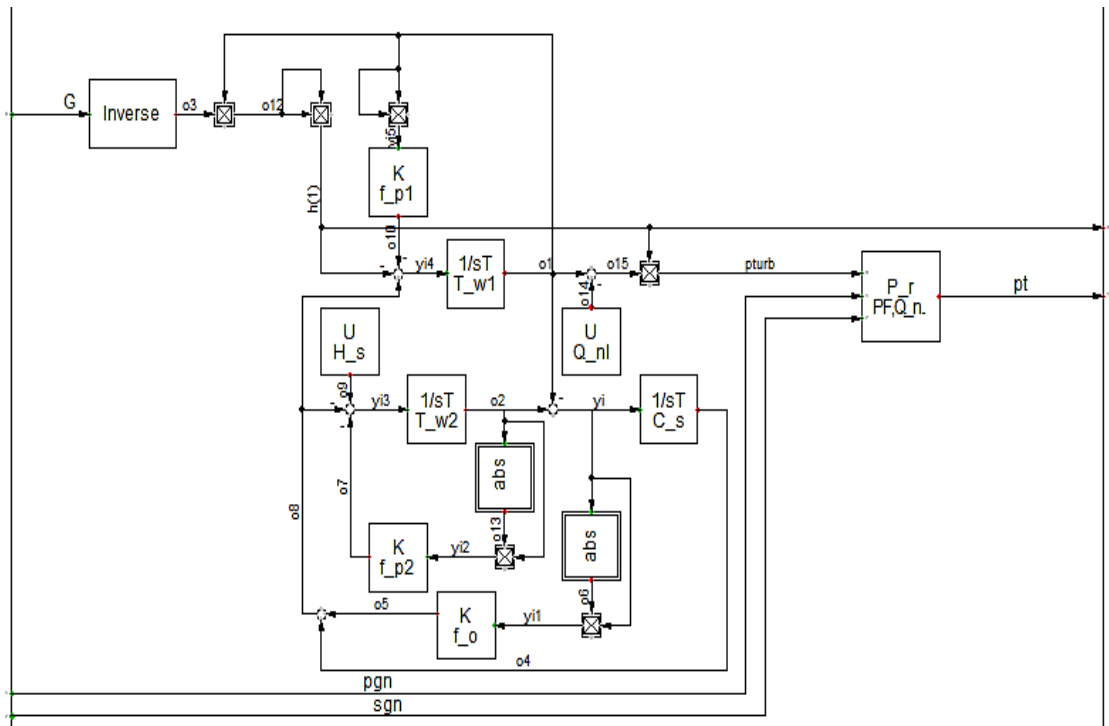


Figure 4.24: Hydraulic Common model

4.4.1.6. Protection

The wind turbine is safeguarded in three distinct ways. When the overspeed/underspeed and overvoltage/undervoltage safeguards are first triggered, the machine breaker is engaged and the turbine is halted. The rotor current protection inserts the crowbar to prevent the rotor converter from being overloaded and ensures

that the machine will continue to function despite the issue. For the speed and voltage safeguards, there are two trigger systems: one for more severe and one for less severe violations. Its block definition is shown in Figure 4.25.

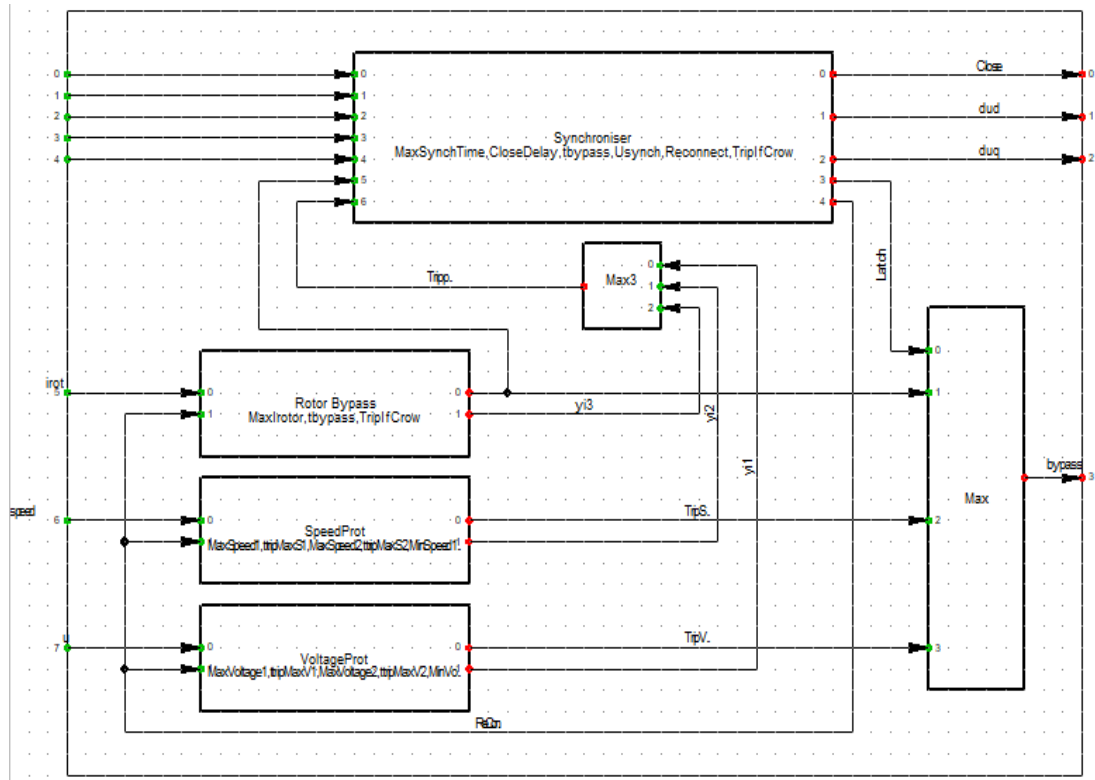


Figure 4.25: Protection block definition

4.4.1.7. PQ Control

It is the management of active and reactive power by the rotor-side converter. It estimates the dq-components of the reference rotor current. It is shown in Figure 4.26.

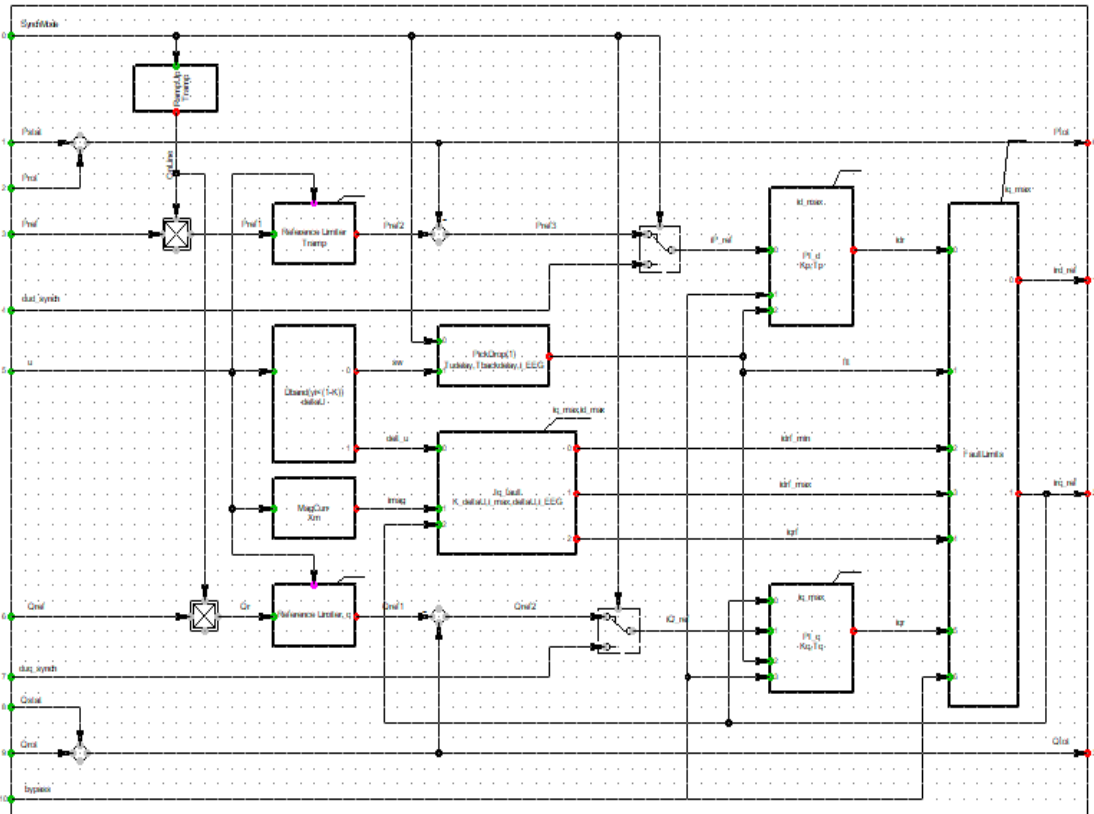


Figure 4.26: PQ Control block definition

All these common models is shown in Figure 4.27 which represents the composite model of the DFIM-PSHP based.

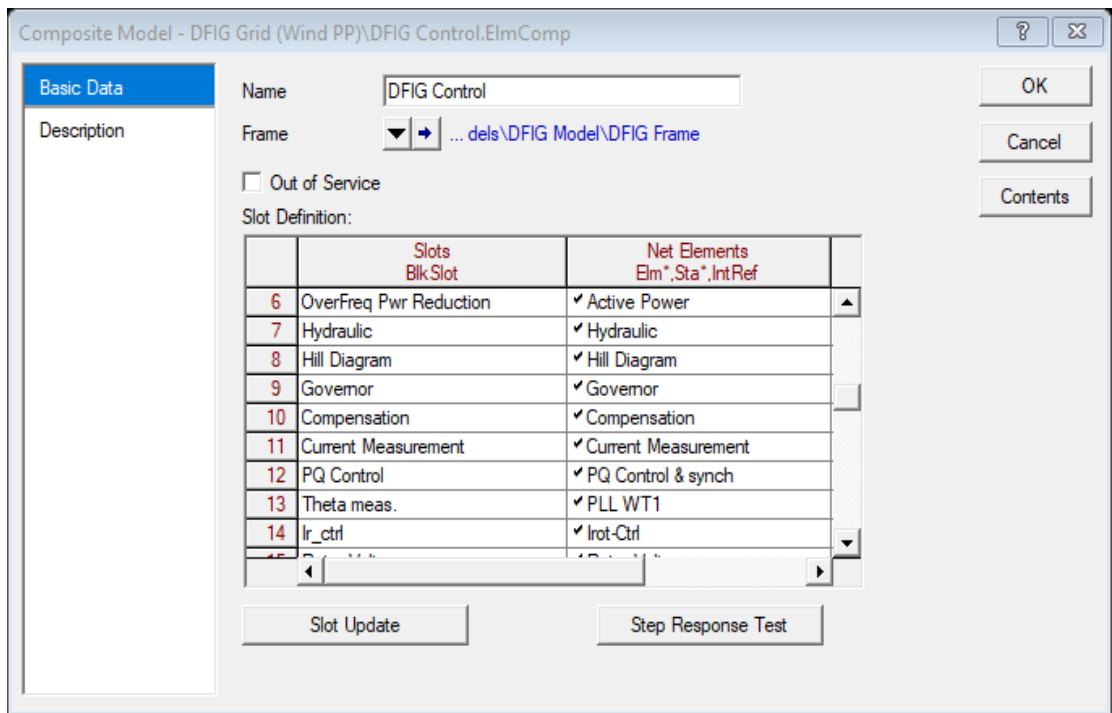


Figure 4.27: DFIM-PSHP Composite model

4.4.2. Fixed-Speed PSHP Model

4.4.2.1. Composite frame of the DFIG

Figure 4.28 illustrates the FS-PSHP composite model. Note that, except for the hill diagram, there is already a built-in model for the synchronous generator, hydro governor, and other parts (Powerfactory, 2015), so no new specification is required.

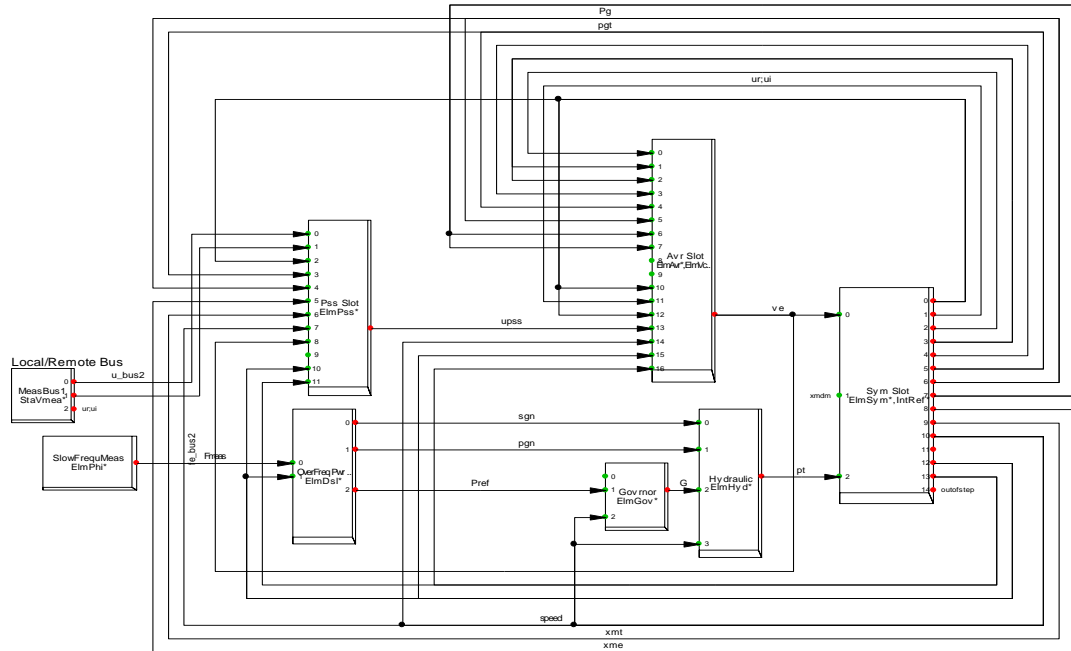


Figure 4.28: Composite frame for FS-PSHP system

Figure 4.28 illustrates the HPT and SM model, which was created as a composite model and includes the following elements: 1-SM (ElmSym): SM's basic PowerFactory model; 2-current measurement: voltage-oriented reference transformation of the stator; 34-Vac_gen (StaVmea): voltage measurement of the stator; 4-MeasBus1 (StaVmea): bus voltage measurement; 5-hill diagram (ElmHil): determination of reference speed; 10-Over Freq Pwr Reduction: avoiding over frequency; 6-Slow Freq Meaa (ElmPhi): frequency measurement; 7-Power system stabilizer; 8-Hydraulic (ElmHyd);, and 9-SlowFrequMeas (ElmPhi). The following are the variables in Figure 4.28: Pt is the HT power in per unit. usr and usi are the real and imaginary portions of the rotor voltage in p.u., xspeed is the rated rotor speed in p.u., pgn is the nominal power of the HT in kW, sgn is the apparent power of the DFIM in kVA, and pgn is the nominal power of the HPT in kW. Psir_r, psir_i are real and imaginary parts of rotor flux in p.u., i_{dr} , i_{qr} are d-q axis rotor current in p.u., sinphim, cosphim are sin and cos of rotor angle, sinphi, cosphi are sin and cos of power angle.

4.4.2.2. Active power reduction controller

It is the rotor-side converter's active power management. It calculates the reference rotor current's dq-components. It is shown in Figure 4.29.

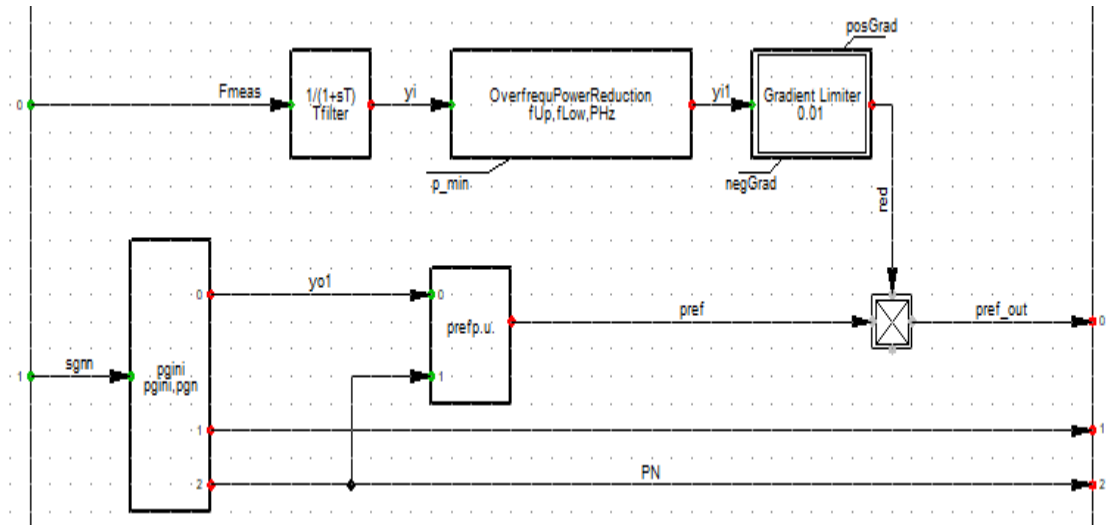


Figure 4.29: Active power reduction controller

4.4.2.3. Governor

The objective of the governor is to manage the unit's speed under all load conditions imposed on the engine-driven generator. Its block definition is seen in figure 4.30.

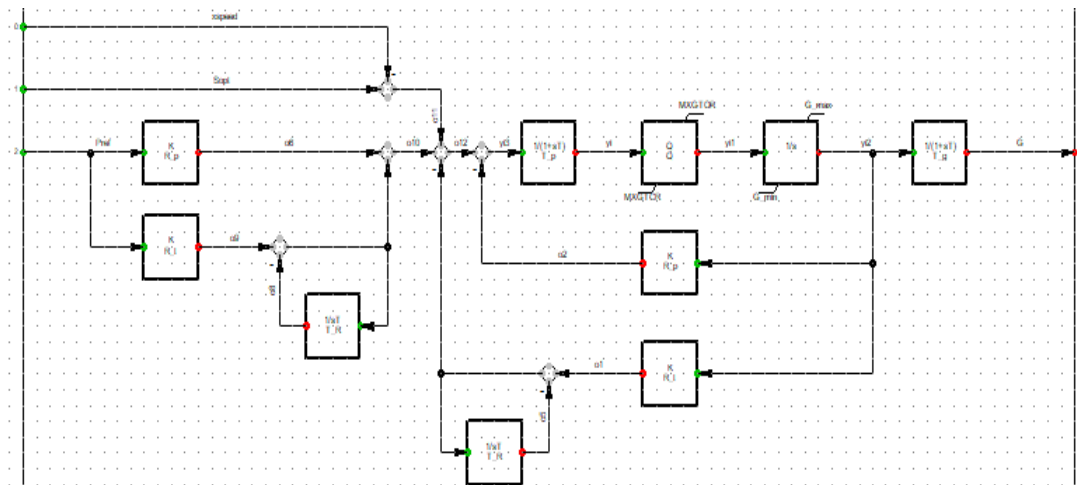


Figure 4.30: Governor block definition

4.4.2.4. Hydraulic

Hydraulic systems use a pressurised fluid to operate and carry out their functions. Another way to explain this is that the pressurised fluid ensures smooth operation. Hydraulics are commonly used in large equipment because to the enormous power of liquid fuel in hydraulics. Figure 4.31 shows its common model.

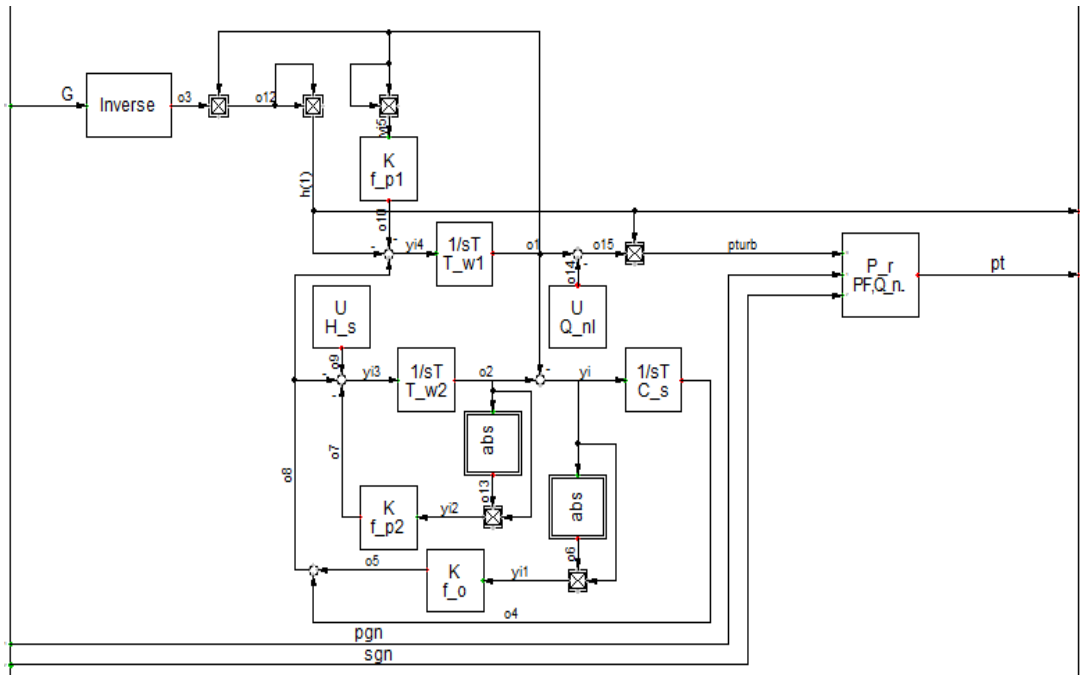


Figure 4.31: MPT Common model

4.4.2.5. AVR

A solid-state electrical device, an automated voltage regulator (AVR) adjusts the voltage at the generator output terminals. This work makes use of the IEEE type 1 AVR from the DIGSILENT library. Its block definition is shown in Figure 4.32.

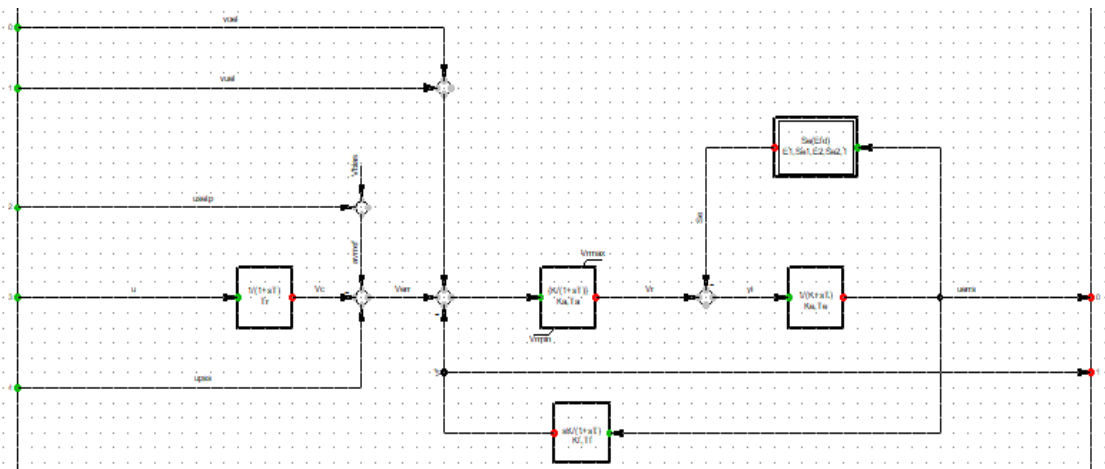


Figure 4.32: AVR block definition.

All these common models is represented in Figure 4.33 that represents the composite model of the DFIM-PSHP based.

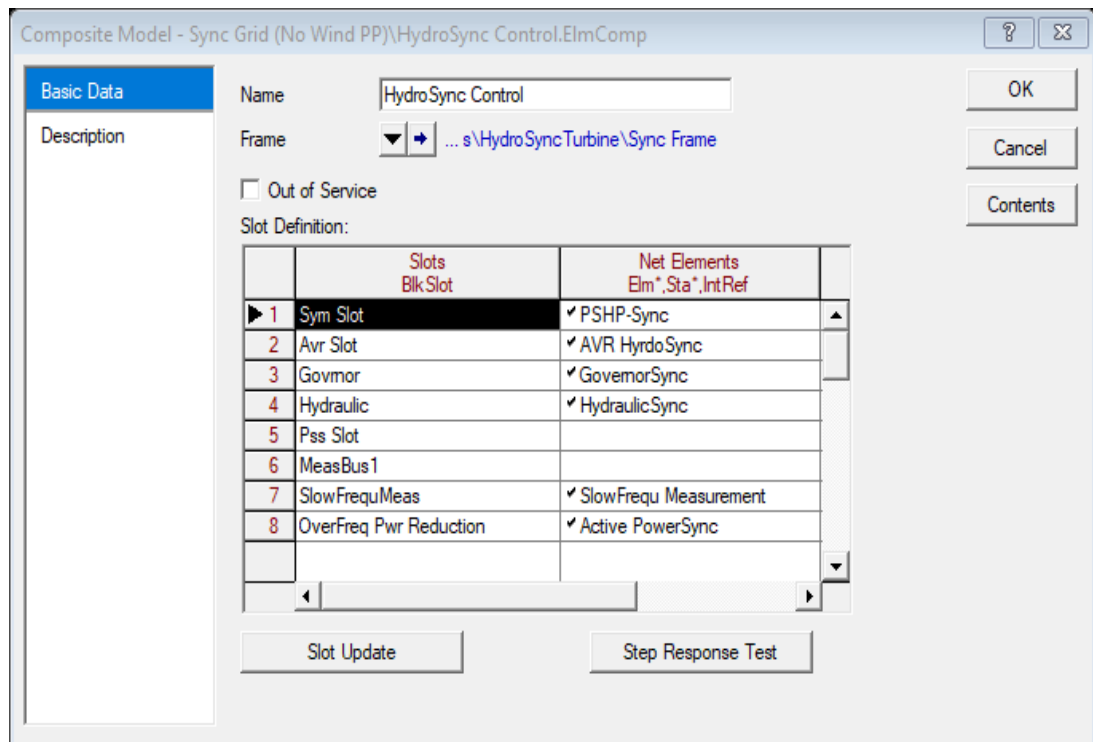





Figure 4.33: SM-PSHP Composite model

4.5. Transient Analysis

Using a dynamic network model, Powerfactory permits three forms of transient analysis: symmetrical steady-state (RMS) network model, three-phase for steady-state (RMS) network model, and electromagnetic transient (EMT) simulation function. Only electromagnetic transient is performed in this work with well-defined steps. The first step in performing a transient simulation is setting up the starting condition. The button () must be clicked to start the system initialization, and a pop-up window with many pre-defined options displays. Then, the user can select one of the following simulation methods: RMS value and Instantaneous Values. The simulation may then be started by selecting () and terminated, if necessary, by selecting ().

4.6. Conclusion

Generators, transmission lines, transformers, loads, and shunt components are just a few of the components that make up power systems. Although they do not have the same parameters, their computer modelling was done according to their parameters with the IEEE 39 bus system, which comprises 39 buses, ten generators, 19 loads, 34 lines, and 12 transformers. IEEE 39 bus system is first modelled without renewable energy. DFIG taken from the DigSilent general templates library was computed and integrated into the existing IEEE 39 bus system. SM-PSHP and DFIM-PSHP have been discussed in detail and modelled. The stability issues can now be dealt with. This will be done in the next chapter.

CHAPTER FIVE: RESULTS AND DISCUSSION

5.1. Introduction

This chapter gives the results and discussion of implementing hydropower plants (PSHP) on the IEEE 39 bus system for stability improvement. IEEE 39 bus system was simulated in the DlgSILENT software package. The study was performed in various scenarios. The first scenario simulated the system without renewable energy to verify the starting conditions. In the second scenario, wind power was integrated into the system and faults were created to study the system stability when disturbances occur. The system stability was improved in the last scenario by implementing two types of hydropower plants, namely the doubly fed induction machine, which is a adjustable speed generator and the synchronous machine, which is a fixed speed generator in the generating operation mode. Comparisons are made with rotor angle and voltage variations for every scenario to point out the impact of the disturbances and determine the best stability improvement method.

5.2. Benchmark case study: 39 Bus system

5.2.1. Scenario 1: Normal operating conditions

IEEE 39 bus system was simulated without renewable energy or fault. This was the first scenario in which the system was operating under normal conditions. This step aimed to verify the starting conditions and show that the system was stable at the beginning of the simulation. The voltage profiles and the rotor angle were used to achieve this aim. The network diagram during load flow is seen in Figure 5.1. The network diagram below depicts the power flow direction. The colour legend is used to signify the network's level of health. To monitor the network's operation, tolerances are specified. The normal voltage working range must be between 0.95 and 1.05 volts. Extreme voltage tolerance falls between 0.9 and 1.1 volts. At 0.95pu, a light blue warning colour legend indicates the situation of low voltage at the designated busbar. The yellow colour of the legend indicates that an overvoltage scenario with an expected voltage of 1.05pu is approaching. The colour legend also displays the system loading, which is a vital component. The orange colour acts as a warning when the equipment is loaded to about 80% of its full capacity. With a 100% loading percentage, the colour red signifies that the equipment is in danger and needs urgent attention. The network was confirmed to be stable after running the load flow simulation. The voltages on the busbars were tested and determined to be within the usual working range (0.95pu-1.05pu). The wires, transformers, and generators are all under 82 per cent loaded.

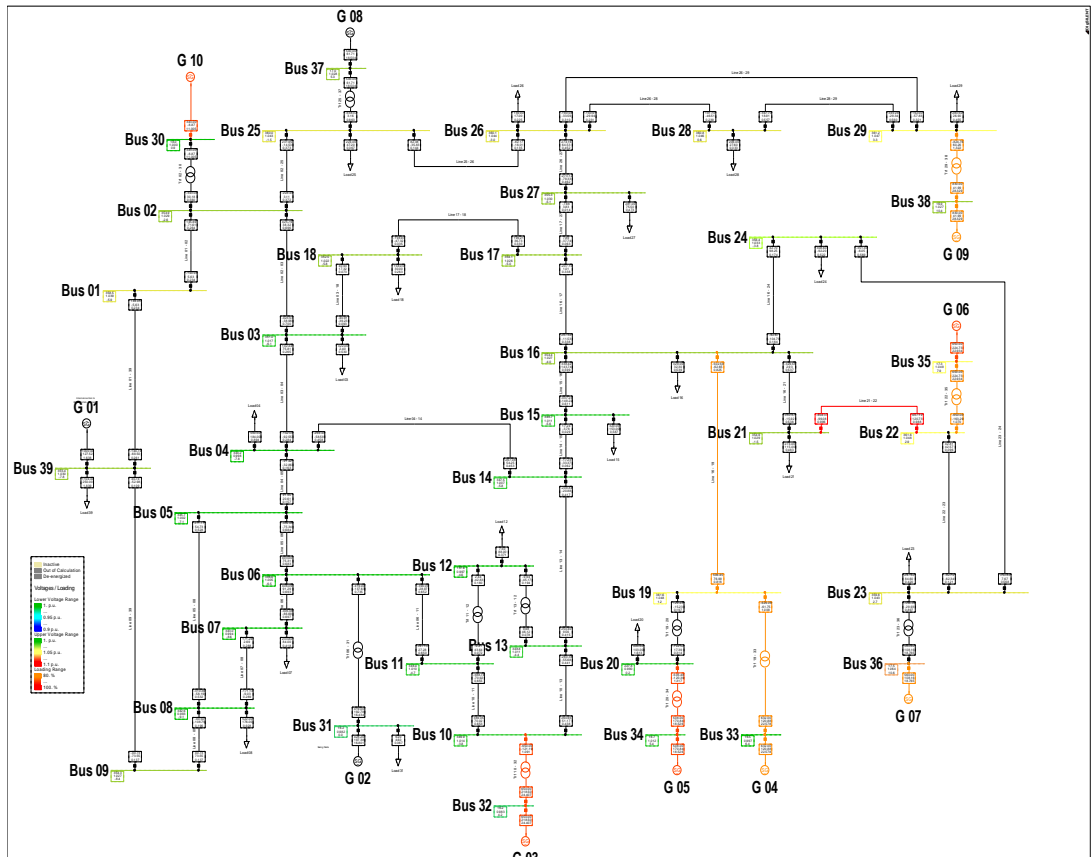


Figure 5.1: Original 39 Bus 10 Machine New England Power System load flow

5.2.1.1. Voltage stability

The voltages of the bus bars are indicated in Table 5.1. According to the South African Network Grid Code, these bus voltages fall within the permitted normal operating range of +/-5% (NERSA, 2020). In addition, the voltage tolerance is listed in Table 5.1 so that the voltage may be monitored relative to its acceptable tolerance. Tables 5.1 and 5.2 demonstrate that the system is well-balanced and stable prior to the occurrence of the fault and before the incorporation of renewable energy.

Table 5.1: Network bus voltage profile in steady-state

Load Flow Calculation										Busbars/Terminals				
AC Load Flow, balanced, positive sequence					Automatic Model Adaptation for Convergence					No				
Automatic Tap Adjust of Transformers					Max. Acceptable Load Flow Error for					1.00 kVA				
Consider Reactive Power Limits					Nodes					0.10 %				
Model Equations														
Grid: Grid		System Stage: Grid			Study Case: Power Flow				Annex: / 1					
	rated	Bus-voltage		Active	Reactive	Power	Power	Factor	Current	Loading	Additional Data			
	Voltage	[kV]	[p.u.]	[kV]	[deg]	[MW]	[Mvar]	[-]	[kA]	[%]				
Bus 08														
	345.00	1.00	343.63	-10.62										
Cub_1	/Lod	Load 08			522.00	176.00	0.95	0.93			P10:	522.00 MW	Q10: 176.00 Mvar	
Cub_2	/Lne	Line 08 - 09			-19.96	-105.94	-0.19	0.18	18.11		Pv:	184.99 kW	cLod: 38.98 Mvar L: 144.02 km	
Cub_3	/Lne	Line 07 - 08			-185.58	-8.19	-1.00	0.31	31.21		Pv:	138.94 kW	cLod: 7.75 Mvar L: 18.25 km	
Cub_4	/Lne	Line 05 - 08			-316.46	-61.88	-0.98	0.54	54.18		Pv:	831.57 kW	cLod: 14.78 Mvar L: 44.44 km	
Bus 07														
	345.00	1.00	343.97	-10.12										
Cub_1	/Lod	Load 07			233.80	84.00	0.94	0.42			P10:	233.80 MW	Q10: 84.00 Mvar	
Cub_2	/Lne	Line 07 - 08			185.72	2.04	1.00	0.31	31.21		Pv:	138.94 kW	cLod: 7.75 Mvar L: 18.25 km	
Cub_3	/Lne	Line 06 - 07			-419.52	-86.04	-0.98	0.72	71.88		Pv:	1101.38 kW	cLod: 11.35 Mvar L: 36.50 km	
Bus 05														
	345.00	1.01	346.83	-8.61										
Cub_1	/Lne	Line 05 - 08			317.29	58.74	0.98	0.54	54.18		Pv:	831.57 kW	cLod: 14.78 Mvar L: 44.44 km	
Cub_2	/Lne	Line 05 - 06			-454.42	-55.95	-0.99	0.76	76.22		Pv:	414.37 kW	cLod: 4.40 Mvar L: 10.32 km	
Cub_3	/Lne	Line 04 - 05			137.14	-2.79	1.00	0.23	22.88		Pv:	148.99 kW	cLod: 13.54 Mvar L: 50.78 km	
Bus 04														
	345.00	1.00	346.33	-9.61										
Cub_1	/Lod	Load 04			500.00	184.00	0.94	0.89			P10:	500.00 MW	Q10: 184.00 Mvar	
Cub_2	/Lne	Line 04 - 14			-270.41	-46.88	-0.99	0.46	45.75		Pv:	593.15 kW	cLod: 14.04 Mvar L: 51.18 km	
Cub_3	/Lne	Line 03 - 04			-92.60	-128.75	-0.58	0.26	26.44		Pv:	289.01 kW	cLod: 22.90 Mvar L: 84.51 km	
Cub_4	/Lne	Line 04 - 05			-136.99	-8.37	-1.00	0.23	22.88		Pv:	148.99 kW	cLod: 13.54 Mvar L: 50.78 km	
Bus 06														
	345.00	1.01	347.65	-7.95										
Cub_1	/Tr2	Trf 06 - 31			-511.61	-116.07	-0.98	0.87	79.58		Tap:	2.00	Min: -2 Max: 2	
Cub_2	/Lne	Line 05 - 06			454.84	56.94	0.99	0.76	76.22		Pv:	414.37 kW	cLod: 4.40 Mvar L: 10.32 km	
Cub_3	/Lne	Line 06 - 07			420.62	91.57	0.98	0.71	71.88		Pv:	1101.38 kW	cLod: 11.35 Mvar L: 36.50 km	
Cub_4	/Lne	Line 06 - 11			-363.85	-32.44	-1.00	0.61	60.67		Pv:	917.08 kW	cLod: 14.17 Mvar L: 32.53 km	
Bus 31														
	16.50	0.98	16.20	0.00										
Cub_1	/Sym	G 02			520.81	198.25	0.93	19.86	79.61		Typ:	SL		
Cub_2	/Lod	Load 31			9.20	4.60	0.89	0.37			P10:	9.20 MW	Q10: 4.60 Mvar	
Cub_3	/Tr2	Trf 06 - 31			511.61	193.65	0.94	19.49	79.58		Tap:	2.00	Min: -2 Max: 2	
Bus 11														
	345.00	1.01	349.38	-6.28										
Cub_1	/Tr2	Trf 11 - 12			-0.06	43.09	-0.00	0.07	14.18		Tap:	1.00	Min: -1 Max: 1	
Cub_2	/Lne	Line 06 - 11			364.76	29.01	1.00	0.60	60.67		Pv:	917.08 kW	cLod: 14.17 Mvar L: 32.53 km	
Cub_3	/Lne	Line 10 - 11			-364.71	-72.10	-0.98	0.61	61.43		Pv:	537.02 kW	cLod: 7.51 Mvar L: 17.06 km	
Bus 12														
	138.00	1.00	138.02	-6.24										
Cub_1	/Lod	Load 12			7.50	88.00	0.08	0.37			P10:	7.50 MW	Q10: 88.00 Mvar	
Cub_2	/Tr2	Trf 11 - 12			0.08	-42.30	0.00	0.18	14.18		Tap:	1.00	Min: -1 Max: 1	
Cub_3	/Tr2	Trf 13 - 12			-7.58	-45.70	-0.16	0.19	15.53		Tap:	1.00	Min: -1 Max: 1	
Bus 10														
	345.00	1.02	350.92	-5.43										
Cub_1	/Tr2	Trf 10 - 32			-650.00	-109.01	-0.99	1.08	86.67		Tap:	2.00	Min: -2 Max: 2	
Cub_3	/Lne	Line 10 - 13			284.76	38.65	0.99	0.47	47.45		Pv:	320.45 kW	cLod: 7.52 Mvar L: 17.06 km	
Cub_4	/Lne	Line 10 - 11			365.24	70.36	0.98	0.61	61.43		Pv:	537.02 kW	cLod: 7.51 Mvar L: 17.06 km	
Bus 32														
	16.50	0.98	16.22	2.57										
Cub_1	/Sym	G 03			650.00	205.14	0.95	24.26	85.20		Typ:	PV		
Cub_2	/Tr2	Trf 10 - 32			650.00	205.14	0.95	24.26	86.67		Tap:	2.00	Min: -2 Max: 2	
Bus 13														
	345.00	1.01	349.94	-6.10										
Cub_1	/Tr2	Trf 13 - 12			7.62	46.64	0.16	0.08	15.53		Tap:	1.00	Min: -1 Max: 1	
Cub_3	/Lne	Line 13 - 14			276.82	-3.92	1.00	0.46	45.69		Pv:	670.54 kW	cLod: 17.68 Mvar L: 40.07 km	
Cub_4	/Lne	Line 10 - 13			-284.43	-42.72	-0.99	0.47	47.45		Pv:	320.45 kW	cLod: 7.52 Mvar L: 17.06 km	

Bus 14													
	345.00	1.01	349.05	-7.66									
	Cub_2	/Lne	Line 04 - 14		271.01	42.41	0.99	0.45	45.75	Pv:	593.15 kW	cLod: 14.04 Mvar	L: 51.18 km
	Cub_4	/Lne	Line 14 - 15		5.14	-36.17	0.14	0.06	6.04	Pv:	5.81 kW	cLod: 37.60 Mvar	L: 86.09 km
	Cub_5	/Lne	Line 13 - 14		-276.14	-6.23	-1.00	0.46	45.69	Pv:	670.54 kW	cLod: 17.68 Mvar	L: 40.07 km
Bus 15													
	345.00	1.02	350.31	-7.74									
	Cub_1	/Lod	Load 15		320.00	153.00	0.90	0.58		P10:	320.00 MW	Q10: 153.00 Mvar	
	Cub_4	/Lne	Line 15 - 16		-314.87	-151.64	-0.90	0.58	57.60	Pv:	1043.53 kW	cLod: 17.92 Mvar	L: 37.29 km
	Cub_5	/Lne	Line 14 - 15		-5.13	-1.36	-0.97	0.01	6.04	Pv:	5.81 kW	cLod: 37.60 Mvar	L: 86.09 km
Bus 20													
	230.00	0.99	227.97	-2.01									
	Cub_1	/Lod	Load 20		628.00	103.00	0.99	1.61		P10:	628.00 MW	Q10: 103.00 Mvar	
	Cub_2	/Tr2	Trf 19 - 20		-122.51	12.61	-0.99	0.31	12.43	Tap:	2.00	Min: -2	Max: 2
	Cub_3	/Tr2	Trf 20 - 34		-505.49	-115.61	-0.97	1.31	87.98	Tap:	1.00	Min: -1	Max: 1
Bus 19													
	345.00	1.05	362.20	-1.02									
	Cub_1	/Tr2	Trf 19 - 20		122.62	-10.48	1.00	0.20	12.43	Tap:	2.00	Min: -2	Max: 2
	Cub_2	/Tr2	Trf 19 - 33		-629.10	-51.14	-1.00	1.01	80.41	Tap:	2.00	Min: -2	Max: 2
	Cub_3	/Lne	Line 16 - 19		506.49	61.62	0.99	0.81	81.90	Pv:	3813.03 kW	cLod: 32.93 Mvar	L: 77.37 km
Bus 34													
	16.50	1.01	16.70	3.17									
	Cub_1	/Sym	G 05		508.00	165.76	0.95	18.47	89.06	Typ:	PV		
	Cub_2	/Tr2	Trf 20 - 34		508.00	165.76	0.95	18.47	87.98	Tap:	1.00	Min: -1	Max: 1
Bus 33													
	16.50	1.00	16.45	4.19									
	Cub_1	/Sym	G 04		632.00	109.91	0.99	22.51	80.19	Typ:	PV		
	Cub_2	/Tr2	Trf 19 - 33		632.00	109.91	0.99	22.51	80.41	Tap:	2.00	Min: -2	Max: 2
Bus 36													
	16.50	1.06	17.55	8.32									
	Cub_1	/Sym	G 07		560.00	101.18	0.98	18.72	81.30	Typ:	PV		
	Cub_2	/Tr2	Trf 23 - 36		560.00	101.18	0.98	18.72	76.44	Tap:	0.00	Min: 0	Max: 0
Bus 23													
	345.00	1.04	360.45	0.47									
	Cub_5	/Lod	Load 23		247.50	84.60	0.95	0.42		P10:	247.50 MW	Q10: 84.60 Mvar	
	Cub_1	/Tr2	Trf 23 - 36		-558.57	-23.30	-1.00	0.90	76.44	Tap:	0.00	Min: 0	Max: 0
	Cub_3	/Lne	Line 22 - 23		-42.77	-61.82	-0.57	0.12	12.04	Pv:	24.77 kW	cLod: 20.25 Mvar	L: 38.09 km
	Cub_4	/Lne	Line 23 - 24		353.84	0.51	1.00	0.57	56.68	Pv:	2531.60 kW	cLod: 39.13 Mvar	L: 138.86 km
Bus 22													
	345.00	1.05	362.18	0.67									
	Cub_1	/Tr2	Trf 22 - 35		-650.00	-151.68	-0.97	1.06	81.46	Tap:	1.00	Min: -1	Max: 1
	Cub_2	/Lne	Line 22 - 23		42.80	41.97	0.71	0.10	12.04	Pv:	24.77 kW	cLod: 20.25 Mvar	L: 38.09 km
	Cub_3	/Lne	Line 21 - 22		607.20	109.71	0.98	0.98	99.08	Pv:	2787.73 kW	cLod: 27.79 Mvar	L: 55.54 km
Bus 37													
	16.50	1.03	16.96	2.42									
	Cub_1	/Sym	G 08		540.00	0.44	1.00	18.38	77.14	Typ:	PV		
	Cub_2	/Tr2	Trf 25 - 37		540.00	0.44	1.00	18.38	75.06	Tap:	1.00	Min: -1	Max: 1
Bus 35													
	16.50	1.05	17.31	5.63									
	Cub_1	/Sym	G 06		650.00	212.41	0.95	22.80	85.48	Typ:	PV		
	Cub_2	/Tr2	Trf 22 - 35		650.00	212.41	0.95	22.80	81.46	Tap:	1.00	Min: -1	Max: 1
Bus 24													
	345.00	1.04	357.87	-6.07									
	Cub_1	/Lod	Load 24		308.60	-92.20	0.96	0.52		P10:	308.60 MW	Q10: -92.20 Mvar	
	Cub_4	/Lne	Line 16 - 24		42.71	91.56	0.42	0.16	17.37	Pv:	30.37 kW	cLod: 7.28 Mvar	L: 23.41 km
	Cub_5	/Lne	Line 23 - 24		-351.31	0.64	-1.00	0.57	56.68	Pv:	2531.60 kW	cLod: 39.13 Mvar	L: 138.86 km
Bus 21													
	345.00	1.03	355.96	-3.78									
	Cub_1	/Lod	Load 21		274.00	115.00	0.92	0.48		P10:	274.00 MW	Q10: 115.00 Mvar	
	Cub_2	/Lne	Line 16 - 21		330.42	-26.29	1.00	0.54	53.76	Pv:	821.67 kW	cLod: 27.12 Mvar	L: 53.56 km
	Cub_3	/Lne	Line 21 - 22		-604.42	-88.71	-0.99	0.99	99.08	Pv:	2787.73 kW	cLod: 27.79 Mvar	L: 55.54 km

Table 5.2 displays a summary of the results for the IEEE 39 bus network grid during steady-state load flow operation. In addition, the network's total number of power system components is shown. The installed functional power generation capacity is 14535MW, the total load demand is 6097.1MW, the grid power losses are 43.71MW, and the generated active power is 6140.81MW. The generation spinning reserves are also 8394.19MW, which is the power used when load demand increases.

Table 5.2: Network grid summary

Load Flow Calculation				Total System Summary			
AC Load Flow, balanced, positive sequence				Automatic Model Adaptation for Convergence			
Automatic Tap Adjust of Transformers				No	Max. Acceptable Load Flow Error for		No
Consider Reactive Power Limits				No	Nodes		1.00 kVA
				Model Equations		0.10 %	
Total System Summary				Study Case: Power Flow		Annex: / 1	
No. of Substations	0	No. of Busbars	39	No. of Terminals	0	No. of Lines	34
No. of 2-w Trfs.	12	No. of 3-w Trfs.	0	No. of syn. Machines	10	No. of asyn.Machines	0
No. of Loads	19	No. of Shunts	0	No. of SVS	0		
Generation	= 6140.81 MW	1250.37 Mvar	6266.82 MVA				
External Infeed	= 0.00 MW	0.00 Mvar	0.00 MVA				
Load P(U)	= 6097.10 MW	1408.90 Mvar	6257.77 MVA				
Load P(Un)	= 6097.10 MW	1408.90 Mvar	6257.77 MVA				
Load P(Un-U)	= -0.00 MW	0.00 Mvar					
Motor Load	= 0.00 MW	0.00 Mvar	0.00 MVA				
Grid Losses	= 43.71 MW	-158.53 Mvar					
Line Charging	=	-1109.50 Mvar					
Compensation ind.	=	0.00 Mvar					
Compensation cap.	=	0.00 Mvar					
Installed Capacity	= 14535.00 MW						
Spinning Reserve	= 8394.19 MW						
Total Power Factor:							
Generation	= 0.98 [-]						
Load/Motor	= 0.97 / 0.00 [-]						

During the steady-state analysis, system voltages are an additional crucial component to consider. The voltages of the system should be within 5% of their nominal value limitations (NERSA, 2020). The system voltages should thus be between 0.95pu and 1.05pu per unit. Figure 5.2 demonstrates that the minimum measured bus voltage is 0.98pu (bus 31), while the highest observed bus voltage is 1.06pu (bus 36). The y-axis represents the per-unit voltage measured at the bus terminals, while the x-axis represents the bus bar in the network.

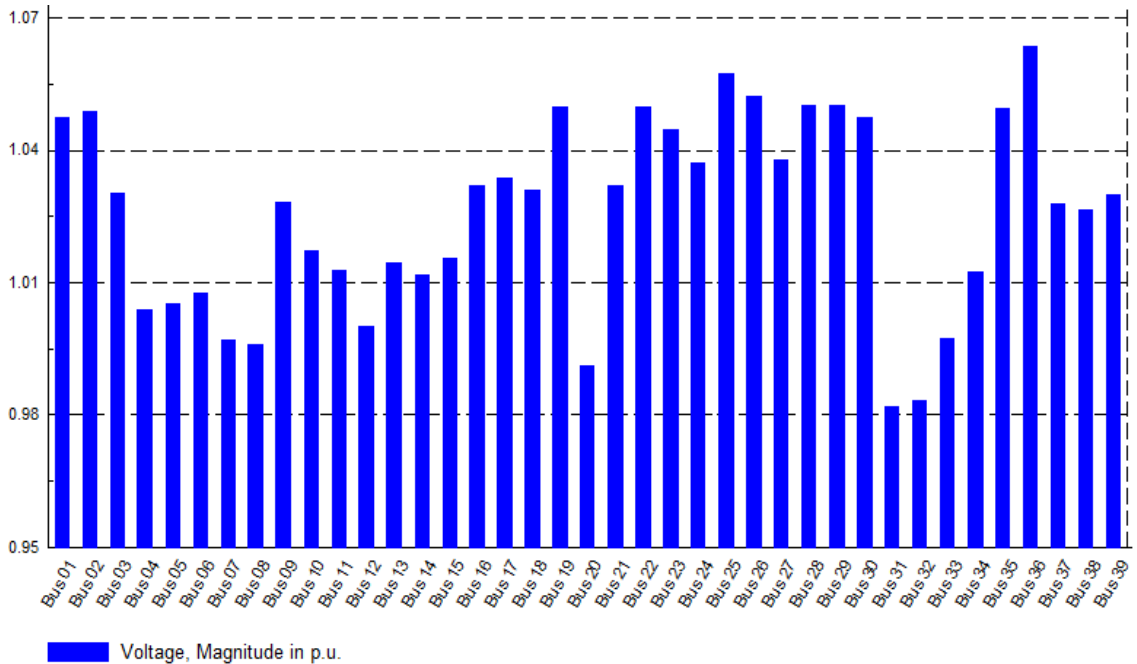


Figure 5.2: Network bus bar voltages

5.2.1.2. Rotor angle stability

Simulation is performed when there is no disturbance. The y-axis in Figure 5.3 illustrates the rotor angles of all the system's generators in degrees, with the x-axis representing the simulation length period, which is set to 70 seconds. All generator's rotor angles were observed to be the same during steady-state simulation with no oscillation. In (Alizadeh Bidgoli & Gonzalez-Longatt, 2021) and (Alizadeh Bidgoli et al., 2021), rotor angles present oscillations when the fault occurs, showing that the stability is disturbed. However, Figure 5.3 shows that rotor angles give no oscillations when there is no fault. This means that the system remains stable and healthy in this scenario under normal operating conditions

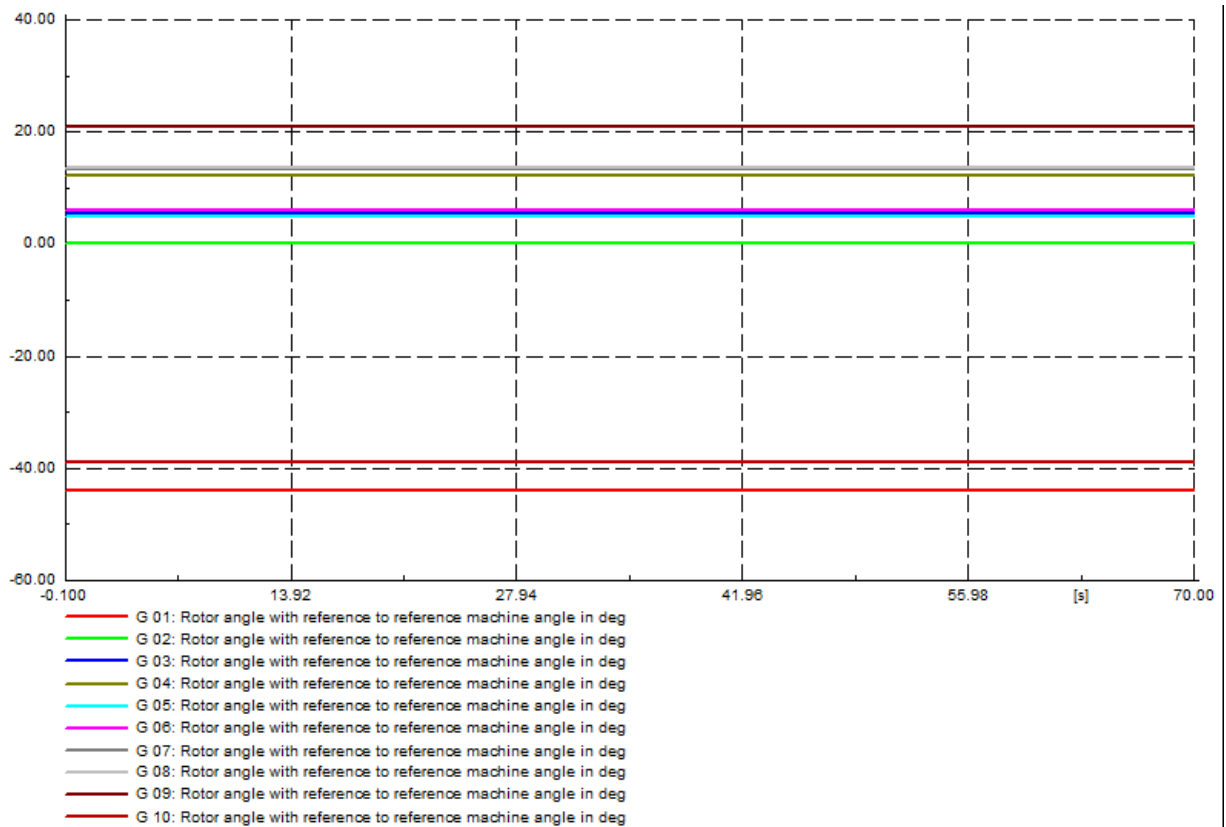


Figure 5.3: Generators' rotor angles in steady state

Using generator 1 for deeper studies, Figure 5.4 shows that its rotor angle values were -44.007 degrees throughout the simulation. This supports what was mentioned before regarding the results presented in (Alizadeh Bidgoli & Gonzalez-Longatt, 2021) and (Alizadeh Bidgoli et al., 2021). The absence of oscillation and the stable rotor angle value show that the system is stable and healthy before the fault occurs. According to (Chen et al., 2017) and (ISO, 2017), in which an illustration in determining the acceptable damping criteria for the 39 bus system is described, the power grid is regarded as stable when the rotor angles are at a nominal state.

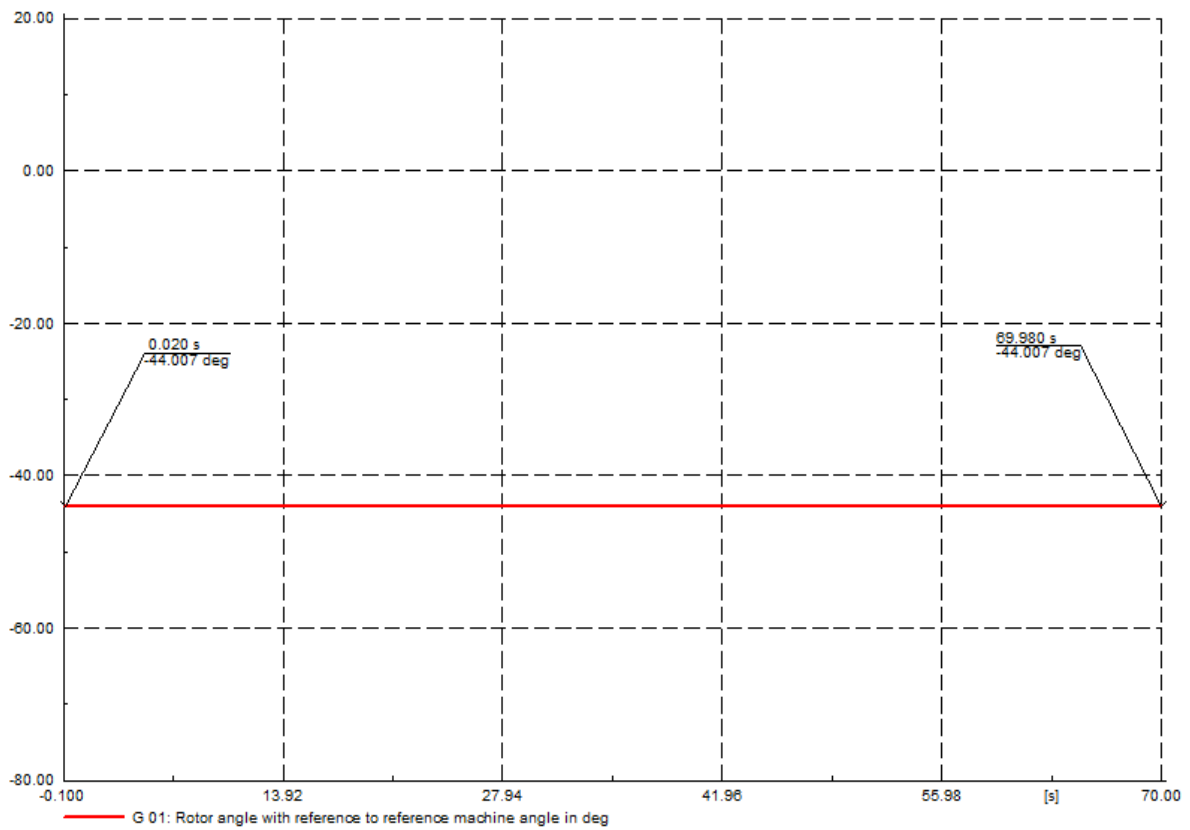


Figure 5.4: Generator 1 rotor angle in steady state

5.2.2. Scenario 2: 100MW of Wind integration

The previous section's results show that the system is stable under normal operating conditions. In this scenario, 100MW of wind power is integrated into the 39 bus system (Alizadeh Bidgoli & Gonzalez-Longatt, 2021). Figure 5.5 shows the load flow running with wind power (100MW) connected to bus 30. the effects of wind power integration on system stability are discussed.

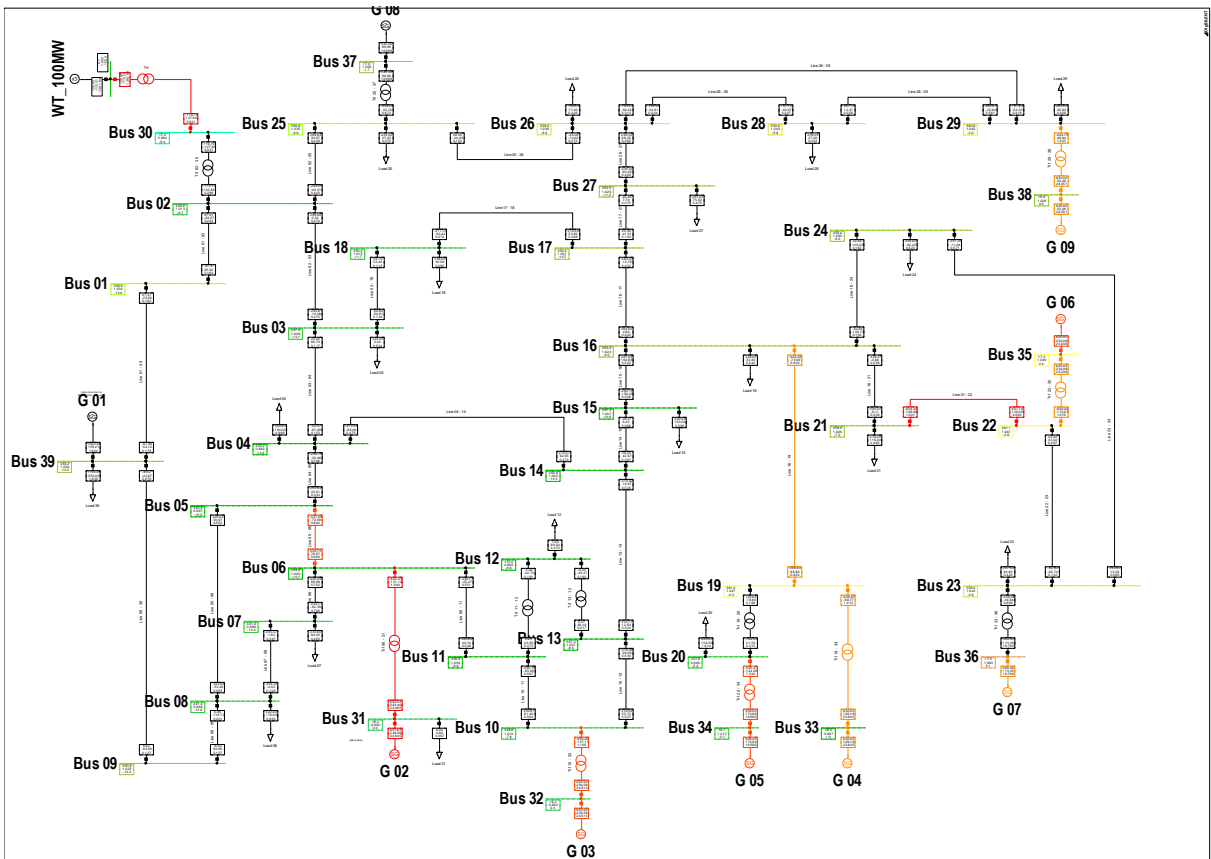


Figure 5.5: Wind integrated 39 Bus system

5.2.2.1. Voltage stability

Figure 5.6 demonstrates that when renewable energy is included into the system, the voltage oscillates from the beginning of the simulation until the fault occurs when renewable energy is not incorporated. The maximum voltage oscillations of bus 33 rise by around 30% compared to when no wind power is used. Although the system only regains steady state after 18 seconds, wind energy integration causes a disturbance in the system stability.

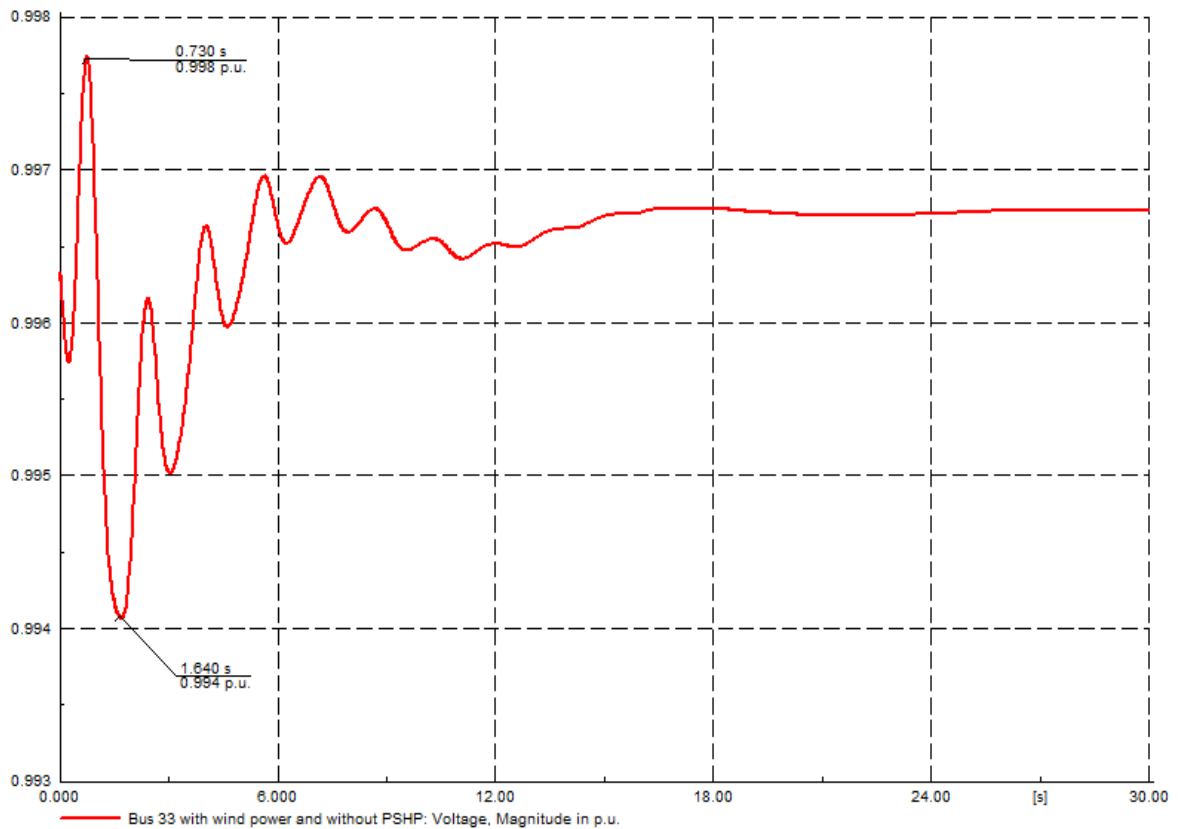


Figure 5.6: Bus 33 voltage with wind power and without PSHP

5.2.2.2. Rotor angle stability

In figure 5.7, the findings for the generator 1 angle clearly show that the integration of wind power brings a disturbance to the system. When looking at the generator 1 angle response in Figure 5.7, we can see that the generator 1 rotor angle oscillates from the simulation's beginning with an angle of -36.322 degrees instead of 44.007 degrees as in Figure 5.4 and its oscillations increase when the fault occurs. It has a maximal negative angle peak at -34.297 degrees and a minimum negative angle peak of -37.415, where it settles down in 18 seconds. As defined in (ISO, 2017), the oscillations increased range is still acceptable as the oscillations of the rotor angle seen in Figure 5.7 disappear in 12 seconds. Moreover, the generator 1 rotor angle becoming stable again at 18 seconds show that the system is still stable.

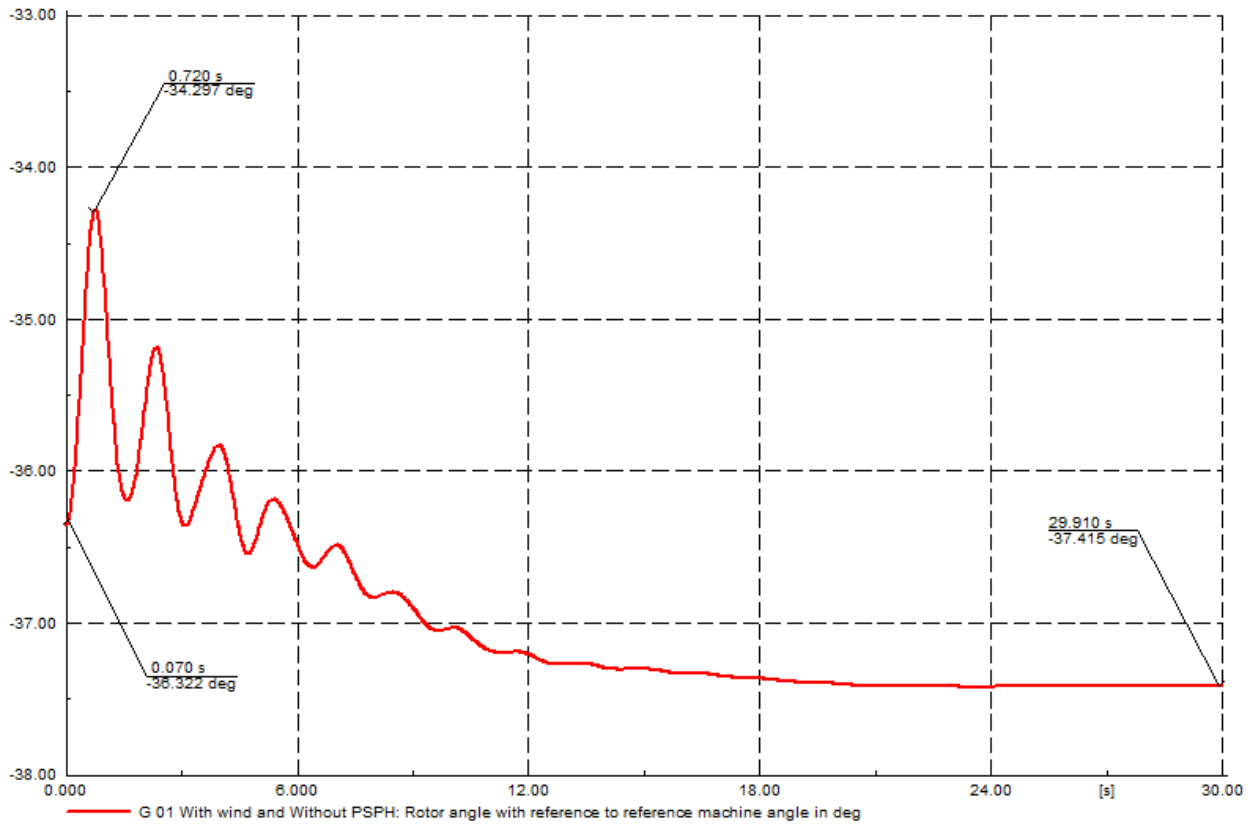


Figure 5.7: Generator 1 rotor angle with wind power and without PSHP

5.2.3. Scenario 3: 150-millisecond fault at bus 30

In this scenario, a 150-millisecond fault is applied at bus 30 at the 10th second of the simulation (Alizadeh Bidgoli & Gonzalez-Longatt, 2021).

5.2.3.1. Voltage stability

Figure 5.8 shows that when the fault occurs at 10 seconds, Bus 33 voltage is temporarily reduced to low levels until the fault is cleared in 10.15 seconds. This also holds true for the voltages of other adjacent buses. This implies that voltage dips are inevitable and tolerated under certain conditions. After a stable fault has been eliminated, the system oscillates to the post-fault state and the voltages trend toward the post-fault steady-state level. The "back-swing," a significant transient voltage drop caused by the demand for post-fault accelerating power, is superimposed over transitory oscillation after the fault has been rectified. The voltage sag module is based on the limits provided for this post-fault voltage sag characteristic, as outlined in the document (Chen et al., 2017). The minimum post-fault voltage sag must remain above 70% of the nominal voltage within 10 seconds following a fault. Although Bus33's voltage oscillation reaches 1.045pu (highest) and 0.815pu (lowest), it regains its initial value of 1.00 pu when the fault is cleared. Figure 5.8 shows that bus 33 voltage recovers a steady state after the fault is cleared, respecting the above characteristic. So the system remains stable.

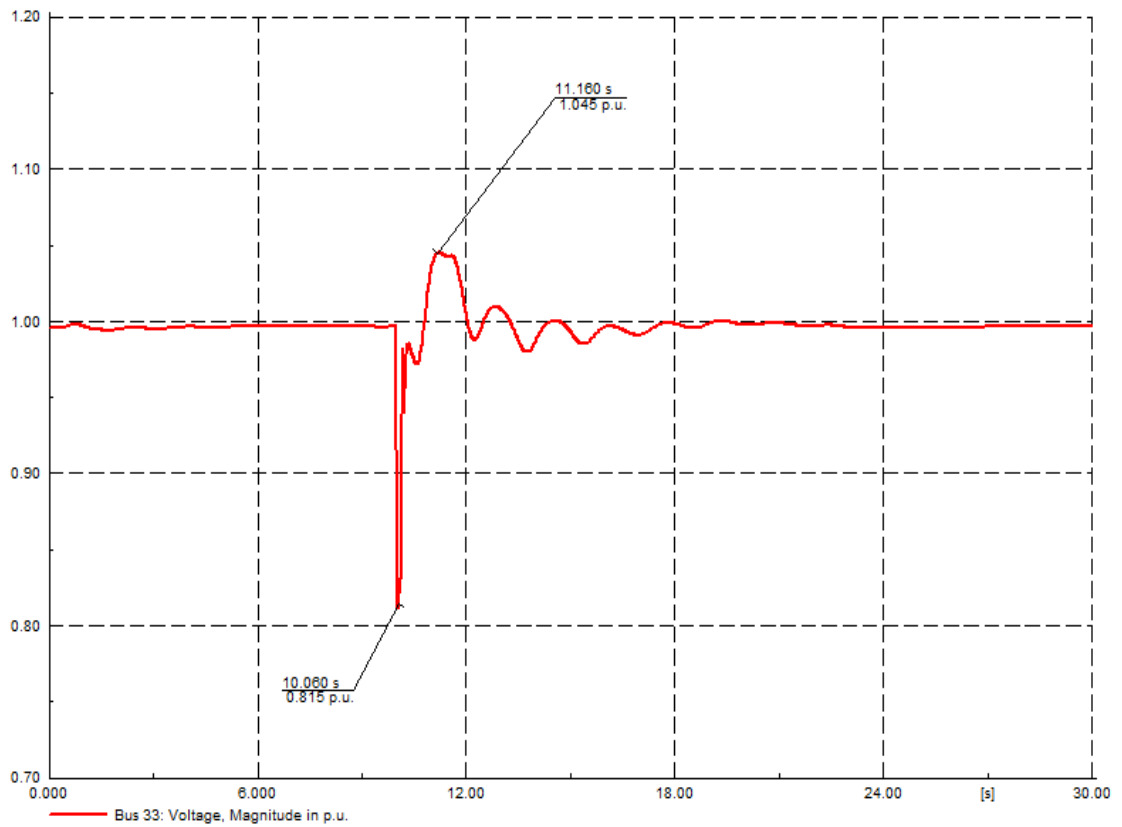


Figure 5.8: Bus 33 voltage with wind power and without PSHP for a 150ms fault at bus 30

5.2.3.2. Rotor angle stability

Figure 5.9 shows the generator angle response. Generator 1 rotor angle is disturbed from the beginning of the simulation with the same values seen in figure 5.7. Generator 1 has the maximal negative angle peak at -14.565, and a minimum negative angle peak of -53.356 degrees after the fault has occurred and settles down at -37.294 in 26 seconds. According to Figures 5.8 and 5.9, the system's stability deteriorated by incorporating wind power into the power grid and when the fault occurred. This is because, when additional wind farms are incorporated, the original simultaneous system's inertia decreases, making it more susceptible to external disturbances. Although the generator one rotor angle oscillates as the fault occurs, according to (Chen et al., 2017) and (ISO, 2017), in which an example for the determination of acceptable damping criteria for 39 bus system is described, the power grid is regarded as being stable when the rotor angles are at nominal state.

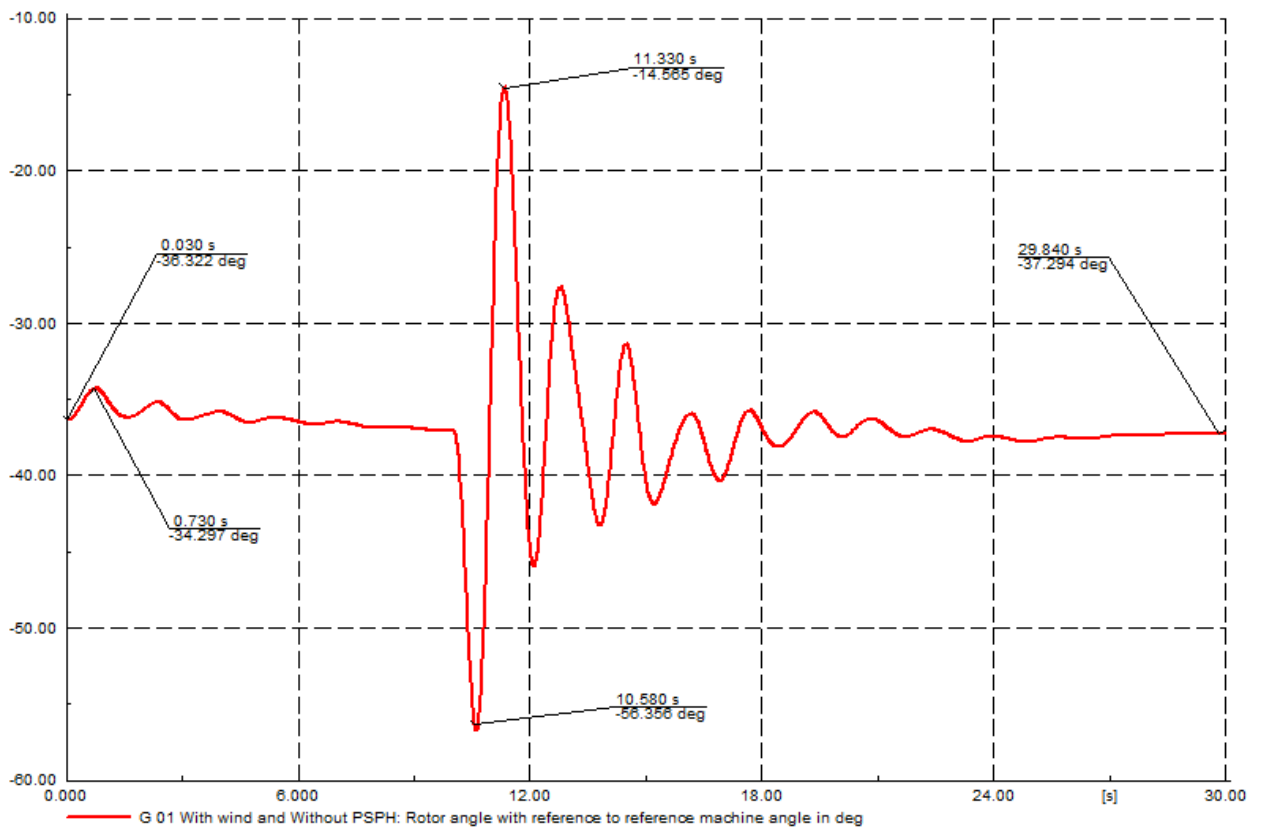


Figure 5.9: Generator 1 rotor angle with wind power and without PSHP for a 150ms fault at bus

30

5.2.4. Scenario 4: 450-millisecond fault at bus 30

In this scenario, the simulation increases the fault duration on bus 30 from 150 milliseconds to 450 milliseconds. This scenario shows the severity of the fault when it lasts longer.

5.2.4.1. Voltage stability

Figure 5.10 shows the oscillations in the Bus 33 voltage throughout a 30-second simulation study. The voltage oscillations are unstable, and all machines lose synchronism due to the occurrences. The voltage sag module is based on the restrictions defined for this post-fault voltage sag characteristic, as described by (Chen et al., 2017). The minimum post-fault voltage drop shall stay above 70% of nominal voltage and not fall below 80% of nominal voltage for more than 250 milliseconds within 10 seconds after a failure. Figure 5.10 demonstrates that the voltage on bus 33 does not return to a steady state when the defect is repaired, and the voltage drop does not adhere to the aforementioned profile. Therefore, the system has lost synchronism.

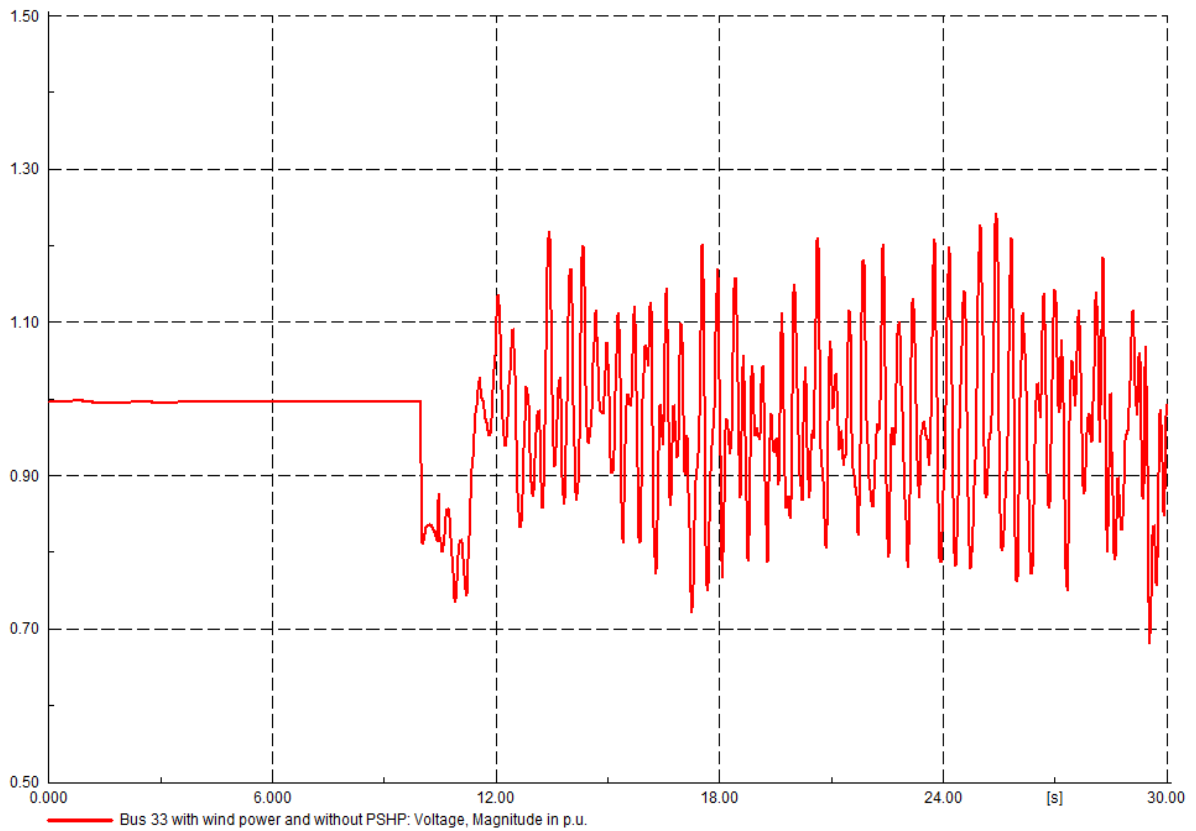


Figure 5.10: voltage profile at Bus 33 for a 450ms fault at bus 30

5.2.4.2. Rotor angle stability

The results indicate that the increase in fault duration affects the system's instability. As seen in Figure 5.11, which shows the generator 1 rotor angle reaction during the disturbance, generator 1 is out of step, as indicated in Table 5.3. In other words, the system is desynchronized after 11.952 seconds. These results reveal that wind integration can be considered a disturbance in a system. Results also demonstrate that disturbances such as faults can cause the system to lose stability if it takes too long to be cleared.

Table 5.3: Generator 1 out of step

```
DIgSI/pcl - (t=11:952 s) -----
DIgSI/pcl - (t=11:952 s) 'Grid\G 01 With wind and Without PSPH.ElmSym':
DIgSI/pcl - (t=11:952 s) Generator out of step (pole slip).
```

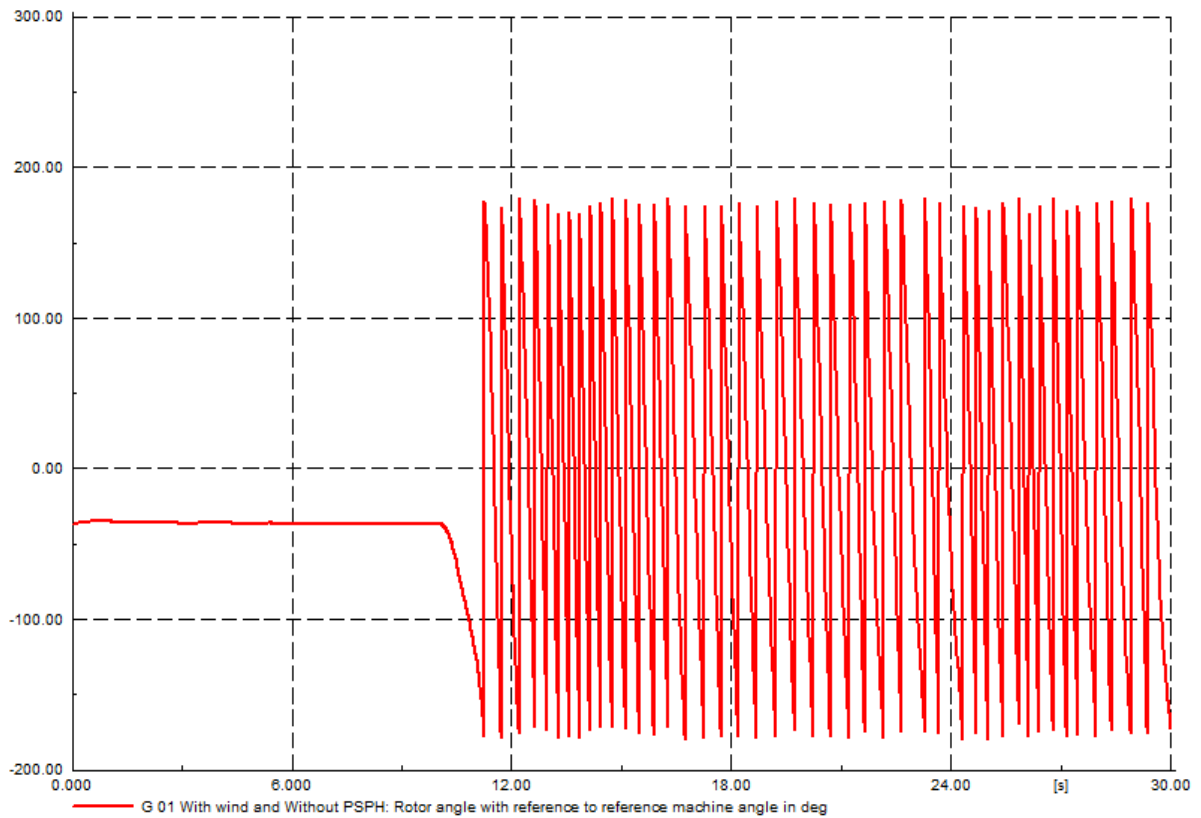


Figure 5.11: Generator 1 out of step for a 450ms fault at bus 30

5.3. Proposed solutions

To enhance the system's stability, the generator angle and voltage oscillations should be reduced, and their oscillation time should be shortened. To achieve this, two types of pumper storage hydropower plants are used, as proposed in (Alizadeh Bidgoli & Gonzalez-Longatt, 2021) and (Alizadeh Bidgoli et al., 2021).

5.3.1. Case study 1: Synchronous Machine Pumped Storage HydroPower (SM-PSHP).

This study case presents the stability improvement using SM-based PSHP. Keeping the 100 MW of wind power at bus 30, the last generator, which is G10 located at bus 30, is replaced by SM-based PSHP of 243 MW and the other parameters are computed as in Tables 4.1-4.4. Figure 5.12 shows what this system looks like when load flow is running. Simulation results are provided with different events, as seen in (Alizadeh Bidgoli & Gonzalez-Longatt, 2021) when a 150-millisecond fault occurs at bus 30 ten seconds after the simulation has started. Results are also provided for a 450-millisecond fault at bus 30.

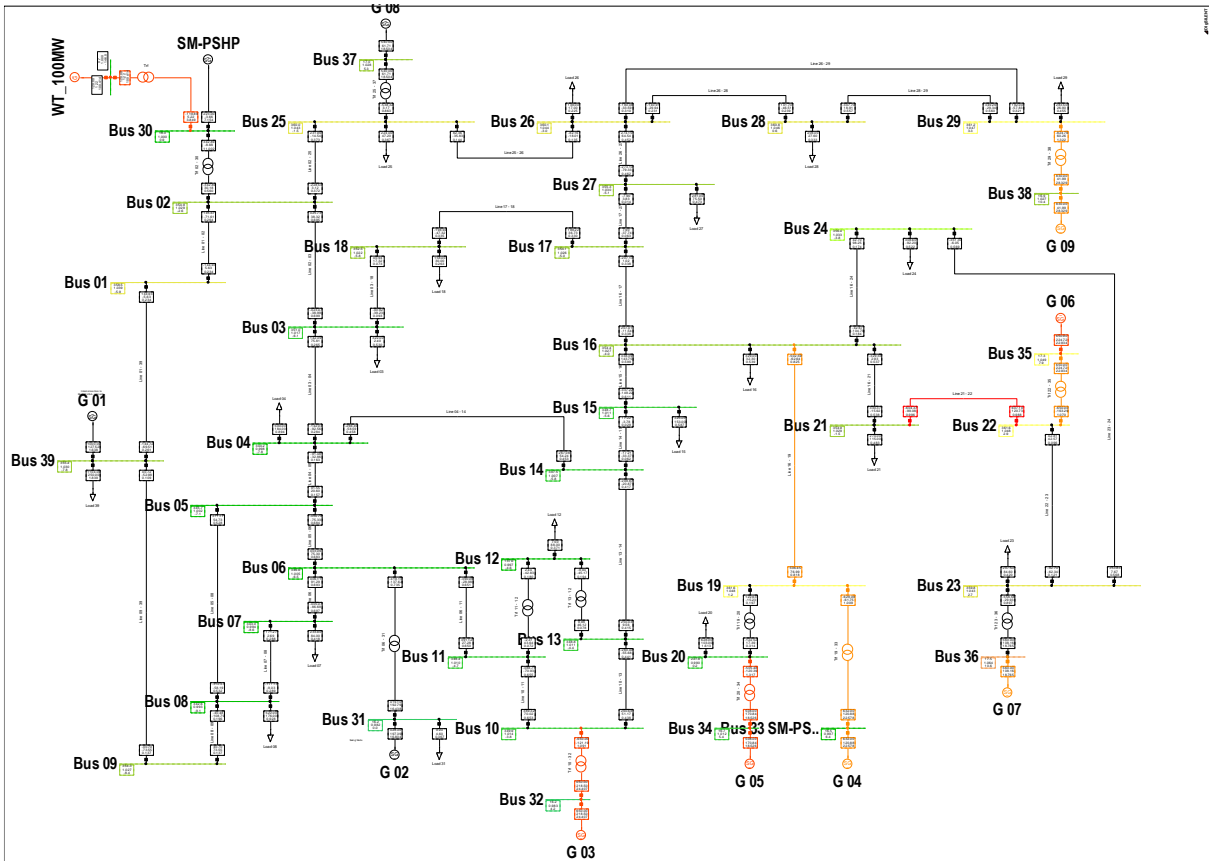


Figure 5.12: Load flow running of the wind-integrated SM-PSHP 39 bus system

5.3.1.1. Scenario 1: 150-millisecond fault at bus 30

In this scenario, a 150-millisecond fault is applied at bus 30 at the 10th second of the simulation and SM-PSHP is used to enhance the system stability as proposed in (Alizadeh Bidgoli & Gonzalez-Longatt, 2021) and (Alizadeh Bidgoli et al., 2021)

5.3.1.1.1. Voltage stability

Figure 5.13 shows that when incorporating the SM-PSHP after the fault occurs at 10 seconds, Bus 33 voltage is temporarily reduced to dangerously low levels until the fault is cleared in 10.15 seconds. This also stands true for the voltages of other nearby buses. This implies that voltage dips are inevitable and tolerated under certain conditions. After the fault is cleared, however, the system oscillates to the post-fault state, and the voltages reach the post-fault steady-state level. The Voltage Sag Module is based on the limits set for this post-fault voltage sag characteristic, as outlined in the document (Chen et al., 2017). The minimum post-fault voltage sag must remain above 70% of the nominal voltage within 10 seconds following a fault. Although Bus33's voltage oscillation reaches 1.039pu (highest) and 0.816pu (lowest), it regains its initial value of 1.00 pu when the fault is cleared. Figure 5.13 shows that not only bus 33 voltage regains a steady state after the fault is cleared, respecting the characteristic mentioned earlier, oscillations are slightly damped with SM-PSHP.

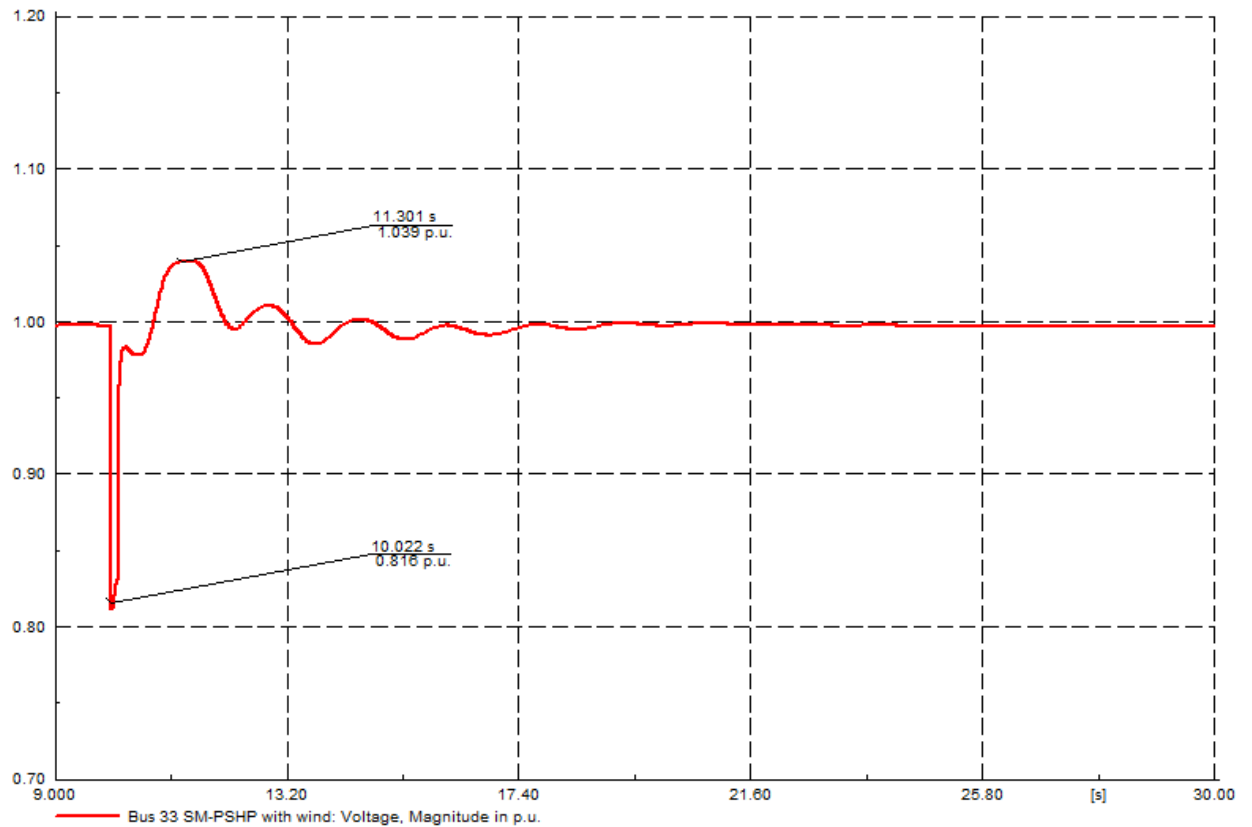


Figure 5.13: Bus 33 voltage with SM-PSHP and wind power for a 150ms fault at bus 30

5.3.1.1.2. Rotor angle stability

Generator 1 rotor angle is disturbed from the beginning of the simulation with the same values when looking at its response in Figure 5.14. but generator 1 has the maximal negative angle peak at -16.550 degrees and a minimum negative angle peak of -52.768 degrees after the fault has occurred and settles down at -36.397 degrees in 26 seconds. According to the observation of Figure 5.14, the system's stability deteriorated not only by incorporating wind power into the power grid but also when the fault occurs is slightly improved when using in the SM-PSHP at bus 30 instead of G10. Figure 5.14 shows that not only generator 1 regains steady state after the fault is cleared, respecting the characteristic mentioned earlier but also oscillations are slightly damped with the use of SM-PSHP. Although the generator 1 rotor angle oscillates as the fault occurs, according to (Chen et al., 2017) and (ISO, 2017), in which an example for the determination of acceptable damping criteria for 39 bus system is described, The power grid is regarded as being stable when the rotor angles are at nominal state.

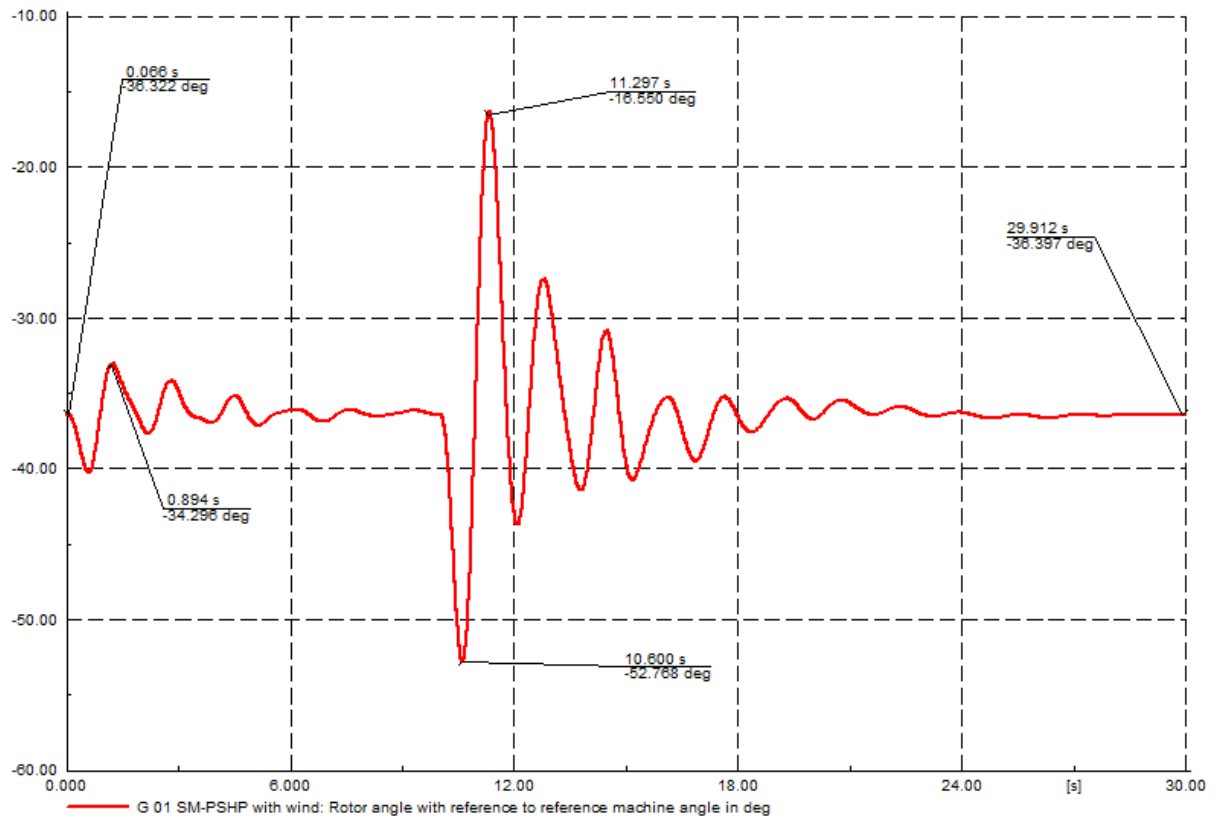


Figure 5.14: Generator 1 rotor angle with SM-PSHP and wind power for a 150ms fault at bus 30

5.3.1.2. Scenario 2: 450-millisecond fault at bus 30

This scenario presents the increase in the duration of the fault on bus 30 from 150-millisecond to 450-millisecond. This is a unique scenario not presented in (Alizadeh Bidgoli & Gonzalez-Longatt, 2021) and (Alizadeh Bidgoli et al., 2021). In this scenario, the fault lasts longer, and the system stability is more affected. This scenario is important as it shows the effectiveness of the PSHP in stability improvement. Although the fault lasts longer, the PSHP can improve system stability.

5.3.1.2.1. Voltage stability

Bus 33 voltage oscillates to low and high levels until the fault is cleared after 10.45 seconds, as seen in Figure 5.15. This is also the case with the voltages on the other nearby buses. This indicates that stat voltage dips are inevitable and reasonable under certain conditions. After the fault has been rectified, the system oscillates to the post-fault state, and the voltages gravitate toward the post-fault steady-state level. The "back-swing," a significant transient voltage drop caused by the demand for post-fault accelerating power, is superimposed over transitory oscillation after the fault has been rectified. The Voltage Sag Module is based on the limits set for this post-fault voltage sag characteristic, as outlined by (Chen et al., 2017). The minimum post-fault voltage sag must remain above 70% of the nominal voltage within 10 seconds following a fault. Although Bus33's voltage oscillation reaches 1.150pu (highest) and 0.813pu (lowest), it regains its initial value of 1.00 pu when the fault is cleared. Figure 5.15 shows that

not only bus 33 voltage recover a steady state after the fault is cleared, respecting the characteristic mentioned earlier, oscillations are slightly damped with SM-PSHP.

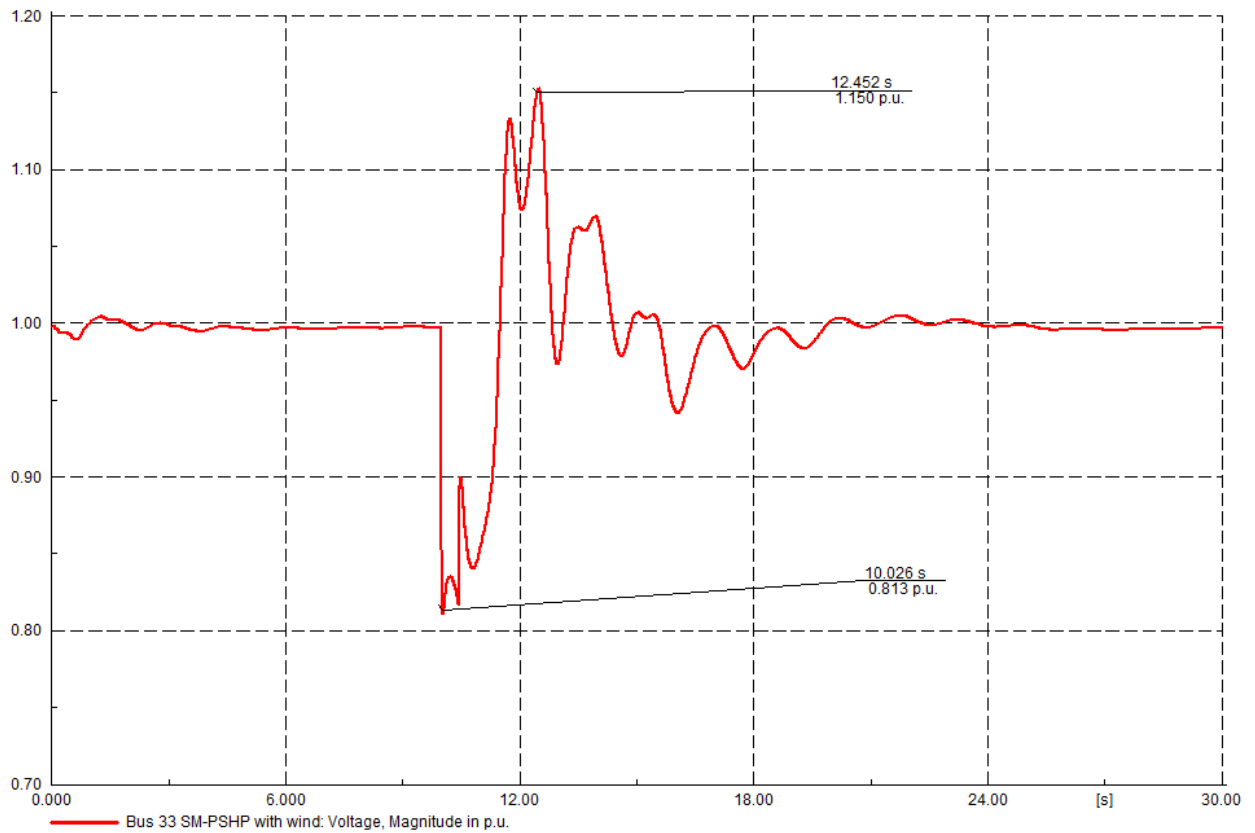


Figure 5.15: Bus 33 voltage with SM-PSHP and wind power for a 450ms fault at bus 30

5.3.1.2.2. Rotor angle stability

The results indicate that the increase in fault duration also increases the system instability. Figure 5.16 shows generator 1 rotor angle reaction during the disturbance. The positive and negative peaks of the angle response oscillate with 60.953 degrees as the maximum value and -123.361 degrees as the minimum value before the system regains transient stability within 26 seconds. Figure 5.16 shows that not only generator 1 retrieves a steady state after the fault is cleared, respecting the characteristic mentioned earlier, but oscillations are also slightly damped with the use of SM-PSHP. Although the generator 1 rotor angle oscillates as the fault occurs, according to (Chen et al., 2017) and (ISO, 2017), which describes the acceptable damping criteria for 39 bus system. the power grid is still stable when the rotor angles are at a nominal state.

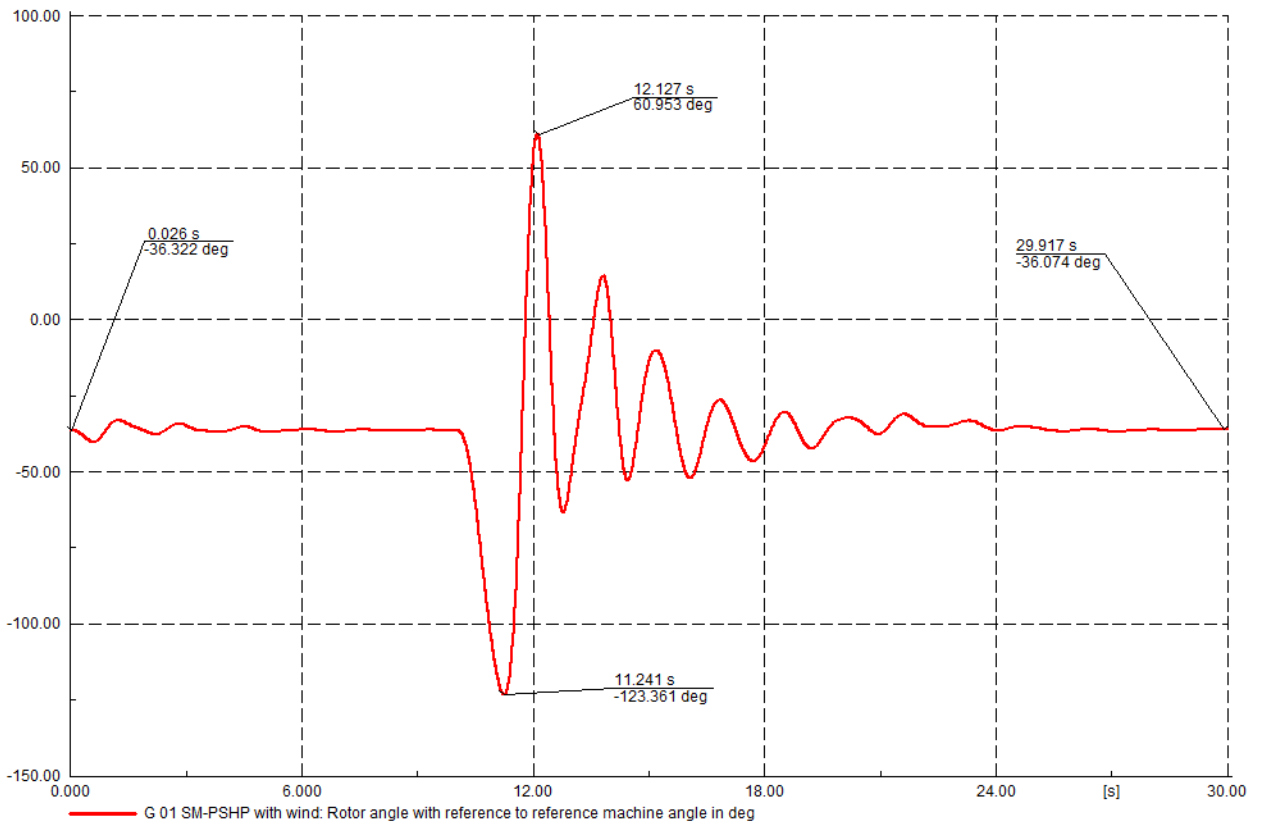


Figure 5.16: Generator 1 rotor angle with SM-PSHP and wind power for a 450ms fault at bus 30

5.3.2. Case study 2: Doubly Fed Induction Machine Pumped Storage HydroPower (DFIM-PSHP)

In this case study, stability improvement is made using DFIM-based PSHP. As in the previous case study, the 100 MW of wind power at bus 30 is kept, but the last generator, G10, located at bus 30, replaced DFIM-based PSHP of 243 MW, and the other parameters are computed as in Tables 4.1-4.4. Figure 5.17 shows what this system looks like when load flow is running. Simulated results are provided with different events, as seen in (Alizadeh Bidgoli & Gonzalez-Longatt, 2021) when a 150-millisecond fault occurs at bus 30 ten seconds after the simulation has started. Results are also provided for a 450-millisecond fault at bus 30.

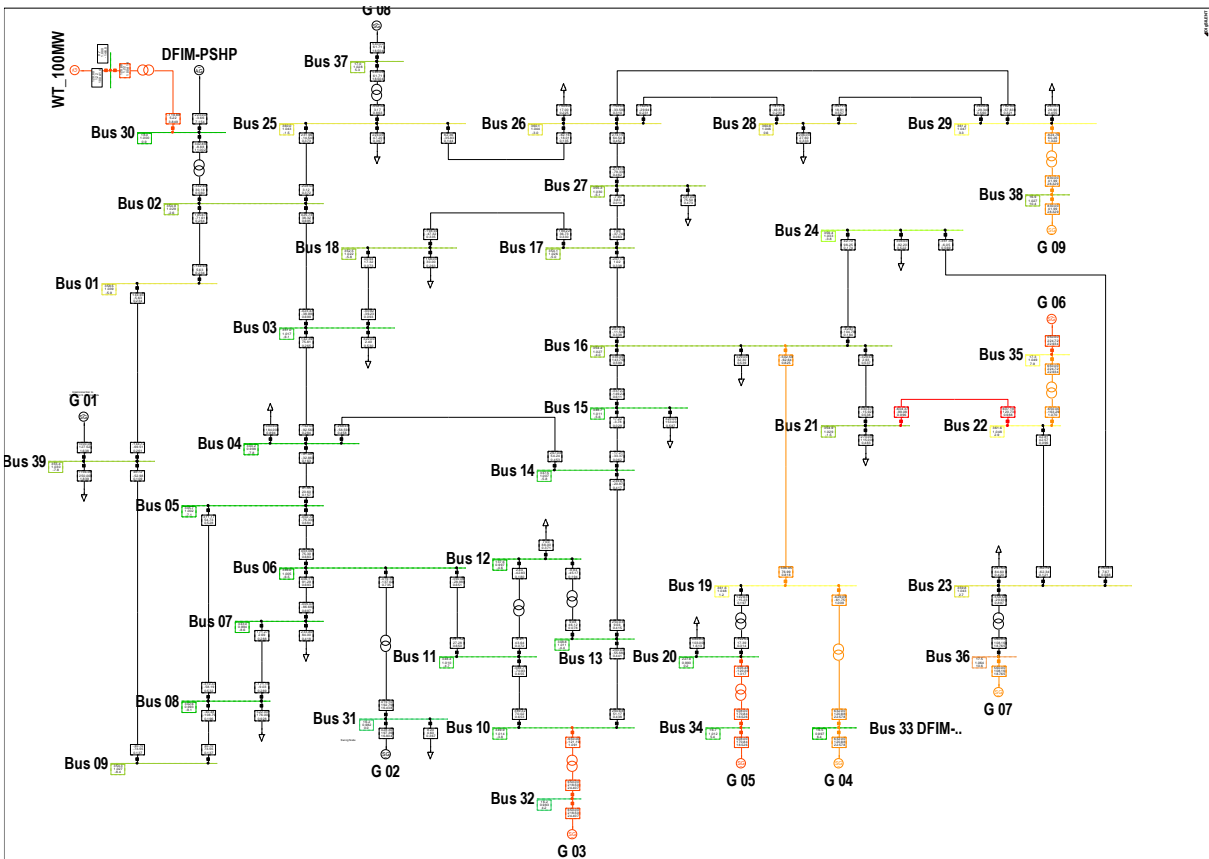


Figure 5.17: Load flow running of the wind-integrated DFIM-PSHP 39 bus system

5.3.2.1. Scenario 1: 150-millisecond fault at bus 30

In this scenario, a 150-millisecond fault is applied at bus 30 at the 10th second of the simulation. The fault only lasts 150 seconds, as in scenario 1 of the SM-PSHP. Generator 1 rotor angle and bus 33 voltage profile is analysed to see the impact of the fault on the system and how the DFIM-PSHP improves the system stability.

5.3.2.1.1. Voltage stability

Bus 33 voltage is temporarily reduced to shallow levels until the fault is cleared in 10.15 seconds, as seen in Figure 5.18. This is also the case with the voltages on the other nearby buses. This means stat voltage sags are unavoidable and tolerable under certain circumstances. However, the system oscillates to the post-fault state after a stable fault is cleared, and the voltages tend toward the post-fault steady-state level. “Although Bus33’s voltage oscillation reaches 1.036pu and 0.816pu, it regains its initial value of 1.00 pu when the fault is cleared. Figure 5.18 also shows that not only bus 33 voltage regain steady state after the fault is cleared respecting the characteristic mentioned earlier, oscillations are more damped with DFIM-PSHP.

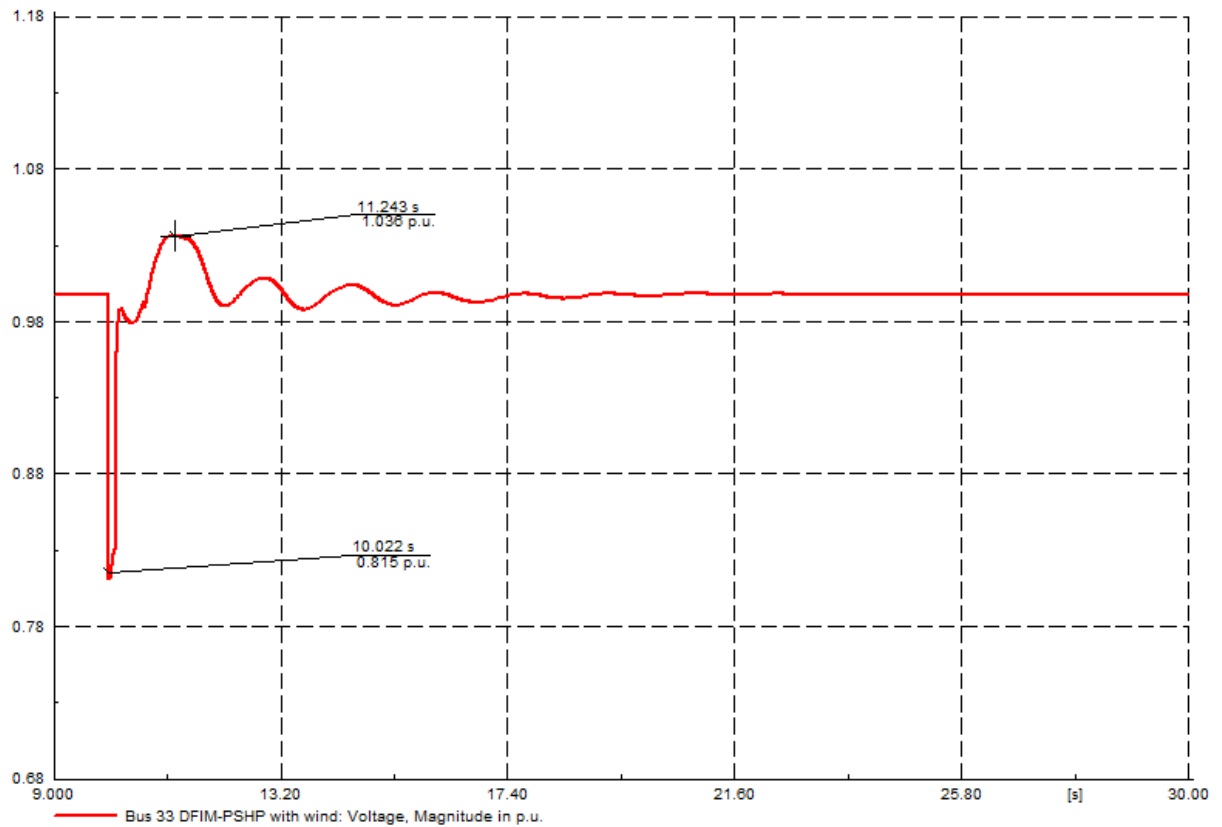


Figure 5.18: Bus 33 voltage with DFIM-PSHP and wind power for a 150ms fault at bus 30

5.3.2.1.2. Rotor angle stability

Figure 5.19 shows that oscillations observed on generator 1 rotor angle at the beginning of the simulation when using wind are eliminated. Generator 1 rotor angle has the maximal negative angle peak at -18.449 degrees and a minimum negative angle peak of -48.369 degrees after the fault has occurred and settles down at -36.310 in 25 seconds. According to the observation of Figure 5.19, the system's stability deteriorated not only by incorporating wind power into the power grid but also when the fault occurs greatly improved when using the DFIM-PSHP at bus 30 instead of G10. Moreover, oscillations are more damped than in the SM-PSHP case. Although the generator 1 rotor angle oscillates as the fault occurs, according to (Chen et al., 2017) and (ISO, 2017), in which an example for the determination of acceptable damping criteria for 39 bus system is described, The power grid is considered to be stable when the rotor angles are at nominal state.

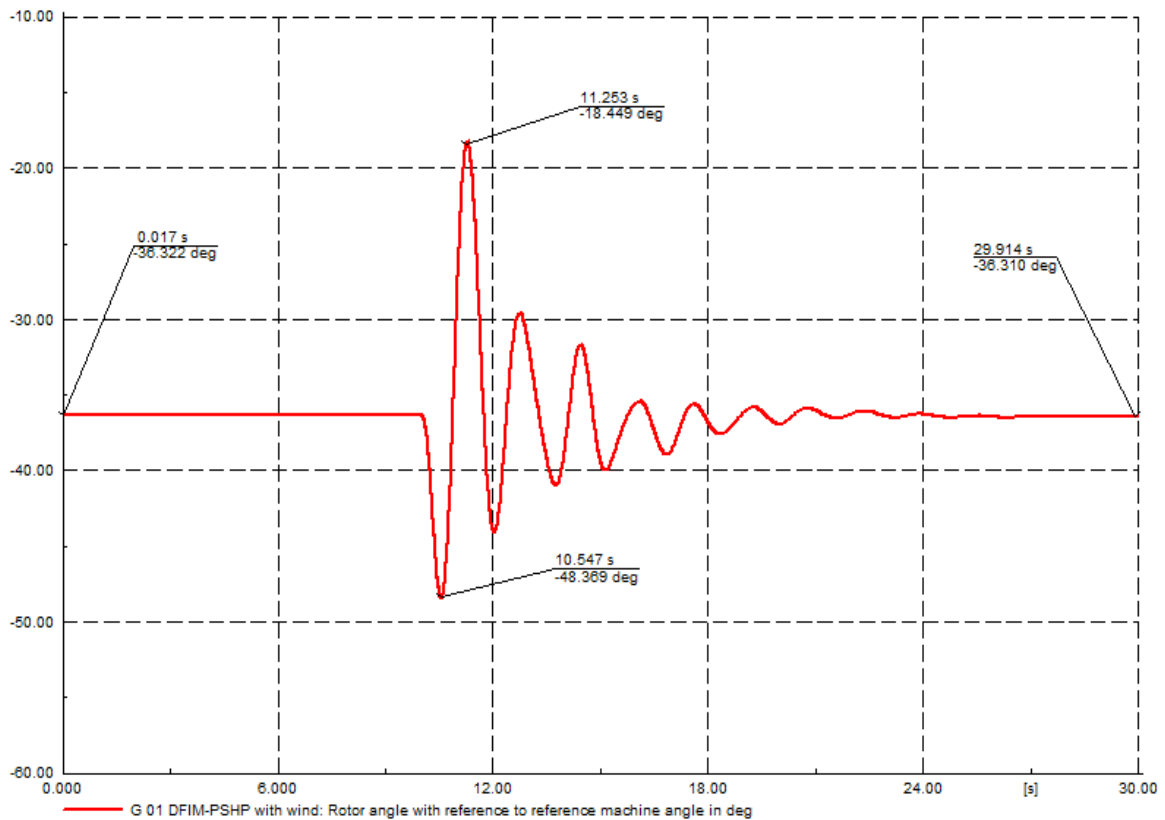


Figure 5.19: Generator 1 rotor angle with DFIM-PSHP and wind power for a 150ms fault at bus 30

5.3.2.2. Scenario 2: 450-millisecond fault at bus 30

This scenario presents the increase in the duration of the fault on bus 30 from 150-millisecond to 450-millisecond. In this scenario, the fault lasts longer, and the system stability is more affected. This scenario is important as it shows the effectiveness of the DFIM-PSHP over the SM-PSHP in stability improvement when the fault is cleared after 450 milliseconds.

5.3.2.2.1. Voltage stability

Bus 33 voltage oscillates to dangerously low and high levels until the fault is cleared in 10.45 seconds, as seen in figure 5.20. This is also the case with the voltages on the other nearby buses. This indicates that stat voltage dips are inevitable and reasonable under certain conditions. After a stable fault has been eliminated, the system oscillates to the post-fault state and the voltages trend toward the post-fault steady-state level. Although Bus33's voltage oscillation hits 1.106pu and 0.818pu, it returns to its previous value of 1.00 pu after the fault has been cleared. Bus 33 voltage regains steady state after the fault is cleared, and oscillations are more damped with the use of the DFIM-PSHP than when the SM-PSHP is used.

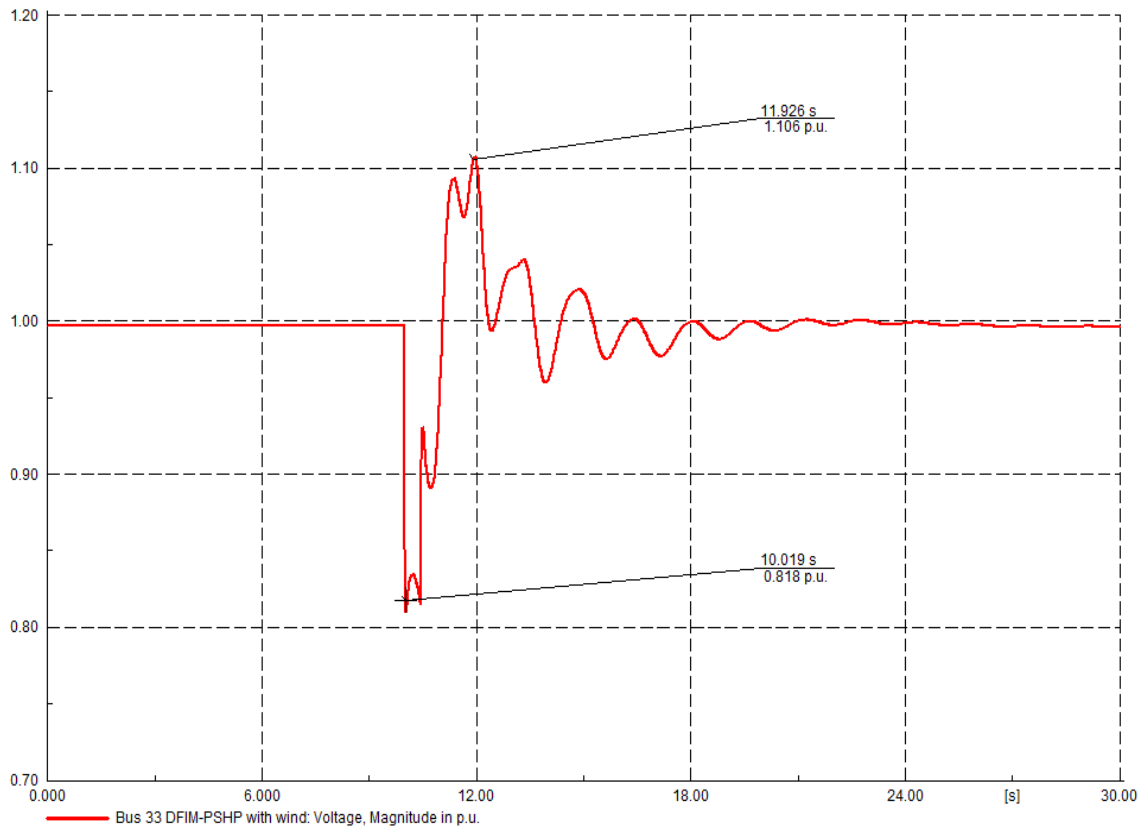


Figure 5.20: Bus 33 voltage with DFIM-PSHP and wind power for a 450ms fault at bus 30

5.3.2.2.2. Rotor angle stability

Figure 5.21 shows generator 1 rotor angle reaction during the disturbance. The positive and negative peaks of the angle response finish at various values. Generator 1 was operating with an angle of -33.322 degrees before the fault occurred, as seen in Figure 5.21. G1 oscillates with 21.920 degrees as the maximum value and -78.836 degrees as the minimum value before the system regains transient stability within 26 seconds. Figure 5.21 shows that not only generator 1 regains a steady state after the fault is cleared, and its rotor angle oscillations are more damped with the use of the DFIM-PSHP as compared to when the SM-PSHP is used.

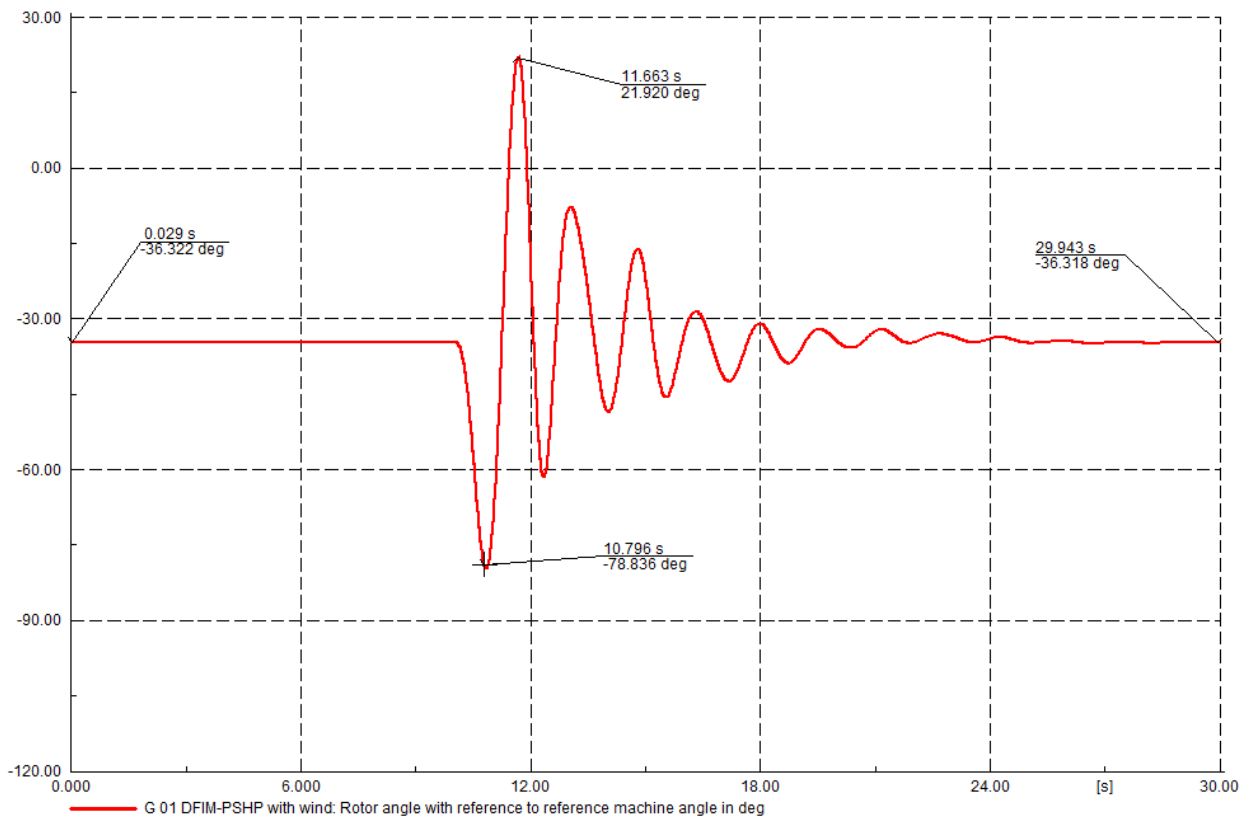


Figure 5.21: Generator 1 rotor angle with DFIM-PSHP and wind power for a 450ms fault at bus 30

5.4. Discussion

5.4.1. 150-millisecond fault at bus 30

5.4.1.1. Voltage stability

Figure 5.22 shows that although the voltage of the system with the DFIM-PSHP was more stable than that of the system with the SM-PSHP or for the system with no PSHP, the system was operating at a voltage of 1.0 per unit for all the cases before the fault occurred. . The 150milliseconds fault on bus 33 results in a voltage drop to 0.813 per unit. After 10.15 seconds, the fault is cleared, and the voltage is restored to 1.00 per unit for all the cases though the voltage of DFIM-PSHP stabilizes faster and has a lower peak value than that of the SM-PSHP or for the case with no PSHP.

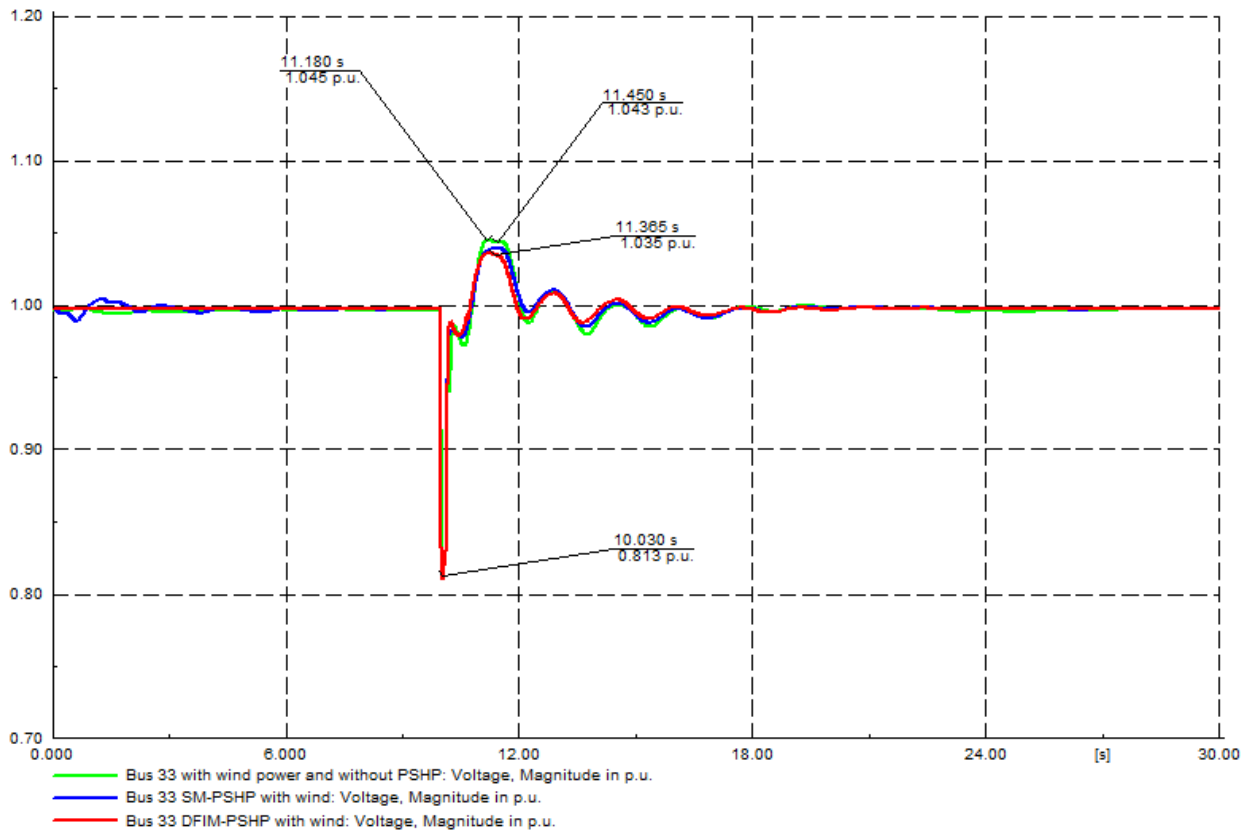


Figure 5.22: Bus 33 voltage variation for a 150ms fault at bus 30

5.4.1.2. Rotor angle stability

Figure 5.23 shows generator 1 rotor angle variation without PSHP, SM-PSHP and DFIM-PSHP. Although the rotor angle is the same in all the scenarios at the beginning of the simulation, the rotor angles of generator 1 have less variation when using the DFIM-PSHP. Those results show that although the SM PSHP case presents better results than the case without PSHP, DFIM PSHP presents less rotor angle and faster steady state recovery. Moreover, distortion as oscillations before the fault is also cleared with the DFIM-PSHP.

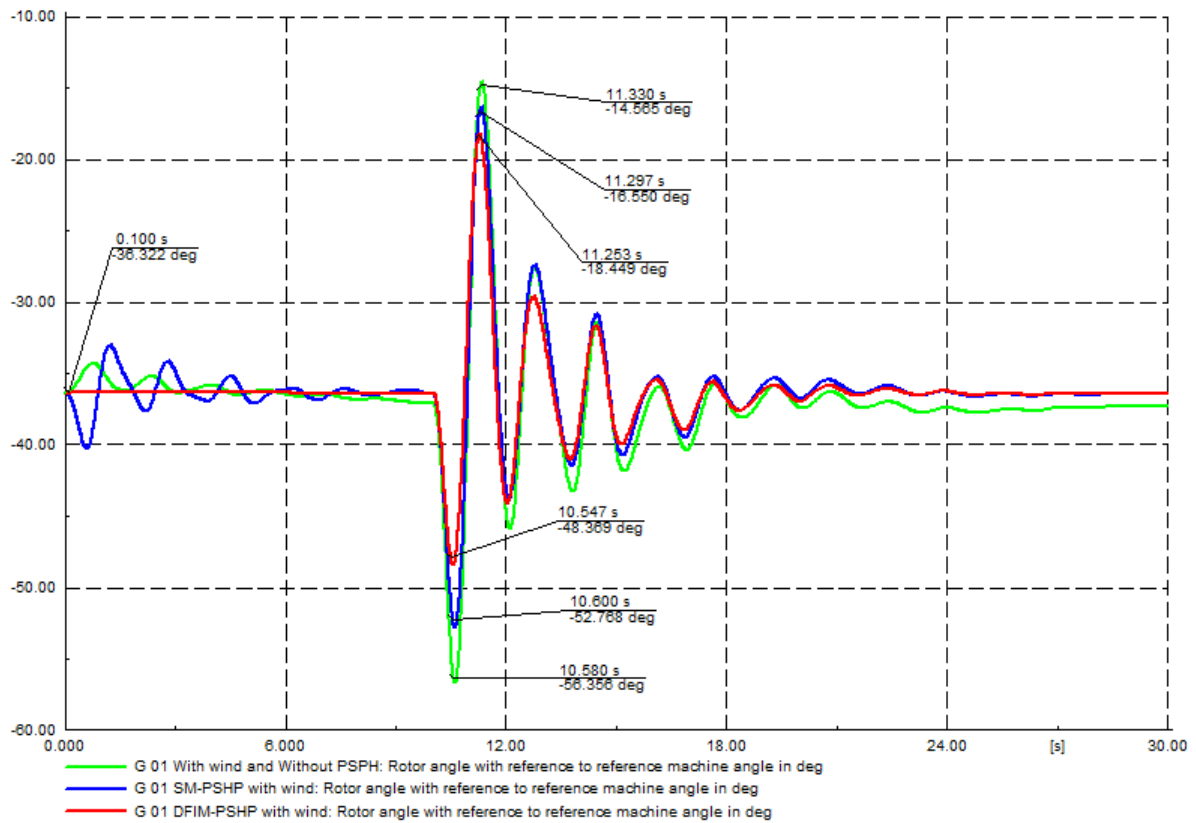


Figure 5.23: Generator 1 rotor angle variation for a 150ms fault at bus 30

Table 5.4 compares the maximum and minimum rotor angle values of generator 1. Results for the 150 milliseconds faults occurring on bus 30 show that the variation or difference of rotor angle for generator 1 is less when using the DFIM-PSHP than the SM-PSHP.

Table 5.4: Comparison of the difference between the maximum and minimum rotor angle values of Generator 1

		The maximum value in degree	The minimum value in degree
Generator 1 rotor angle	Without PSHP	-14.565	-56.356
	SM-PSHP	-16.550	-52.768
	DFIM-PSHP	-18.449	-48.369

5.4.2. 450-milliseconds fault at bus 30

5.4.2.1. Voltage stability

Figure 5.24 displays the voltage at the load bus or the fault bus for the different scenarios stated previously. Without PSHP, the voltage never recovers once the fault has been cleared, which violates various grid rules for certain transmission providers. As seen in Figure 5.24, the swing amplitude of the angle at operating point 2 grows larger and larger, eventually causing the system to lose stability. PSHP is used to solve this problem, as seen in Figure 5.22, where the voltage stabilizes after the fault is cleared when PSHP is used as compared to the scenario without PSHP. This means

that the allowable voltage range, which is 10% of the nominal voltage, is achieved in the whole simulation period of 30 seconds. In other words, the generator is out of step if the voltage at bus 33, the point of generator connection, does not reach the acceptable range, as seen in Figure 5.24.

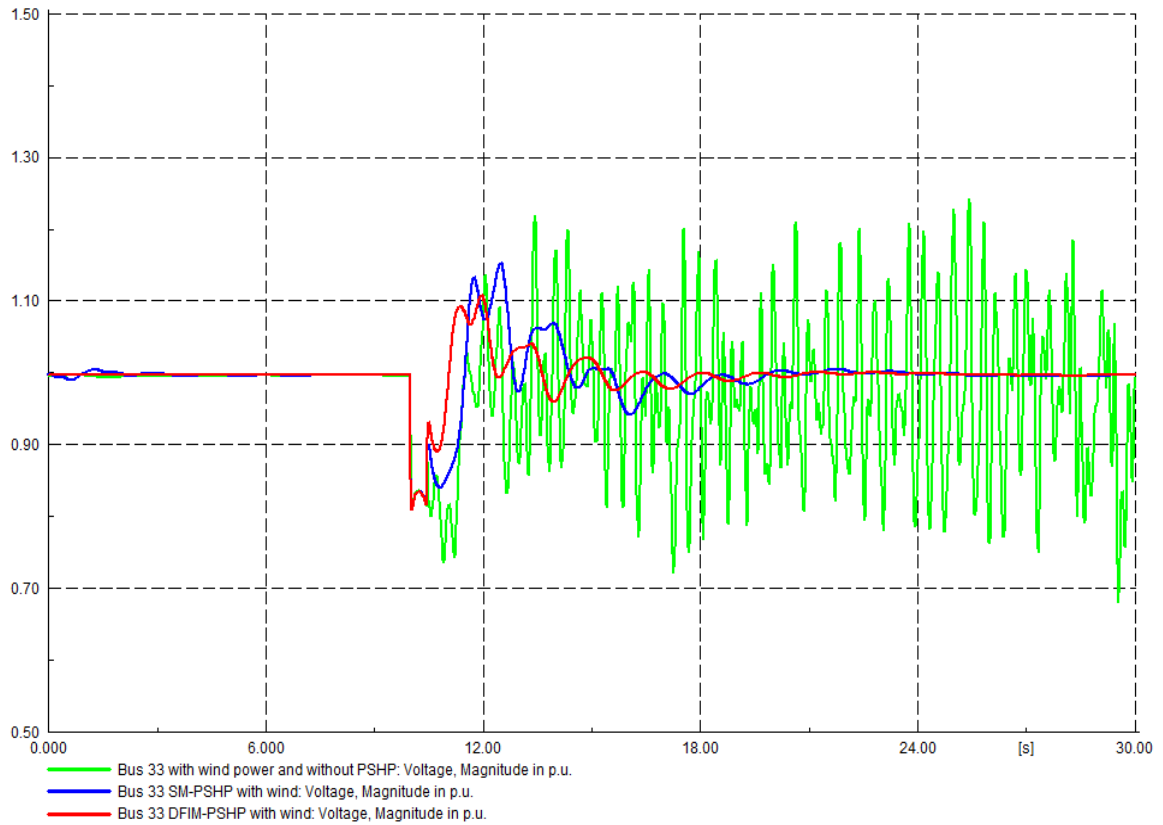


Figure 5.24: Bus 33 voltage variation for a 450ms fault at bus 30

5.4.2.2. Rotor angle stability

Figures 5.25 shows that the rotor angle of Generator 1 has less variation when using the DFIM PSHP. In addition, generator 1 rotor angle variation without PSHP and SM-PSHP and DFIM-PSHP in which generator 1 rotor angle is desynchronised for the case without PSHP after the fault occurs is also shown. Although the SM PSHP case presents better results than the one without PSHP as they prevent the system from losing its synchronism, DFIM PSHP presents less rotor angle distortion and faster steady state recovery.

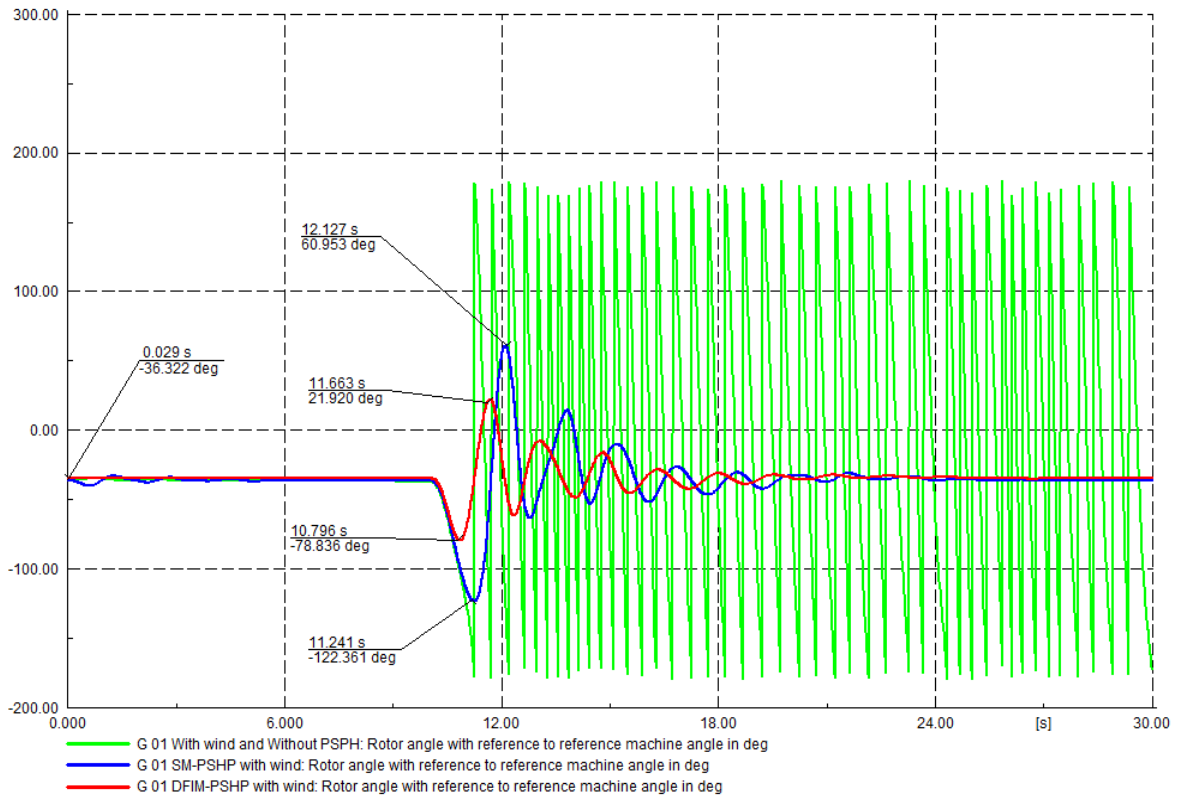


Figure 5.25: Generator 1 rotor angle variation for a 450ms fault at bus 30

Table 5.5 also confirms that the variation or difference of rotor angle for generator 1 is less when using the DFIM-PSHP than the SM-PSHP with a 450 milliseconds fault occurring on the same bus. Without PSHP, the system is desynchronised. PSHP cases present better results for voltage and rotor angle oscillations damped than the case with no PSHPs. As previously explained in the PSHP operation section, the total reactive power demand by the system was provided by the PSHP not only before the fault but also during the fault events. These results show how the system stability is improved with PSHP when the disturbance is caused by wind integration and when faults occur. When the 150-millisecond fault occurs, though the system remains stable after it is cleared, PSHP improves the voltage and rotor angle stability. Although the 450-millisecond fault causes the system to lose stability, PSHP makes it stable and synchronized.

Table 5.5: Variation or difference of rotor angle for generator 1

		The maximum value in degree	The minimum value in degree
Generator 1 rotor angle	Without PSHP	Desynchronised	Desynchronised
	SM-PSHP	60.953	-122.361
	DFIM-PSHP	21.920	-78.836

5.5. Conclusion

Different case studies studied and improved the stability of the IEEE 39 bus system wind power. In the first case study, SM-based PSHP and wind power are linked to bus 30 (100 MW wind power and 243 MW PSHP). The second case study used the DFIM-PSHP with the same parameters (100 MW wind power and 243 MW PSHP at bus 30). Oscillations appearing with wind power integration reveal that integrating wind power into a system can also impact the system's stability. Also, the fault duration significantly impacts the system's instability. The longer the fault, the more unstable the system becomes. It was also shown that a long fault could cause the system to lose its synchronism. Results indicate that by using DFIM-based PSHP in linked power grids, not only is the oscillation eliminated, but also the transient stability of the power system is significantly enhanced, as it may prevent the system from being desynchronized. In other words, using PSHP may enhance power system stability even if DFIM-PSHP presents better results than SM-PSHP. Although the machine's rotor angle variation is more significant in the case with no PSHP, they are also more effective when using SM-PSHP compared to DFIM-PSHP. In addition, using DFIM-PSHP instead of SM-PSHP improves the voltage recovery time and prevents the system from losing its stability.

CHAPTER SIX: CONCLUSION AND FUTURE WORK

The power system is a complex and large machine made of generators, transformers, lines, loads, and protective devices, and it may be structured as follow generation, transmission and distribution. All those subsystems work in harmony or are synchronised and ensure quality and continuity of supply. This is where the expression power system stability comes in. It is the property that the system has in remaining in an equilibrium state under normal operating conditions and the fact that it can also regain equilibrium after being subjected to a disturbance such as a fault. Although faults are used for stability analysis, load flow studies are inevitable when performing stability studies, and simulations are carried out in DigSilent PowerFactory. Many papers have presented various methodologies that can be used for power system enhancement in the presence of renewable energy. However, there is a lack of understanding of which and how these faults impact the rotor angle leading the system to become desynchronised. In this work, the IEEE 39 bus system's stability was improved by using SM-PSHP and DFIM-PSHP.

Mathematical modelling of the power system components used for this work has been presented. Those components are synchronous generators, transformers, transmission lines, and general load. Wind generators are chosen in this work because they are readily accessible and environmentally sustainable and have also been presented with mathematical modelling. Mathematical modelling of PSHP was also done. As mentioned in chapter two, SM-PSHP and DFIM-PSHP are the power system stability enhancement components chosen in this work. To study the stability of a network, load flow studies must first be done. As Newton Raphson's method was the load flow analysis method chosen for this work, its mathematical formulation was presented. Power system stability analysis tools, such as critical clearing time, are also presented. Power system stability has also been presented with its mathematical formulation.

Generators, transmission lines, transformers, loads, and shunt components are just a few of the components that make up power systems. Although they do not have the same parameters, their computer modelling was done according to their parameters with the IEEE 39 bus system, which comprises 39 buses, ten generators, 19 loads, 34 lines, and 12 transformers. The two networks were first designed without renewable energy. DFIG, taken from DigSILENT general templates library, was also computed and integrated into the IEEE 39 bus system. FS-PSHP and VS-PSHP have been discussed in detail and computed

The stability of a power system using wind energy is researched and enhanced. The benchmark case study illustrates the system's stable condition. In the first example study, when SM-based PSHP and wind power are connected to bus 30 (100 MW wind power and 243 MW PSHP), rotor angle simulation results are reported and compared. The second case study employs the same settings for the DFIM-PSHP (100 MW wind power and 243 MW PSHP at bus 30). Incorporating wind energy into a system may have an effect on the system's stability, since oscillations are seen when wind energy is included. Additionally, fault duration influences the system's instability. The greater the length of the fault, the more unstable the system. It was also shown that a protracted failure might result in the system losing its synchronisation. Results indicate that using DFIM-based PSHP in interconnected power grids not only eliminates oscillations, but also considerably improves the transient stability of the power system by preventing it from being desynchronized. In other words, using PSHP may enhance power system stability even if DFIM-PSHP presents better results than SM-PSHP. Although the machine's rotor angle variation is more significant in the case with no PSHP, they are also more effective when using SM-PSHP compared to DFIM-PSHP. In addition, using DFIM-PSHP instead of SM-PSHP improves the voltage recovery time and prevents the system from losing its stability.

Future studies might look at the impact of implementing a higher-rated STATCOM and other types of faults and using different kinds of renewable energy, such as solar PV.

REFERENCES

- Abaci, K., Yamacli, V. & Chen, Z. 2018. Voltage Stability Improvement by Using a Newly Designed STATCOM Controller in Case of High Wind Penetration Cases. In *Proceedings - 2018 IEEE 18th International Conference on Power Electronics and Motion Control, PEMC 2018*.
- Abaci, K., Yamacli, V. & Chen, Z. 2021. Voltage stability improvement with coordinated ULTC–STATCOM controller and VSC-HVDC in high wind penetration cases. *Electrical Engineering*, 103(2).
- Abidin, Z. 2020. Stabilitas Transien pada Saluran Transmisi dengan Static VAR Compensator (SVC) dan PSS (Power System Stabilizer). *Jurnal Elektro*.
- Aeggegn, D.B., Salau, A.O. & Gebru, Y. 2020. Load flow and contingency analysis for transmission line outage. *Archives of Electrical Engineering*, 69(3): 581–594.
- Aguero, E.D., Cepeda, J.C. & Colome, D.G. 2014. FACTS models for stability studies in DlgSILENT Power Factory. *2014 IEEE PES Transmission and Distribution Conference and Exposition, PES T and D-LA 2014 - Conference Proceedings*, 2014-Octob(February 2016).
- AJAY, K.T., MAHESH, S., SHIMPY, R. & DOVENDRA, K.V. 2020. Transient Stability Enhancement By Using Statcom and Stabilizer for Multi Machine Power System Network. *i-manager's Journal on Power Systems Engineering*, 8(2): 34.
- Alizadeh Bidgoli, M. & Bathaee, S.M.T. 2015. Full-state variables control of a grid-connected pumped storage power plant using non-linear controllers. *Electric Power Components and Systems*, 43(3).
- Alizadeh Bidgoli, M., Ganjali, D., Yang, W. & Atrian, S. 2021. *Small signal stability improvement of pumped storage hydropower using wide area signal considering wind farm*. Springer International Publishing. http://dx.doi.org/10.1007/978-3-030-54275-7_9.
- Alizadeh Bidgoli, M. & Gonzalez-Longatt, F.M. 2021. *Transient Stability Assessment of Power System Incorporating DFIM-Based Pumped Storage Hydropower and Wind Farm*. Springer International Publishing. http://dx.doi.org/10.1007/978-3-030-54124-8_5.
- Alizadeh Bidgoli, M. & Yang, W. 2020. DFIM versus synchronous machine for variable speed pumped storage hydropower plants: A comparative evaluation of technical performance. *Renewable Energy*, 159.
- AllumiaX Staff Engineers. 2019. Fault analysis in power systems. *Fault Analysis Open Circuit Faults Short Circuit Faults Symmetrical And Unsymmetrical Faults Types Of Faults* .

- <https://www.allumiax.com/blog/fault-analysis-in-power-systems> 30 May 2021.
- Anon. 2020. Electrical distribution engineering. *Choice Reviews Online*, 30(01): 30-0318-30–0318.
- Anon. 2012. Wind energy conversion system with full-scale power converter and squirrel cage induction generator. *International Journal of Physical Sciences*.
- Applications, I. & Transmission, P. 2015. IGBT Applications: Power Transmission 16. , 16: 539–560.
- Arabkoohsar, A. & Namib, H. 2021. Pumped hydropower storage. In *Mechanical Energy Storage Technologies*. Elsevier: 73–100.
- Araga, I.A. & Airoboman, A.E. 2021. Enhancement of voltage stability in an interconnected network using unified power flow controller. *Journal of Advances in Science and Engineering*, 4(1).
- Ashok Kumar, L., Archana, N. & Vidhyapriya, R. 2015. Power quality improvement of grid connected wind energy systems using STATCOM-battery energy storage system. *ARPJ Journal of Engineering and Applied Sciences*, 10(21).
- Asija, D., Choudekar, P., Ruchira & Chouhan, M. 2015. Performance Evaluation and Improvement in Transient Instability of IEEE 9 Bus System Using Exciter and Governor Control. In *Procedia Computer Science*.
- B, V.R. 2015. Designing of Power System Stabilizer and It Effects on Power System. , 3(04): 1–6.
- Bangash, K.N., Farrag, M.E.A. & Osman, A.H. 2019. Investigation of Energy Storage Batteries in Stability Enforcement of Low Inertia Active Distribution Network. *Technology and Economics of Smart Grids and Sustainable Energy*, 4(1).
- Bannykh, P., Lozhkin, S. & Pazderin, A. 2018. Software package for power flow mathematical modeling with single-phase and three-phase power-energy flow model. *CEUR Workshop Proceedings*, 2298.
- Bidgoli, M.A., Mohammadpour, H.A. & Bathaee, S.M.T. 2015. Advanced Vector Control Design for DFIM-Based Hydropower Storage for Fault Ride-Through Enhancement. *IEEE Transactions on Energy Conversion*, 30(4).
- Chakravorty, M., Das, M. & Patra, S. 2015. Importance of Load Flow Analysis in Voltage Stability Studies. , (December): 45–50.
- Chatterjee, S. & Mandal, S. 2017. A novel comparison of gauss-seidel and Newton- raphson methods for load flow analysis. In *International Conference on Power and Embedded*

Drive Control, ICPEDC 2017.

- Chen, S., Onwuachumba, A., Musavi, M. & Lerley, P. 2017. A quantification index for power systems transient stability. *Energies*, 10(7).
- Christy, C.. 1990. Analysis of steady state voltage stability in large scale power system.
- Cifuentes, N., Rahmann, C., Valencia, F. & Alvarez, R. 2019. Network allocation of BESS with voltage support capability for improving the stability of power systems. *IET Generation, Transmission and Distribution*, 13(6).
- Dai, J. & Dourian, R. 2018. Standard Approach To Perform Power System Stability Studies in Oil and Gas Plants.
- Darabian, M., Jalilvand, A. & Azari, M. 2016. Power system stability enhancement in the presence of renewable energy resources and HVDC lines based on predictive control strategy. *International Journal of Electrical Power and Energy Systems*.
- Dasu, B., Siva Kumar, M. & Srinivasa Rao, R. 2019. Design of robust modified power system stabilizer for dynamic stability improvement using Particle Swarm Optimization technique. *Ain Shams Engineering Journal*, 10(4).
- Dasu, B., Sivakumar, M. & Srinivasarao, R. 2019. Interconnected multi-machine power system stabilizer design using whale optimization algorithm. *Protection and Control of Modern Power Systems*, 4(1).
- Deshpande, M. V. 2010. *Design and testing of electrical machines*.
- Dey, P., Bhattacharya, A. & Das, P. 2017. Tuning of power system stabilizer for small signal stability improvement of interconnected power system. *Applied Computing and Informatics*, 16(1–2).
- DlgSILENT GmbH. 2015. DlgSILENT PowerFactory Technical Reference Documentation Doubly-Fed Induction Machine. <http://www.digsilent.de>.
- DlgSILENT GmbH. 2015a. 39 bus New England system. : 1–16.
- DlgSILENT GmbH. 2015b. DlgSILENT PowerFactory Technical Reference Documentation General Load.
- DlgSILENT GmbH. 2015c. DlgSILENT Powerfactory Technical Reference Documentation Rectifier/Inverter. : 1–31.
- DlgSILENT GmbH. 2015d. DlgSILENT PowerFactory Technical Reference Documentation Two-Winding Transformer (3-Phase).
- Dorile, P.O., Jagessar, D.R., Guardado, L., Jagessar, S.S. & Mccann, R.A. 2021. Power

System Stabilization of a Grid Highly Penetrated from a Variable-Speed Wind Based Farm Through Robust Means of STATCOM and SSSC. *2021 16th International Conference on Engineering of Modern Electric Systems (EMES) | 978-1-6654-4995-3/21/\$31.00 ©2021 IEEE | DOI: 10.1109/EMES52337.2021.9484110.*

- Eidiani, M., Ebrahimean Baydokhty, M., Ghamat, M., Zeynal, H. & Mortazavi, H. 2011. Transient stability enhancement via hybrid technical approach. *Proceedings - 2011 IEEE Student Conference on Research and Development, SCORed 2011: 375–380.*
- European Commission. 2015. Renewable energy progress report. *Report From the Commission To the European Parliament, the Council, the European Economic and Social Committee and the Committee of the Regions.*
- Farmer, W.J. & Rix, A.J. 2019. Optimising Power System Frequency Stability Using Virtual Inertia from Inverter-based Renewable Energy Generation. In *ICCEP 2019 - 7th International Conference on Clean Electrical Power: Renewable Energy Resources Impact.*
- Firouzi, M., Gharehpetian, G.B. & Salami, Y. 2017. Active and reactive power control of wind farm for enhancement transient stability of multi-machine power system using UIPC. *IET Renewable Power Generation*, 11(8): 1246–1252.
- Garba, J. & Sani, S. 2018. Coordinated Placement and Tuning of STATCOM and SSSC for Oscillation Damping in a Wide Area Networks of Power System . *Turk J Elec Eng & Comp Sci.*
- Govindasamy, S. & Rangaswamy, A. 2020. Configuration and Digital Simulation of STATCOM utilizing 48-Pulse VSC for Reactive Power Reparation and Potential Reliability. *International Journal of Computer Communication and Informatics*, 2(1).
- Grigsby, L.L. 2018. *Electric Power Generation, Transmission, and Distribution: The Electric Power Engineering Handbook.*
- Gross, C.A. 2017. Power transformers. In *Systems, Controls, Embedded Systems, Energy, and Machines.*
- Gurung, S., Naetiladdanon, S. & Sangswang, A. 2019. Coordination of power-system stabilizers and battery energy-storage system controllers to improve probabilistic small-signal stability considering integration of renewable-energy resources. *Applied Sciences (Switzerland)*, 9(6).
- Hansen, A., Iov, F., Sorensen, P., Cutululis, N., Jauch, C. & Blaabjerg, F. 2007. *Dynamic wind turbine models in power system simulation tool \uppercase{DIGSILENT}.*

- Hanson, A. & Grigsby, L. 2017. Power system analysis. In *Systems, Controls, Embedded Systems, Energy, and Machines*.
- Hatziargyriou, N., Milanovic, J., Rahmann, C., Ajarapu, V., Canizares, C., Erlich, I., Hill, D., Hiskens, I., Kamwa, I., Pal, B., Pourbeik, P., Sanchez-Gasca, J., Stankovic, A., Van Cutsem, T., Vittal, V. & Vournas, C. 2021. Definition and Classification of Power System Stability - Revisited & Extended. *IEEE Transactions on Power Systems*, 36(4): 3271–3281.
- Hemeida, M.G., Rezk, H. & Hamada, M.M. 2018. A comprehensive comparison of STATCOM versus SVC-based fuzzy controller for stability improvement of wind farm connected to multi-machine power system. *Electrical Engineering*, 100(2).
- ISO. 2017. ISO New England Stability planning procedure.
- Kamble, S., Kanojiya, S., Male, Y., Ingale, G., Manekar, P., Patrik, R., Shrikhande, R. & Kamdi, S. 2017. Transient Stability Analysis of IEEE-9 Bus Electrical Power System. *International Journal Of Engineering And Computer Science*, 6(4): 20847–20850.
- Karami, A. & Mahmoodi Galougahi, K. 2019. Improvement in power system transient stability by using STATCOM and neural networks. *Electrical Engineering*, 101(1).
- Karlsson, B. 2017. Comparison of PSSE & PowerFactory. , (September): 1–122.
- Kaur, R. & Kumar, D. 2016. Transient Stability Improvement of IEEE 9 Bus System Using Power World Simulator. *MATEC Web of Conferences*.
- Kehinde, O.P. 2012. Transient Stability Assessment of Hybrid Distributed Generation Using Computational Intelligence Approaches. *University of Cape Town*: 322.
- Khan, B. & Kassas, M. 2019. FSIG-Based wind power plant transient stability margin improvement, a STATCOM/SVC Comparison. In *2019 IEEE Texas Power and Energy Conference, TPEC 2019*.
- Khomami Pamsari, H., Alizadeh Bidgoli, M., Rajabzadeh, M., Bathaee, S.M.T. & Ozgoli, S. 2011. Application of a new multivariable sliding mode controller for the single machine infinite bus systems. In *2011 2nd Power Electronics, Drive Systems and Technologies Conference, PEDSTC 2011*.
- Kim, J.J. & Park, J.H. 2021. A novel structure of a power system stabilizer for microgrids. *Energies*, 14(4).
- Kishore, T.S., Vijayakrishna, R. & Venkateswarlu, C. 2020. Static Voltage Stability Margin Enhancement Using STATCOM in Grid Connected Wind Farms. *Proceedings - 2020 IEEE India Council International Subsections Conference, INDISCON 2020*: 90–95.

- Kumar, G. & Nijhawan, P. 2016. Simulation-Based performance analysis of three-level 48-pulse STATCOM with constant DC link voltage for reactive power compensation. In *India International Conference on Power Electronics, IICPE*.
- Kyriakides, E. & Polycarpou, M. 2015. *Intelligent Monitoring, Control, and Security of Critical Infrastructure Systems Conclusions*.
- Li, A. 2016. A novel improved voltage stabilizer using a power system stabilizer (PSS) and static var compensator (SVC). *International Journal of Simulation: Systems, Science and Technology*, 17(47).
- Liu, J., Su, C., Wang, X., Fang, W., Niu, S. & Cheng, L. 2017. Abnormality in power system transient stability control of BESS/STATCOM. *The Journal of Engineering*, 2017(13).
- Lyshevski, S.E. & Lyshevski, S.E. 2018. Synchronous machines. In *Electromechanical Systems, Electric Machines, and Applied Mechatronics*.
- Majidi, M., Rodriguez-Garcia, L., Parvania, M. & Mosier, T.M. 2020. Integration of small pumped storage hydropower units in water distribution system operation. In *IEEE Power and Energy Society General Meeting*. IEEE Computer Society.
- Manjul, N. & Rawat, M.S. 2021. Transient Stability Analysis of Wind Integrated Power Network Using STATCOM and BESS Using DIgSILENT PowerFactory. In *Springer Nature Singapore Pte Ltd. 2021 M. Bose and A. Modi (eds.), Proceedings of the 7th International Conference on Advances in Energy Research, Springer Proceedings in Energy*.
- Marić, P., Kljajić, R., Chamorro, H.R. & Glavaš, H. 2021. Power system stabilizer tuning algorithm in a multimachine system based on s-domain and time domain system performance measures. *Energies*, 14(18).
- McWilliams, M. 2021. Pumped Storage Hydropower. In *Reference Module in Earth Systems and Environmental Sciences*. Elsevier.
- Mekhanet, M. & Mokrani, L. 2020. Online self-tuning power system stabilizer based on the speed gradient. *International Journal on Electrical Engineering and Informatics*, 12(2).
- Mohammad, A. & Hossain, S. 2016. A STUDY ON : TRANSIENT STABILITY IMPROVEMENT OF POWER TRANSMISSION GRID BY CONTROLLED FAULT CURRENT LIMITERS CONSIDERING CYBER-ATTACKS. , (August).
- Mohanty, A., Viswavandya, M., Mishra, D., Ray, P.K., Patra, S. & Sthitapragyan, M. 2016. An optimized STATCOM controller for voltage stability and reactive power compensation in an isolated micro grid. In *2015 IEEE Power, Communication and Information*

- Mrehel, O.G. & Shenbisha, A. 2021. Comparative Study on Effect of Different Wind Generator Types on Power Systems Stability. *2021 IEEE 1st International Maghreb Meeting of the Conference on Sciences and Techniques of Automatic Control and Computer Engineering MI-STA, 25-27 May 2021, Tripoli-Libya, (May): 25–27.*
- Muruganantham, B., Gnanadass, R. & Padhy, N.P. 2017. Challenges with renewable energy sources and storage in practical distribution systems. *Renewable and Sustainable Energy Reviews, 73.*
- Naeem, A. & Atif, A. 2018. Transient Stability of Power System by Static VAR Compensator (SVC) and Power System Stabilizers (PSS) using MATLAB/SIMULINK. *International Journal of Electrical and Electronics Engineering, 5(4): 15–19.*
- Nagababu, M., Srinivas, R.S., Sobhan, P.V.S. & Subbarao, M. 2019. Transient stability improvement of wind farm integrated power system using STATCOM. *International Journal of Engineering and Advanced Technology, 8(6 Special Issue 3).*
- NERSA. 2020. *Annual report 2019/2020.*
- Netzberechnungssoftware, I. 2015. PowerFactory 15 user manual. : 0–26.
- NPTEL. 2019. Fault Analysis : Symmetrical faults : Unsymmetrical faults : Symmetrical or Balanced three phase fault analysis : *Nptel.Ac.in: 146–154.*
- NTEKA, M.F. 2013. Development and Assessment of Reduced Order Power System Models. , (July).
- Oh, S., Shin, H., Cho, H. & Lee, B. 2018. Transient impact analysis of high renewable energy sources penetration according to the future Korean power grid scenario. *Sustainability (Switzerland), 10(11).*
- Ou, T.C., Lu, K.H. & Huang, C.J. 2017. Improvement of transient stability in a hybrid power multi-system using a designed NIDC (Novel Intelligent Damping Controller). *Energies, 10(4): 1–16.*
- Papadopoulos, P.N. & Milanović, J. V. 2017. Probabilistic Framework for Transient Stability Assessment of Power Systems with High Penetration of Renewable Generation. *IEEE Transactions on Power Systems.*
- Peres, W., Silva Júnior, I.C. & Passos Filho, J.A. 2018. Gradient based hybrid metaheuristics for robust tuning of power system stabilizers. *International Journal of Electrical Power and Energy Systems, 95.*
- Perilla, A., Papadakis, S., Torres, J.L.R., van der Meijden, M., Palensky, P. & Gonzalez-

- Longatt, F. 2020. Transient stability performance of power systems with high share of wind generators equipped with power-angle modulation controllers or fast local voltage controllers. *Energies*, 13(6).
- Perilla, A., Torres, J.L.R., Papadakis, S., Rakhshani, E., van der Meijden, M. & Gonzalez-Longatt, F. 2020. Power-angle modulation controller to support transient stability of power systems dominated by power electronic interfaced wind generation. *Energies*, 13(12).
- Petersen, L., Kryezi, F. & Iov, F. 2017. Design and tuning of wind power plant voltage controller with embedded application of wind turbines and STATCOMs. In *IET Renewable Power Generation*.
- Petinrin, J.O. & Shaaban, M. 2016. Impact of renewable generation on voltage control in distribution systems. *Renewable and Sustainable Energy Reviews*.
- Pico, H.N.V. 2017. Transient Stability Assessment of Power Systems With Uncertain Renewable Generation. , (July).
- Powerfactory, D. 2015. DigSILENT PowerFactory Technical Reference Documentation Synchronous Machine. , 1: 1–40.
- Prathap, D. & Krishna, H. 2011. Design Of Power System Stabilizer To Improve Small Signal Stability By Using Modified Heffron-Phillip ' s Model. , 3(6): 4888–4896.
- Raghutu, R. & Ramana Rao, P. V. 2020. Comparative stability enhancement of micro-grid interconnected power system with anfis and integer-order power system stabilizer. *International Journal of Emerging Trends in Engineering Research*, 8(9).
- Rahman, M.S., Pota, H.R., Mahmud, M.A. & Hossain, M.J. 2016. A decentralised multi-agent approach to enhance the stability of smart microgrids with renewable energy. *International Journal of Sustainable Energy*.
- Rashid, G. & Ali, M.H. 2015. Transient Stability Enhancement of Doubly Fed Induction Machine-Based Wind Generator by Bridge-Type Fault Current Limiter. *IEEE Transactions on Energy Conversion*.
- Remon, D., Cantarellas, A.M., Mauricio, J.M. & Rodriguez, P. 2017. Power system stability analysis under increasing penetration of photovoltaic power plants with synchronous power controllers. *IET Renewable Power Generation*.
- Renuka, T. & Kesavarao, G. 2017. STATCOM with battery and super capacitor hybrid energy storage system for enhancement of voltage stability. *Indonesian Journal of Electrical Engineering and Computer Science*, 5(2).

- Routray, S.K., Nayak, N. & Rout, P.K. 2012. A Robust Fuzzy Sliding Mode Control Design for Current Source Inverter based STATCOM Application. *Procedia Technology*, 4.
- S. Bhole, S. & Nigam, P. 2015. Improvement of Voltage Stability in Power System by Using SVC and STATCOM. *International Journal of Advanced Research in Electrical, Electronics and Instrumentation Engineering*, 04(02).
- Sahami, A. & Kamalasadani, S. 2019. Prediction and Enhancement of Power System Transient Stability Using Taylor Series. *2018 North American Power Symposium, NAPS 2018*, (January).
- Sengupta, S., Kumar, A. & Tiwari, S. 2018. Transient stability enhancement of a hybrid Wind-PV farm incorporating a STATCOM. *2018 3rd IEEE International Conference on Recent Trends in Electronics, Information and Communication Technology, RTEICT 2018 - Proceedings*: 1574–1580.
- Shadabi, H. & Kamwa, I. 2022. A decentralized non-linear dynamic droop control of a hybrid energy storage system bluefor primary frequency control in integrated AC-MTDC systems. *International Journal of Electrical Power and Energy Systems*, 136.
- Sharma, A., Saini, M. & Ahmed, M. 2017. Power Flow Analysis Using NR Method. *International Conference on Innovative Research in Science, Technology and Management*: 324–329. <http://data.conferenceworld.in/MIMT/P324-329.pdf>.
- Som, S., De, S., Chakrabarti, S., Sahoo, S.R. & Ghosh, A. 2022. A robust controller for battery energy storage system of an islanded ac microgrid. *IEEE Transactions on Industrial Informatics*, 18(1).
- Su, C., Zhou, H., Yan, P., Meng, L. & Cheng, Z. 2021. Research on Improving Transient Stability of Power System with Distributed BESS and its Coordinated Control Method. In *E3S Web of Conferences*.
- Subramaniam, T., Rahman, M.S.A., Ariffin, A.M. & Sahrim, M. 2018. An investigation on the power system stability of photovoltaic grid integrated system. In *Proceedings - 7th IEEE International Conference on Control System, Computing and Engineering, ICCSCE 2017*.
- Tanaka, T., Ma, K., Wang, H. & Blaabjerg, F. 2019. Asymmetrical Reactive Power Capability of Modular Multilevel Cascade Converter Based STATCOMs for Offshore Wind Farm. *IEEE Transactions on Power Electronics*, 34(6).
- Tavukcu, E. & Türkay, B.E. 2017. Transient stability analysis of the transmission system considering the initial steady state results. In *2017 10th International Symposium on Advanced Topics in Electrical Engineering, ATEE 2017*.

- Tephiruk, N., Kanokbannakorn, W., Kerdphol, T., Mitani, Y. & Hongesombut, K. 2018. Fuzzy logic control of a battery energy storage system for stability improvement in an islanded microgrid. *Sustainability (Switzerland)*, 10(5).
- Thakur, T. 2016. Three Phase Faults Analysis of Power System. *Global Journal of Researches in Engineering (USA)*, 16(5): 13.
- The, I., Of, A., Power, M. & Line, T. 2017. INVESTIGATING THE APPLICATION OF STATIC SYNCHRONOUS COMPENSATOR (STATCOM) FOR MITIGATING POWER TRANSMISSION LINE LOSSES.pdf.
- Del Vecchio, R.M. 2018. *Transformer design principles*. Third edition. Boca Raton, FL: CRC Press.
- Verdejo, H., Pino, V., Kliemann, W., Becker, C. & Delpiano, J. 2020. Implementation of particle swarm optimization (PSO) algorithm for tuning of power system stabilizers in multimachine electric power systems. *Energies*, 13(8).
- Vu, T.L. & Turitsyn, K. 2017. A Framework for Robust Assessment of Power Grid Stability and Resiliency. *IEEE Transactions on Automatic Control*.
- Wang, X., Chen, L., Chen, Q., Mei, Y. & Wang, H. 2018. Model and analysis of integrating wind and PV power in remote and core areas with small hydropower and pumped hydropower storage. *Energies*, 11(12).
- Wei, S., Zhou, Y. & Huang, Y. 2017. Synchronous Motor-Generator Pair to Enhance Small Signal and Transient Stability of Power System with High Penetration of Renewable Energy. *IEEE Access*.
- Wende, S., Berry-stölzle, T.R. & Lai, G.C. 2107. Result Analysis on Load Flow by Using Newton Raphson Method. *International Journal of Advanced Research in Electrical, Electronics and Instrumentation Engineering*, 6(7): 5835–5844.
- Xia, S., Zhang, Q., Hussain, S.T., Hong, B. & Zou, W. 2018. Impacts of integration of wind farms on power system transient stability. *Applied Sciences (Switzerland)*.
- Xia, S.W., Bu, S.Q., Zhang, X., Xu, Y., Zhou, B. & Zhu, J.B. 2018. Model reduction strategy of doubly-fed induction generator-based wind farms for power system small-signal rotor angle stability analysis. *Applied Energy*.
- Xu, X., Yan, Z., Shahidehpour, M., Wang, H. & Chen, S. 2018. Power System Voltage Stability Evaluation Considering Renewable Energy With Correlated Variabilities. *IEEE Transactions on Power Systems*.
- Yadav, P., Sharma, P.R. & Gupta, S.K. 2014. Enhancement of Voltage Stability in Power

System Using Unified Power Flow Controller. *IOSR Journal of Electrical and Electronics Engineering*, 9(1): 76–82.

Yagami, M., Ishikawa, S., Ichinohe, Y., Misawa, K. & Tamura, J. 2014. Transient stability analysis of power system with photovoltaic systems installed. In *IET Conference Publications*.

Zhang, Y., Kou, P., Yu, L. & Liang, D. 2022. Coordinated voltage and frequency control for HVDC sending end under pole-block fault: Using model predictive control. *International Journal of Electrical Power and Energy Systems*, 136.

Zhao, Z., Yang, J., Chung, C.Y., Yang, W., He, X. & Chen, M. 2021. Performance enhancement of pumped storage units for system frequency support based on a novel small signal model. *Energy*, 234.

Zheng, L., Kuang, H., Zhang, S., Li, S. & Ding, X. 2017. Voltage stability improvement of wind power integrated system using TCSC-STATCOM control. *Dianli Xitong Baohu yu Kongzhi/Power System Protection and Control*, 45(22).